Structural Optimization and Design of a Strut-Braced Wing Aircraft

Amir H. Naghshineh-Pour

Thesis submitted to the Faculty of the
Virginia Polytechnic Institute and State University
in partial fulfillment of the requirements for the degree of

Master of Science
in
Aerospace Engineering

Rakesh K. Kapania, Chair
Joseph A. Schetz
William H. Mason
Eric R. Johnson

November 30, 1998
Blacksburg, Virginia

Keywords: Aircraft Design, Multidisciplinary Design Optimization,
Structural Optimization, Strut-Braced Wing, Wing Box

Structural Optimization and Design of a Strut-Braced Wing Aircraft

Amir H. Naghshineh-Pour

(ABSTRACT)

A significant improvement can be achieved in the performance of transonic transport aircraft using Multidisciplinary Design Optimization (MDO) by implementing truss-braced wing concepts in combination with other advanced technologies and novel design innovations. A considerable reduction in drag can be obtained by using a high aspect ratio wing with thin airfoil sections and tip-mounted engines. However, such wing structures could suffer from a significant weight penalty. Thus, the use of an external strut or a truss bracing is promising for weight reduction.

Due to the unconventional nature of the proposed concept, commonly available wing weight equations for transport aircraft will not be sufficiently accurate. Hence, a bending material weight calculation procedure was developed to take into account the influence of the strut upon the wing weight, and this was coupled to the Flight Optimization System (FLOPS) for total wing weight estimation. The wing bending material weight for single-strut configurations is estimated by modeling the wing structure as an idealized double-plate model using a piecewise linear load method.

Two maneuver load conditions 2.5g and -1.0g × factor of safety of 1.5 and a 2.0g taxi bump are considered as the critical load conditions to determine the wing bending material weight. From preliminary analyses, the buckling of the strut under the –1.0g load condition proved to be the critical structural challenge. To address this issue, an innovative design strategy introduces a telescoping sleeve mechanism to allow the strut to be inactive during negative g maneuvers and active during positive g maneuvers. Also, more wing weight reduction is obtained by optimizing the strut

force, a strut offset length, and the wing-strut junction location. The best configuration shows a 9.2% savings in takeoff gross weight, an 18.2% savings in wing weight and a 15.4% savings in fuel weight compared to a cantilever wing counterpart.

Acknowledgments

First and foremost, I would like to thank God for giving me the wisdom, strength, faith, courage, right directions, and providing for all my needs.

I am greatly indebted to my advisor, Dr. Rakesh K. Kapania, whose enthusiastic guidance, and vast knowledge enlightened me throughout this work. I would like to acknowledge all the truss-braced wing team members, Dr. Bernard Grossman, Dr. Joseph Schetz, Dr. William Mason, Dr. Rakesh Kapania, Dr. Raphael Haftka, Dr. Frank Gern, Philippe-Andre Tetrault, Joel Grasmeyer, Erwin Sulaeman, Jay Gundlach, and Andy Ko, for providing a unique environment of team work and support which would be difficult to obtain otherwise. Also, my thanks are extended to Dr. Dennis Bushnell, Chief Scientist at NASA Langley for providing the financial support of this project and believing in us.

Regards are also due to Dr. Eric Johnson for his thoughtfulness and willingness to serve on my thesis committee. My thanks to my other Virginia Tech professors for contributing their technical expertise and assistance to my future.

I am also grateful to my friends at Virginia Tech especially Philippe, Bragi, Arash, Mohamed, and Stina for their great friendship and support.

I would like to express my warmest appreciation to my parents Shahla and Bahman Naghshineh-Pour whose encouragement, inspiration, life long support, and sacrifices made my life easier and my accomplishment possible. And I would also like to thank my brother for being my best friend throughout my life.

My thanks to my grandmother, relatives, and friends who are always in my mind and will never forget.

Table of Contents

List of Figures

List of Tables

Chapter 1 Introduction

1.1 *Motivation*

Strut-braced wing configurations have been used both in the early days of aviation and today's small airplanes. Adopting very thin airfoil sections needed external wing structural support to sustain aerodynamic loads. However, those external structures cost a significant penalty in drag. Gradually, it was understood that the external bracing could be removed and lower drag could be achieved by replacing the wing-bracing structure with a cantilever wing with an appropriate wing box and thickness to chord ratios.

However, along with the idea of the cantilever wing configuration with its aerodynamic advantages over the external bracing and wire wing configurations, the concept of the truss-braced wing configuration also survived. This is due to the tireless efforts of Werner Pfenninger at Northrop in the early 1950's (Pfenninger, 1954) and his continuation of these efforts until the late 1980's. In the summer of 1996 Dennis Bushnell, Chief Scientist at the NASA Langley Research Center, challenged the Multidisciplinary Analysis and Design (MAD) Center of Virginia Tech to evaluate the feasibility of a truss-braced wing for transonic commercial transport aircraft. Using a strut or a truss offers the opportunity to increase the wing aspect ratio and thus to decrease the induced drag significantly without a great wing weight penalty relative to a cantilever wing. This makes it possible to achieve a long range and meet large payload requirements. Also, a lower wing thickness becomes feasible which reduces the transonic wave drag and hence results in a lower wing sweep. A lower wing sweep and a high aspect ratio produce natural laminar flow due to low Reynolds numbers. Consequently, a significant increase in the aircraft performance is achieved (Joslin, 1998 and Grasmeyer et al., 1998).

1.2 *Multidisciplinary Design Optimization (MDO)*

Multidisciplinary design optimization (MDO) has become remarkably accessible in aircraft preliminary design due to rapid advancements in computer technologies. For a number of years, optimization tools using the sequential approach or the conventional approach, have been employed in preliminary design of aircraft. However, because of poor fidelity of analysis methods, it was rarely used by the industry (Kroo, 1997). Today, improvements in optimization algorithms and modern computers have made it possible to deal with preliminary design with hundreds of design variables from a multidisciplinary point of view (Venkayya et al., 1996). Since in aircraft design aerodynamics, structures, propulsion, stability and control are tightly coupled, especially the somewhat adversarial relationship between the aerodynamics and structures, i.e. thinner wings to achieve low drag and thicker wings to reduce wing bending weight, it is advantageous to investigate the trade-off among these disciplines. The MDO strategy allows simultaneous participation of all the disciplines in the analyses and design rather than in a sequential fashion. Thus, the application of MDO is promising for design of advanced vehicles in which the multidisciplinary interactions are expected to play a dominant role. Although it has a long way to go before maturity, MDO has provided a powerful tool to design these advanced vehicles. This is especially true for unconventional aircraft design, since empirical data and statistical methods are not available. The most recent applications of MDO for the past few years are the High Speed Civil Transport (HSCT) (Giunta et al., 1997 and Korte et al., 1998), Unpiloted Air Vehicle (UAV) (Kroo, 1997), and Blended Wing Body Concept (BWB) (Kroo, 1997), and an industrial application is the development of the Boeing 777 (Kroo, 1997). Also, the work of Bennett et al. (1998) can be mentioned in applications of multidisciplinary optimization in industry.

The aircraft design process can be divided into three steps: conceptual design, preliminary design, and detailed design (Raymer, 1992). So far, the MDO methodology has been applied successfully at the conceptual design stage and up to some levels of preliminary design and detailed design stages. Usually in conceptual design, statistical data or simple models are used for analyses, hence it is convenient

to apply MDO. The design problem is defined parametrically, and then optimization is applied to all the disciplines simultaneously. Thus, the effects of each design variable to all trends is taken into account. Several aircraft optimization design tools such as Flight Optimization System (FLOPS) (McCullers) and Aircraft Synthesis ACSYNT (Vanderplaats, 1976) have been developed for such a purpose.

After selection of a proper design concept, preliminary design employs more detailed analyses with more accurate methods in each discipline such as the finite element method (FEM) for structural analyses and computational fluid dynamics (CFD) for aerodynamic analyses (Korte et al., 1998). Furthermore, aerodynamic and structural behavior of aircraft are inherently very complex and nonlinear (Kroo, 1997). Consequently, linking these methods together in the optimization process with several design variables would require millions of analyses even for one optimization iteration. That makes the process too expensive or impractical to maintain (Kroo et al., 1994), although for a few cases such as the Aerospike Rocket Nozzle (Korte et al., 1998) such advanced analysis approaches in an MDO context have been utilized.

Therefore, to bridge the gap between the simple and advanced methods, approximation methods like response surfaces, design of experiments, and neural networks are commonly employed to approximate detailed methods to build aerodynamic and structural equations. The advantages of these models are to reduce the number of analyses and to remove noise in the analysis methods. These equations could be weight equations for structural design and lift and drag equations for aerodynamic design. Three preliminary design examples using MDO are the Aerospike Rocket Nozzle (Korte et al., 1998), the HSCT (Korte et al., 1998 and Giunta et al., 1997), and design of a commercial transport (Kroo et al., 1994). All show the advantages of MDO over conventional methods. Some commercial structural optimization and CFD packages used at this stage are MSC/NASTRAN (Patel, 1992), GENESIS (Thomas et al., 1991), USM3D (Parikh and Pirzadeh, 1991), and the General Aerodynamic Simulation Program (GASP) (Aerosoft, 1996).

1.3 *Some Previous MDO Aircraft Design Applications*

The MDO approach has been implemented in several aircraft designs. Grossman et al. (1986) investigated the interaction of aerodynamic and structural design of a composite sailplane subject to aeroelastic, structural, and aerodynamic constraints to increase the overall performance. They based their design on two different design approaches, i.e. the conventional design or the sequential design and the multidisciplinary design. They showed that the multidisciplinary design can yield superior results than the sequential design. The Joined-Wing configurations were also studied from the MDO point of view by Wolkovitch (1985), Hajela and Chen (1986), Selberg and Cronin (1986), Kroo and Gallman (1990 and 1992), and Gallman et al. (1993). Other references about Joined-Wing design can be found in the above articles. They introduced a new concept which resulted in better structural and aerodynamic performance compared with conventional cantilever wing configurations. Another example is the application of MDO to a High Speed Civil Transport. The HSCT configuration flies for a range of 5,500 nautical miles at a cruise Mach number of 2.4, while carrying 251 passengers. A significant effort has been made at the Multidisciplinary Analysis and Design (MAD) center of Virginia Tech to perform an MDO of an HSCT. A few methods were developed for the better use of the MDO approach for aircraft conceptual and preliminary design stages. More information about this work can be obtained from Giunta et al. (1996 and 1997), Hutchison et al. (1994), and Knill et al. (1998).

1.4 *Previous Strut-Braced Wing Studies*

Previously, a number of Strut-Braced Wing aircraft configurations have been investigated. In continuing Pfenninger's work, Kulfan and Vachal (1978) from the Boeing Company performed preliminary design and evaluated the performance of a large turbulent subsonic military airplane. Moreover, they compared the performance and economics of a cantilever wing configuration with a strut-braced wing configuration. The design mission of the transport has a range of 10,000 nautical miles, payload of 350,000 *lbs*, and takeoff field length of 9,000 *ft* while the Mach

number was determined from tradeoff studies. Two load conditions, i.e. 2.5g maneuver and 1.67 taxi bump were used to perform structural analyses. Their optimization and sensitivity analyses showed that high aspect ratio wings with low thickness to chord ratios would result in a significant fuel consumption reduction. For their case the wing sweep was a less important parameter. Also, for the cantilever configuration a ground strike problem arose during taxiing. This issue was resolved by adding a strut to the wing structure. Moreover, their high fidelity analysis results indicated that the strut-braced wing configuration requires less fuel (1.6%), lower takeoff gross weight (1.8%), and lower empty weight (3%) than the cantilever wing configuration. Furthermore, the cost comparisons showed that the operating costs of the strut-braced wing configuration were also slightly less than those of the cantilever wing configuration because of a lower takeoff gross weight. Also, Park (1978) from the Boeing Company compared the block fuel consumption of a strutted wing versus a cantilever wing. A mission profile with a range of two 500-statue-mile stages including adequate reserve, a payload of 20,000 *lbs*, a cruise speed of 300 *mi/hr* at 25,000 *ft*, and takeoff and landing fields of 4,500 *ft* was considered. Even though he concluded that the use of a strut saves wing structural weight, the significant increase in the strut *t/c* to cope with its buckling at the -1.0g load condition increased the strut drag and hence did not appear practical for this type of transport category aircraft due to its higher fuel consumption compared to the cantilever case. Another study on strut-braced wing configurations was conducted by Turriziani et al. (1980). They addressed the fuel efficiency advantages of a strut-braced wing business jet employing an aspect ratio of 25 over an equivalent conventional wing business jet with the same payload range. They concluded that the strut-braced wing configuration reduces the total aircraft weight, even though the wing and strut weight will increase compared to the cantilever wing case. This is due to aerodynamic advantages of high aspect ratio wings. Furthermore, the results showed a fuel weight savings of 20%.

1.5 *Current Truss-Braced Wing Study*

In June 1996, a research program was begun at the MAD center at Virginia Tech to evaluate the benefits of the truss-braced wing configuration at the request of the NASA Langley Research Center. A team consisting of five faculty members, Dr. Bernard Grossman, Dr. William H. Mason, Dr. Rakesh K. Kapania, Dr. Joseph A. Schetz, and Dr. Raphael T. Haftka (University of Florida), and three graduate students, Philippe-Andre Tetrault (CFD and interference drag analyses), Joel M. Grasmeyer (general aerodynamics, performance, stability and control, and propulsion), and the author (structural analyses), began the work in earnest. Later in April 1998, Lockheed Martin Aeronautical Systems (LMAS), with Virginia Tech as a subcontractor, received a contract from the NASA Langley Research Center to further investigate the truss-braced wing concept. At this stage, Erwin Sulaeman (aeroelasticity), Dr. Frank Gern (structures and aeroelasticity), Jay Gundlach (MDO and aerodynamics), and Andy Ko (MDO software engineering and aerodynamics) joined the team.

The objective is to exploit truss-braced wing concepts in combination with advanced technologies to improve the performance of transonic transport aircraft. The truss topology introduces several opportunities. A high aspect ratio and decreased wing thickness can be achieved without an increase in wing weight relative to a cantilever wing. The increase in the aspect ration will result a decrease in the induced drag. The reduction in thickness allows the wing sweep to be reduced without incurring a transonic wave drag penalty. The reduced wing sweep allows a larger percentage of the wing area to achieve natural laminar flow. Additionally, tip-mounted engines can be used to reduce the induced drag. A Multidisciplinary Design Optimization (MDO) approach is used to obtain the best technology integration in structural analyses, aerodynamics, and controls of the truss-braced wing aircraft (Grasmeyer et al., 1998).

A Lockheed Martin Aeronautical Systems' (LMAS) mission profile with a range of 7,500 nmi at Mach 0.85 with 325 passengers in a three-class configuration with an additional 500 nmi of cruise for reserve fuel requirements is considered. So far, a

single-strut configuration has been used to represent the most basic truss configuration.

Several different modules for aerodynamics, structures, and stability and control have been built and integrated. The commercial optimization software, Design Optimization Tools (DOT) (Vanderplaats Research & Development, Inc., 1995), is utilized for optimization to minimize the maximum takeoff weight of the configuration subject to defined constraints. The weight equations except for wing bending material weight from NASA Langley's Flight Optimization System (FLOPS) (McCullers) are used to estimate the aircraft weight. First, an optimum cantilever design is obtained from the baseline LMAS design for the advanced technology. Then, strut-braced wing designs are obtained for the same technology and compared with the optimum cantilever design to address the differences. Moreover, two design configurations, i.e. tip-mounted and under-wing engines, are considered in this study.

Also, CFD analyses have been performed by Tetrault and Schetz at Virginia Tech to design the strut-braced wing for minimum wing-strut interference drag in the transonic flow regime. No detailed analysis in this category is available in the literature. Only, the work of Hoerner (1965) can be mentioned for evaluating the interference drag for various strut-wall intersections in subsonic flow. The interference drag in transonic flow regimes is expected to be more significant than the results obtained from Hoerner (1965) studies for subsonic flow regimes. Thus, for the current work, an equation to estimate the wing-strut interference drag from the off-line CFD analyses has been customized by Tetrault and Schetz for use in the MDO code. For the strut-fuselage junction, an equation derived by Hoerner (1965) is used. For more detailed studies general aerodynamics, performance, stability and control, and propulsion refer to Grasmeyer (1997) and (1998).

The purpose of this thesis is a preliminary structural design and bending material weight estimation for a strut-braced wing. First, the bending material weight estimation using the piecewise linear load method is discussed and then an

introduction to detailed analysis and weight estimation using the finite element method will be presented.

Two sets of results based on tip-mounted and under-wing engine configurations are carried out. The results are tabulated, illustrated, and discussed.

The truss-braced wing has a high aspect ratio and is made of thin airfoil sections. Preliminary studies showed that the wing may undergo large deformations at critical maneuver load conditions. Thus, static aeroelastic effects should be considered in the future to account for more realistic aerodynamic load distributions.

1.6 *Overview*

This work investigates the structural behavior and bending material weight estimation of strut-braced wing configurations. The objective and different strut-braced configuration arrangements are given in Chapter 2. In Chapter 3, structural formulation and modeling, critical load conditions, the wing weight estimation method, and model validation of the strut-braced wing are introduced and discussed in detail. The optimization problem, the objective function, and the constraints are presented in Chapter 4. Results, discussions, and comparisons on different strut-braced wing configurations are tabulated, discussed, and illustrated in Chapter 5. In Chapter 6, an introduction to static aeroelastic analysis using the finite element method, strut-braced wing finite element modeling, and preliminary static aeroelastic results are elaborated. And finally, concluding remarks and recommendations for the future work are presented in Chapter 7. Wing weight equations in FLOPS and a code description are given in Appendix A and Appendix B, respectively.

Chapter 2 Strut-Braced Wing Configurations

2.1 *Objective*

The objective of this study encompasses a multidisciplinary design optimization of a strut-braced wing aircraft to minimize the maximum takeoff weight according to the aforementioned mission profile. The aircraft wing is designed to operate at the 2.5g and -1.0g $\times$ factor of safety of 1.5 maneuver load conditions and a 2.0g taxi bump load condition. These symmetrical critical loads are adopted to determine the wing bending material weight according to load factors per FAR 25.337(b) and (c) for commercial transport aircraft (Lomax, 1996).

The weight equations from NASA Langley's Flight Optimization System (FLOPS) are used to estimate most of the structural weight and all of the non-structural weight (McCullers). Because there is little wing weight data available for high aspect ratio truss-braced wing commercial transports, and since FLOPS only uses an empirical correction factor to account for strut-bracing, structural analyses and bending material weight estimation were conducted to provide a proper means to the multidisciplinary design of the truss-braced wing. The bracing factor in FLOPS was adopted from available statistical data from strut-braced wing aircraft and cannot be used for the current strut-braced wing analysis due to different structural design concepts. Previous comparisons between FLOPS strut-braced wing bending material weight and that of the strut-braced wing recent analysis showed a considerable difference. A more detailed analysis using a piecewise linear load model has been adopted to estimate the wing bending material weight and substituted for that value in FLOPS. Replacing the bending material weight from FLOPS with other estimates has been done in High Speed Civil Transport research at Virginia Tech for several years (Dudley et al., 1995).

2.2 *Studied Design Procedures*

Two maneuver load conditions 2.5g and -1.0g × safety factor and a 2.0g taxi bump load condition are used to determine the wing bending material weight (Lomax, 1996). Preliminary calculations showed that the landing load condition would not be critical. Three different designs have been considered:

1. A design consisting of a cantilever wing with a supporting strut. The existence of the strut causes the structure to be statically indeterminate.
2. A design consisting of a hinged support wing and a supporting strut.
3. A design consisting of a cantilever wing with a force-controlled supporting strut.

Coster and Haftka (1996) showed that for a truss-braced wing subjected to negative maneuvers a significant weight penalty is required to prevent the strut from buckling in the -1.0g load condition. They compared the buckling weights of strut-braced wing configurations with those of truss-braced wing configurations to explore the effects of buckling on different configurations. The results revealed that using a truss would reduce the weight penalty approximately by 50%, but this is still too large. Hence, to eliminate the weight penalty due to strut buckling a different design philosophy was adopted.

The second design assumes a one-way hinge at the wing root. This means that the wing configuration consists of a hinged support wing incorporating a resisting strut for positive maneuvers and a cantilever wing with no strut for negative maneuvers and the taxi bump load condition.

The third design assumes a clamped wing for all load conditions. The strut is assumed to be inactive in compression during the -1.0g load condition. However, during positive g maneuvers, the strut remains active. Since the wing is clamped to the fuselage, it acts like a cantilever beam in negative load conditions and as a strut-braced beam in positive load conditions. This could be done by a telescoping sleeve mechanism on the strut. Moreover, the strut force is obtained by the global optimizer to minimize the bending material weight at the 2.5g load condition. Other features

such as a slack distance and a strut offset have been added to the wing structure for structural and aerodynamic reasons. This design approach results in a significant reduction in the bending material weight compared to configurations 1 and 2. Thus, it was chosen for further studies.

The bending material weight model idealizes the wing as a beam with properties varying along the span. Because the strut force and the spanwise wing-strut intersection position are design variables, the beam can be treated as a statically determinate structure. This means that one can calculate the bending moment distribution by simple quadrature and calculate the required panel thickness directly, thus making the structural optimization very easy.

To put tension forces on the strut during the positive maneuvers, a high-wing configuration is employed. In this way, the strut will be more beneficial to reduce weight according to the adopted configuration. Moreover, a high wing will avoid adverse transonic flow interference on the upper surface with a truss placed in the supersonic flow region.

In the preliminary studies of a truss-braced wing, we direct our attention to only single-strut-braced wing configurations which are a special case within the general class of truss-braced wing configurations. The wing is assumed to be manufactured of a high strength aluminum alloy. The effect of composite materials is studied by multiplying the wing weight by a "technology factor". The wing box consists of upper and lower skin panels. The wing is subjected to lift distribution loads obtained from the aerodynamic analyses.

2.3 *Strut-Braced Wing Design Configurations*

Figure 2.1 shows some of the single-strut configurations. The strut-braced wing is a clamped beam at the root with a supporting strut. A strut is employed to avoid wing weight penalty due to the high aspect ratio and small thickness to chord ratios.

However, the supporting strut would be vulnerable to strut buckling at the -1.0g load condition which would result in a very heavy strut. Although this phenomenon is highly dependent on the wing-strut location and different strut configurations, preliminary studies showed that a cantilever wing would be more efficient both structurally and aerodynamically if the strut was designed to sustain the buckling. To bridge this dilemma, an innovative design strategy was adopted.

Moreover, the wing-strut junction is anticipated to produce considerable interference drag if the wing and strut make a small angle. This undesirable drag can be reduced dramatically by increasing the junction angle to 90° according to Tetrault and Schetz's investigation. Thus, a strut offset is added to the strut structure to address the interference drag issue. Furthermore, tip-mounted engines lead to a further reduction in induced drag (Grasmeyer et al., 1998). Under-wing engines have also been investigated .

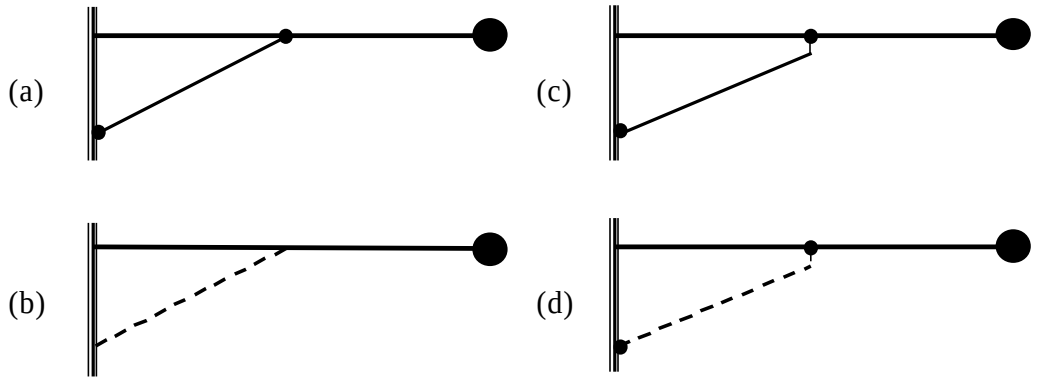

Figure 2.1 Strut-braced wing design configurations (a) strut in tension with no offset (b) strut in compression with no offset (c) strut in tension with offset (d) strut in compression with offset.

2.3.1 Strut Configuration Arrangement

To eliminate the weight penalty due to strut buckling, the strut is assumed to be inactive during the -1.0g maneuver and 2.0g taxi bump load conditions. To address this matter, several different types of mechanisms can be used. A telescoping sleeve

mechanism was found suitable for the current design purposes. This strut arrangement was suggested by Dr. R.T. Haftka. During positive g maneuvers, the strut is in tension. Since the wing is clamped to the fuselage, it acts as a cantilever beam in the negative load conditions and as a strut-braced beam in the positive load maneuvers. Moreover, the strut force (the force carried by the strut) at the 2.5g load condition is optimized to provide the minimum total wing bending material weight. Figure 2.2 shows a conceptual sketch of typical variations of the strut force versus the wing weight for different wing-strut intersection locations.

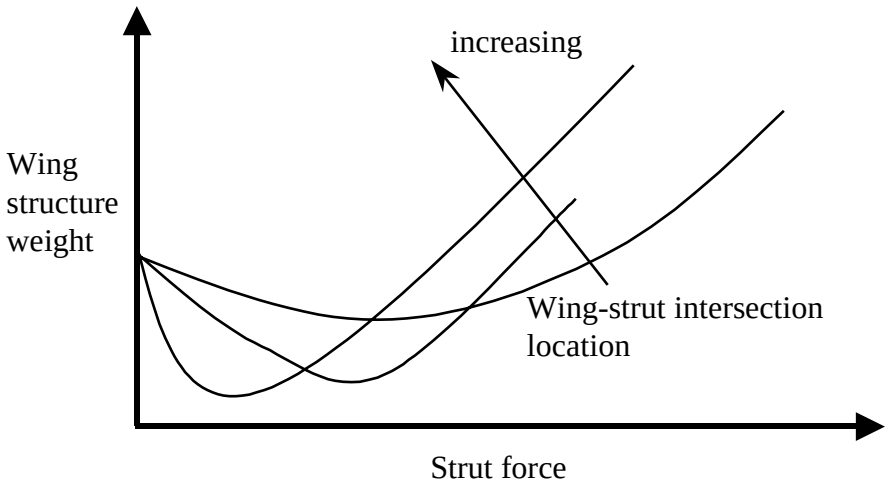

Figure 2.2 Variation of the strut force versus the wing weight at different wing-strut intersection locations.

On a typical optimum single-strut design, this means that the strut would first engage in tension at some positive load factor by defining a slack distance in the wing-strut mechanism arrangement to reach the optimum strut force at the 2.5 load factor. The load factor that the strut engages will be referred to as the slack load factor. Furthermore, the optimum strut force at 2.5g's is different from the strut force that would be obtained at 2.5g's if the strut engaged immediately at 0g (this could be thought of as the pre-force or jig-shape force). It is important to have the slack load factor always positive otherwise the strut would be under a pre-load condition at the jig shape to achieve the optimum strut force. The relationship between the strut force and the strut length displacement is shown in Figure 2.3. When the wing is subjected

to the 2.5g maneuver, first the strut extends as much as the slack distance without carrying any tension load and then engages. When the load factor reaches to 2.5 the strut carries the optimum strut designed force for minimum wing bending material weight. The strut is designed the way that it will not carry aerodynamic forces during the cruise condition. However, it will carry air loads during 2.5g and -1.0g maneuvers. Figure 2.4 shows the telescoping sleeve mechanism.

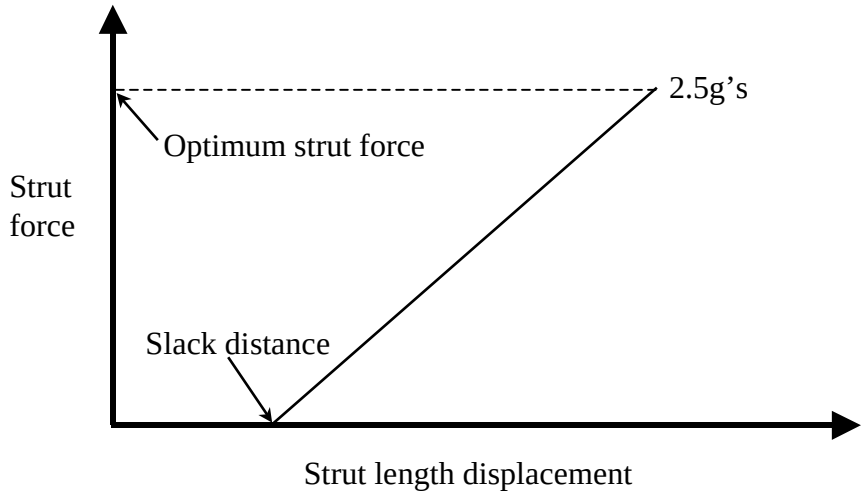

Figure 2.3 Strut force versus strut length displacement.

Also, a strut offset, as shown in Figure 2.5, is designed to achieve a few objectives: (1) A reduction in aerodynamic wing-strut interference drag, (2) Simulation of an arch-shaped strut configuration (see the future work in Chapter 7), and (3) Alleviation in the bending moment due to the lift load. The vertical offset member is subjected to high bending loads and is designed for a combined bending-tension loading. In this context, the horizontal component of the strut force is of a special concern. Since this horizontal force results in a considerable bending moment on the offset piece, its weight increases dramatically with increasing the strut force and offset length. As a result, it is imperative to employ MDO tools to obtain optimum values for the vertical offset, strut force, and spanwise wing-strut intersection. That way, it will be possible to accommodate the two contrary design requirements which are: (1) A reduced offset length to reduce strut loading and (2) An increased offset length to reduce the wing-strut interference drag.

This design approach results in a significant reduction in bending material weight compared to a wing in which a completely rigid strut is designed to withstand the buckling loads.

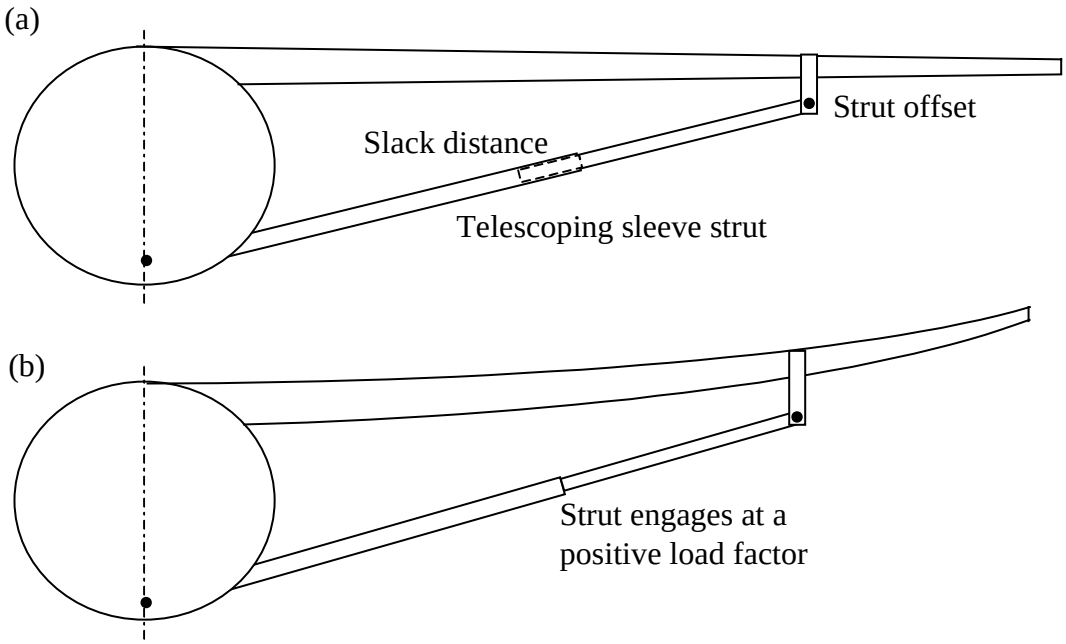

Figure 2.4 The clamped wing with a supporting telescoping sleeve strut (a) Strut inactive in compression (b) Strut engages at a positive load factor.

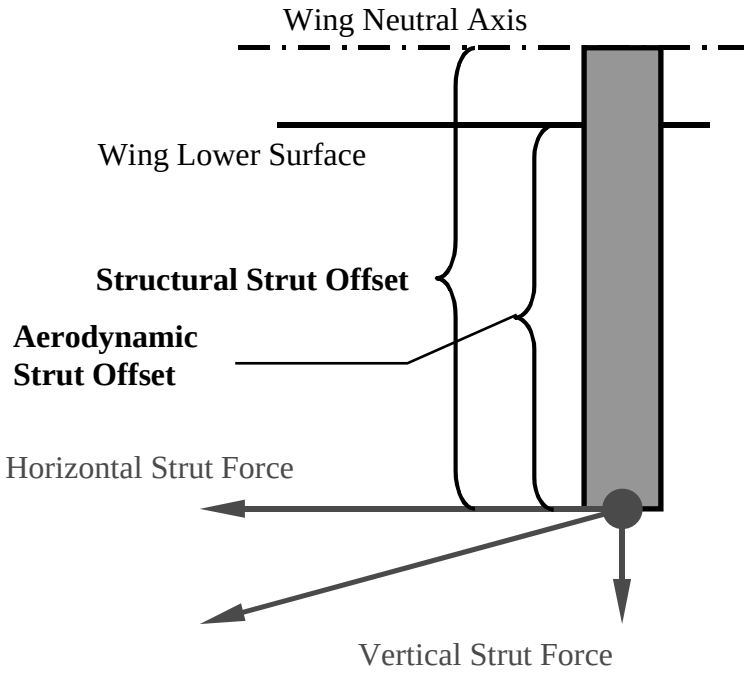

Figure 2.5 Strut offset member and applied loads.

Chapter 3 Structural Formulation and Modeling

A simple double-plate model using the piecewise load method has been employed to idealize the structural wing box and evaluate the wing bending material weight for the cantilever and strut-braced wing configurations. Because of symmetry, only a half wing is modeled. A FORTRAN code has been developed to perform the analyses. For more details, see Appendix B. The code imports all the wing geometry parameters and aerodynamic loads from the MDO code and calculates the wing bending material weight and then exports it to the MDO code. In the following sections, the structural formulation and modeling of the wing are described.

3.1 *Problem Formulation*

A single-strut-braced wing with loading is shown in Figure 3.1. To simplify the analyses, only the stiffness component in the *z*-direction is accounted for. The stiffness can be obtained from the stiffness matrix of a truss member. By assuming only the displacement in the *z*-direction for the strut at the wing-strut attachment and other displacements in the *x*- and *y*-directions to be zero, the equivalent stiffness is obtained as:

$$K = \frac{A_s E_s}{L_s} \sin^2 \varphi, \tag{3.1}$$

where K denotes the equivalent stiffness matrix, A_s denotes the strut cross-sectional area, E_s denotes strut material Young's modulus, L_s denotes the strut length, and φ denotes the angle between the strut and the wing at the attachment.

To perform the analyses, it is advantageous to use non-dimensional parameters thus we non-dimensionalize the parameters with respect to *b/2* and q_0 where *b/2* is the

wing half span in (*ft*) and q_0 is the load at the wing root in (*lbs/ft*). Therefore, the displacements, forces, and moments can be non-dimensionalized as follows:

$$\overline{Length} = \frac{Length}{b/2}, \quad \overline{Force} = \frac{Force}{q_0 b/2}, \quad \overline{Moment} = \frac{Moment}{q_0 (b/2)^2}, \tag{3.2}$$

where $\overline{Length}$ and *Length* are general non-dimensional and dimensional displacements, respectively, $\overline{Force}$ and *Force* are general non-dimensional and dimensional forces, respectively, and $\overline{Moment}$ and *Moment* are general non-dimensional and dimensional moments, respectively. All other parameters can be non-dimensionalized accordingly.

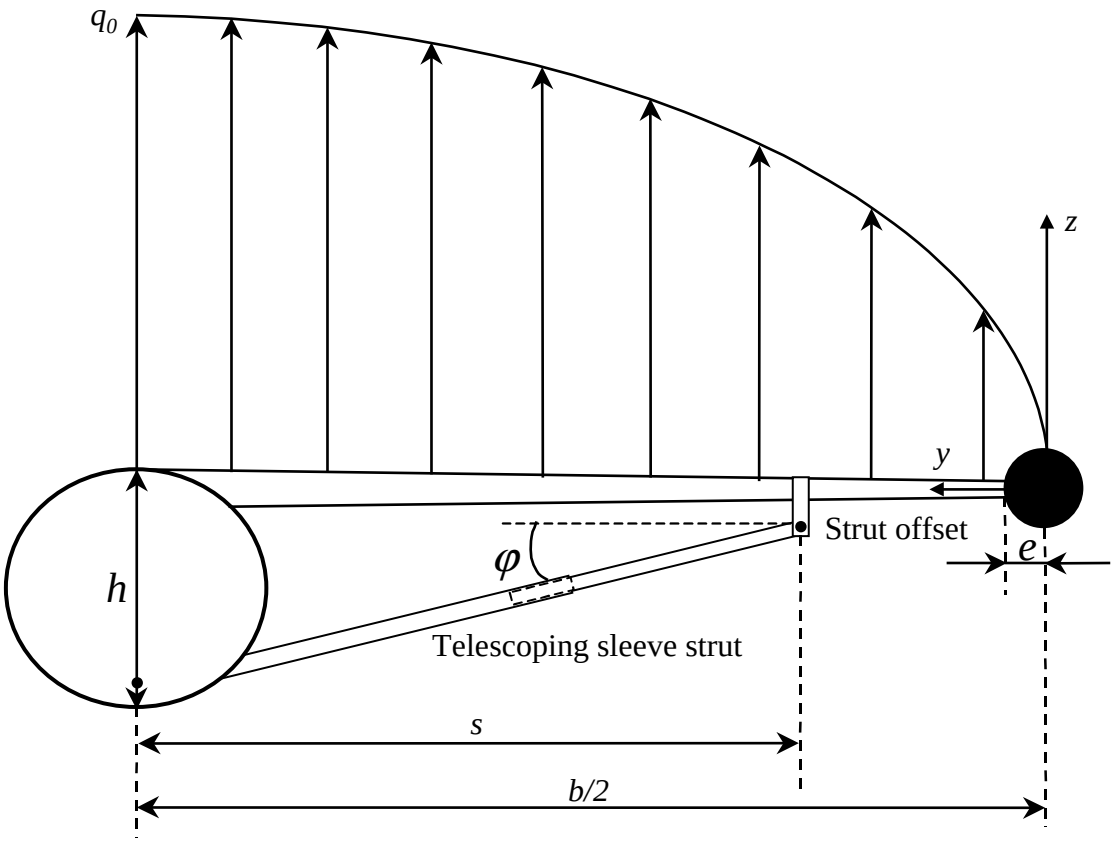

Figure 3.1 Strut-braced wing configuration with loading.

Two methods based on the linear load method are employed for strut-braced wing structural analyses. They are:

1. Direct integration method
2. Piecewise load method.

The direct integration method is used to develop the equations for the piecewise method. To derive the equations for both cases

- The Euler-Bernoulli beam theory is used.
- Aerodynamic loads and wing geometry parameters are imported from the MDO code.

To account for the realistic lift distribution obtained from the aerodynamic analysis module, the wing is divided into several segments. Also, structural nodes are defined to separate the nodes used in the structural analyses from those of aerodynamic analyses. For each segment, the load values at both structural nodes are obtained by interpolating the load values of the aerodynamic nodes from the aerodynamic analysis module using linear Lagrange Polynomials to obtain the load distribution as shown in Figure 3.2.

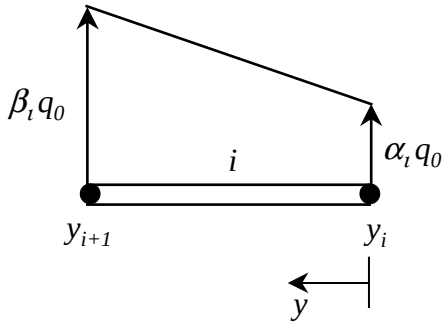

Figure 3.2 Local coordinates and load distribution.

A local lift distribution can be written:

$$q_i(y) = q_0\left(\frac{(y - y_{i+1})}{(y_i - y_{i+1})}\alpha_i + \frac{(y - y_i)}{(y_{i+1} - y_i)}\beta_i\right), \tag{3.3}$$

where $q_i(y)$ denotes the local lift distribution for element *i*, α_i and β_i denote the lift coefficients at nodes *i* and *i+1* , and y_i and y_{i+1} denote the node coordinates in the *y*-direction. The piecewise model in global coordinates is shown in Figure 3.3.

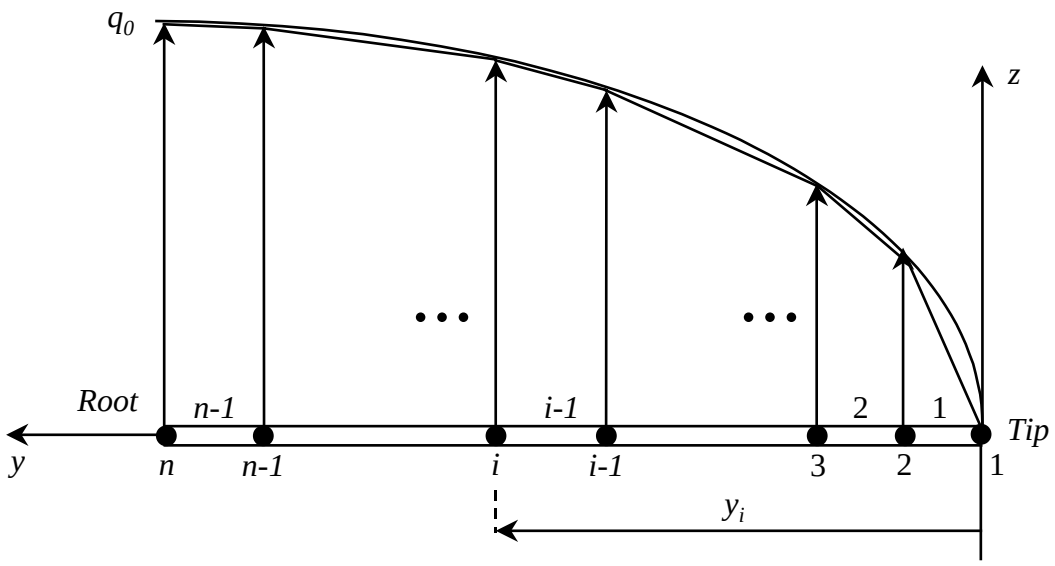

Figure 3.3 Piecewise representation of the aerodynamic loads.

3.1.1 Derivation of Structural Equations Using the Direct Integration Formulation

As previously discussed, the structure consists of a cantilever wing with a telescoping sleeve strut at the 2.5g load condition for which an optimum strut force is given by the optimizer and a cantilever wing without a supporting strut at the -1.0g load condition. Thus, for both load conditions the structure is statically determinate. Due to different boundary conditions and the structural configurations, there are two derivations considered for this formulation. They are: (1) the 2.5g load condition and (2) the -1.0g load condition.

3.1.1.1 The 2.5g Load Condition

To derive the mechanics equation for the wing, first the unit step function is defined as follows:

$$u(y) = \begin{cases} 0 & \text{if} \quad y < 0 \\ 1 & \text{if} \quad y \geq 0 \end{cases}. \tag{3.4}$$

The shear force and bending moment distributions can be obtained from the following equations:

$$V(y) = W_e u[y - (b/2 - y_e)] + F_{sv} u[y - (b/2 - s)] - \int_0^y q(y)dy, \tag{3.5}$$

$$\begin{aligned} M(y) = -V(y)y - W_e e u[y - (b/2 - y_e)] + F_{sv}(b/2 - s)u[y - (b/2 - s)] - \\ \int_0^y yq(y)dy + W_e(b/2 - y_e)u[y - (b/2 - y_e)] + F_{sh}L_{off}u[y - (b/2 - s)], \end{aligned} \tag{3.6}$$

where $V(y)$ indicates the shear force, F_{sv} indicates the strut force in the *z*-direction, F_{sh} indicates the strut force in the *y*-direction, *s* indicates the wing-strut intersection distance from the wing root, W_e indicates the engine weight, y_e indicates the engine position from the root, L_{off} indicates the strut offset length, and $M(y)$ indicates the bending moment.

The boundary conditions of the structure are defined

$$\theta(b/2) = 0,\ w(b/2) = 0, \tag{3.7}$$

where $\theta(b/2)$ is the rotation of the wing at the wing root, and $w(b/2)$ is deflection of the wing at the wing root.

Using the governing differential equation of beams, the wing rotation is expressed as:

$$\theta(y) = \int_0^y \frac{M(y)}{EI(y)} dy + c_1 \tag{3.8}$$

where $\theta(y)$ is the wing rotation and $EI(y)$ is the flexural rigidity of the wing.

Integrating equation (3.8), the equation for wing deflections is obtained as:

$$w(y) = \int_0^y \theta(y) dy + c_1 y + c_2, \tag{3.9}$$

where $w(y)$ is the deflection of the wing, and c_1 and c_2 are the coefficients to be determined by the boundary conditions.

3.1.1.2 The -1.0g Load Condition

The boundary conditions at this load condition are:

$$\theta(b/2) = 0 \text{ and } w(b/2) = 0, \tag{3.10}$$

where $\theta(b/2)$ and $w(b/2)$ denote the rotation and deflection of the wing at the root, respectively.

The shear force and bending moment equations are obtained as:

$$V(y) = -W_e u[y - (b/2 - y_e)] + \int_0^y q(y) dy, \tag{3.11}$$

$$M(y) = -V(y)y + W_e e u[y - (b/2 - y_e)] + \int_0^y yq(y) dy - W_e (b/2 - y_e) u[y - (b/2 - y_e)]. \tag{3.12}$$

The rotation and deflection equations can be readily derived from the beams governing equation analogous to equations (3.8) and (3.9).

3.1.2 Derivation of Structural Equations Using the Piecewise Formulation

A piecewise formulation is used herein to account for the actual lift distributions. Figure 3.3 depicts the piecewise model. The wing is divided into several segments and for each segment the shear force, bending moment, and bending material weight are evaluated. Two sets of formulations are also obtained for the two load cases, i.e. 2.5g's and -1.0g.

3.1.2.1 The 2.5g Load Condition

The boundary conditions are identical to those of the direct integration method. Linear interpolation is utilized to obtain the load distribution at the structural nodes from the aerodynamic analysis. The shear force and bending moment for the i^{th} element is expressed as:

$$V_i(y) = F_{sv}u[y-(b/2-s)]+W_e u[y-(b/2-y_e)]- \sum_{i=1}^{i-1}\int_{y_j}^{y_{j+1}} q_i(y)dy - \int_{y_i}^{y} q_i(y)dy. \tag{3.13}$$

$$M_i(y) = -W_e e u[y-(b/2-y_e)]- \sum_{j=1}^{i-1}\int_{y_j}^{y_{j+1}} yq_j(y)dy - \int_{y_i}^{y} yq_i(y)dy + F_{sv}(b/2-s)u[y-(b/2-s)]-V_i(y)y + W_e(b/2-y_e)u[y-(b/2-y_e)]+F_{sh}L_{off}u[y-(b/2-s)]. \tag{3.14}$$

3.1.2.2 The -1.0g Load Condition

The shear force and bending moment equations for the i^{th} element are obtained as:

$$V_i(y) = -W_e u[y-(b/2-y_e)]+\sum_{i=1}^{i-1}\int_{y_j}^{y_{j+1}} q_i(y)dy + \int_{y_i}^{y} q_i(y)dy\,, \tag{3.15}$$

$$M_i(y) = W_e e u[y-(b/2-y_e)]+\sum_{j=1}^{i-1}\int_{y_j}^{y_{j+1}} yq_j(y)dy + \int_{y_i}^{y} yq_i(y)dy - V_i(y)y - W_e(b/2-y_e)u[y-(b/2-y_e)]. \tag{3.16}$$

It is essential to mention that the engine weight multiplied by the load factor is always in the opposite direction of the maneuver loads. This phenomenon produces inertia relief in the bending material weight of the wing.

3.1.2.3 Slope and Deflection Formulation

The slope and deflection equations for the i^{th} element are carried out as:

$$\theta_i(y_i) = \theta_{i+1}(y_{i+1}) - \int_{y_i}^{y_{i+1}} \frac{M_i(y)}{EI_i(y)} dy\,, \tag{3.17}$$

$$W_i(y_i) = W_{i+1}(y_{i+1}) - \int_{y_i}^{y_{i+1}} \left(\int_{y_i}^{y} \frac{M_i(y)}{EI_i(y)} dy \right) dy - \theta_i(y_i)(y_{i+1} - y_i)\,. \tag{3.18}$$

The integration constants were obtained from the boundary conditions.

3.1.3 Moment of Inertia Distribution

In order to maintain generality, we assume that the *EI* distributions vary along the wing. Figure 3.4 shows a linear variation of the chord along the wing. The wing thickness is also assumed to vary linearly along the wing. Since the wing is built with thin airfoils, an idealized wing box or a double-plate model was found suitable to simulate the wing box airfoils as shown in Figure 3.5. This model is made of upper and lower wing skin panels which are assumed to resist the bending moment. The double-plate model offers the opportunity to extract the material thickness distribution by a closed-form equation. The cross-sectional moment of inertia of the wing box can be expressed as:

$$I(y) = \frac{t(y)c_b(y)d^2(y)}{2}, \tag{3.19}$$

where *t(y)* is the wing skin thickness, $c_b(y)$ is the wing box chord, and *d(y)* is the wing airfoil thickness. All parameters are shown in Figure 3.4 and Figure 3.5.

The equations for $c_b(y)$ and *d(y)* are obtained using linear interpolation between the wing root, break, and tip data as:

$$\text{for } b/2-s \le y \le b/2, \quad c_b(y) = c_{b0}\left[\frac{(\gamma_1 - 1)}{s}(b/2-y)+1\right], \tag{3.20}$$

for $0 \le y \le b/2-s$,

$$c_b(y) = c_{b0}\left[\frac{2}{b}\left(\xi_1 + \frac{\xi_1 s - \gamma_1 b/2}{b/2-s}\right)(b/2-y) + \left(\frac{\gamma_1 b/2 - \xi_1 s}{b/2-s}\right)\right], \tag{3.21}$$

where c_{b0} is the wing box root chord, γ_1 is the chord coefficient at the wing-strut attachment, and ξ_1 is the wing box tip chord coefficient, and

$$\text{for } b/2-s \le y \le b/2, \quad d(y) = d_0\left[\frac{(\gamma_2 - 1)}{s}(b/2-y)+1\right], \tag{3.22}$$

and for $0 \le y \le b/2-s$,

$$d(y) = d_0\left[\frac{2}{b}\left(\xi_2 + \frac{\xi_2 s - \gamma_2 b/2}{b/2-s}\right)(b/2-y) + \left(\frac{\gamma_2 b/2 - \xi_2 s}{b/2-s}\right)\right], \tag{3.23}$$

where d_0 is the wing root thickness, γ_2 is the thickness coefficient at the wing-strut attachment, and ξ_2 is the wing tip thickness coefficient.

Now using equation (3.19), the $EI(y)$ distribution is obtained as:

for $b/2-s \le y \le b/2$,

$$EI(y) = EI_0\left[\frac{(\gamma_1 - 1)}{s}(b/2-y)+1\right]\left[\frac{(\gamma_2 - 1)}{s}(b/2-y)+1\right]^2, \tag{3.24}$$

and for $0 \le y \le b/2-s$,

$$EI(y) = EI_0\left[\frac{2}{b}\left(\xi_1 + \frac{\xi_1 s - \gamma_1 b/2}{b/2 - s}\right)(b/2 - y) + \left(\frac{\gamma_1 b/2 - \xi_1 s}{b/2 - s}\right)\right] \left[\frac{2}{b}\left(\xi_2 + \frac{\xi_2 s - \gamma_2 b/2}{b/2 - s}\right)(b/2 - y) + \left(\frac{\gamma_2 b/2 - \xi_2 s}{b/2 - s}\right)\right]^2, \quad (3.25)$$

where $EI_0 = Et(y)c_{b0}d_0^{\,2}/2$.

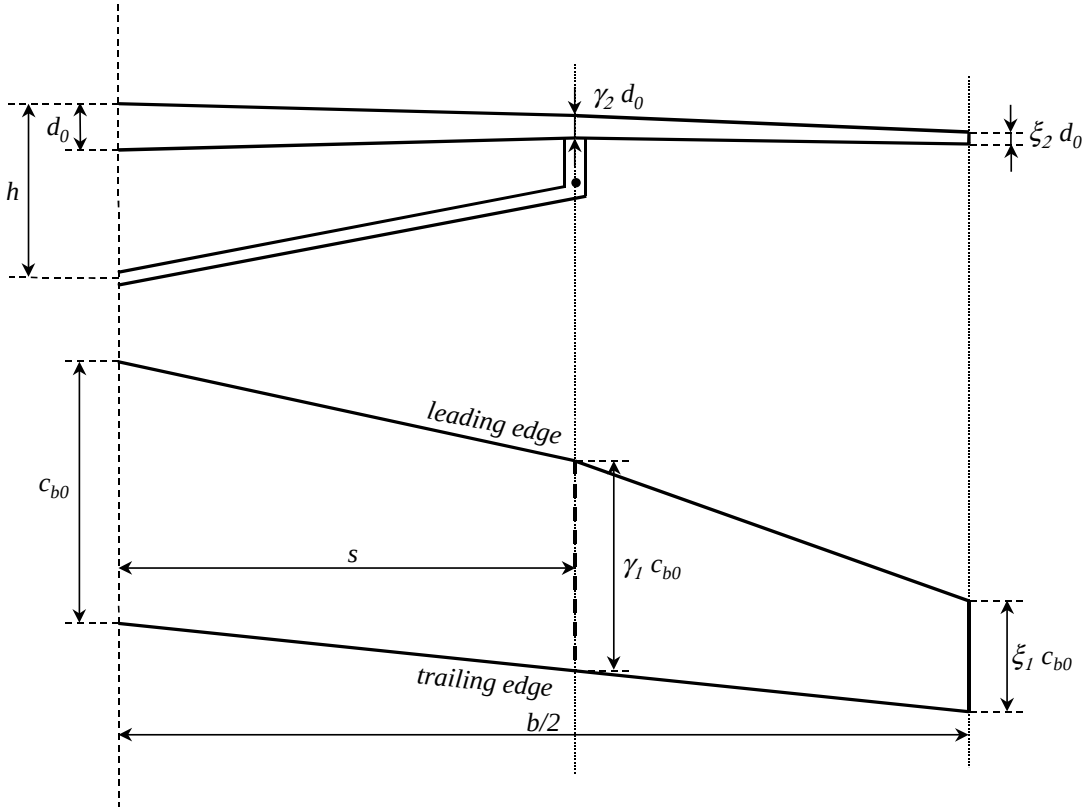

Figure 3.4 Wing planform and geometry parameters.

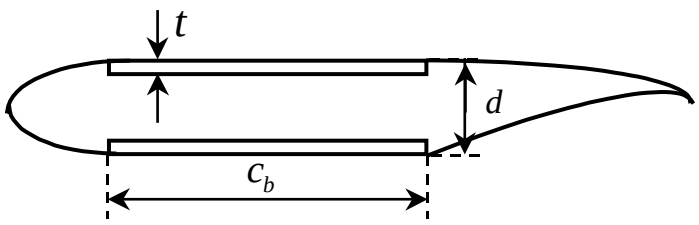

Figure 3.5 Idealized wing box (double-plate model).

3.2 *Taxi Bump Analysis*

Taxi loads are shown in Figure 3.6. In the figure, W_e denotes the engine weight, W_s denotes the strut weight, W_w denotes the wing weight, W_f denotes the fuel weight, and n_t denotes the taxi load factor. Although the taxi bump condition may not be a critical load case for traditional wing configurations such as the Boeing 747 wing, the preliminary results and other studies (Kulfan and Vachal, 1978) showed an area of concern in the taxi bump condition for the strut-braced wing. Since the strut-braced wing configurations have high aspect ratios with thin airfoil sections this condition could be critical. Thus, this load condition was adopted as one of the critical load conditions to calculate the bending material weight. A load factor of 2.0g is used for the analysis (Lomax, 1996).

To summarize the taxi analysis procedure, in general, two different material thickness distributions are obtained. The first one is based on the fully stressed criterion to resist the bending moment due to the taxi loads and the second is based on the wing ground strike displacement constraint. Figure 3.7 shows the taxi analysis scheme. The structural equations for the taxi load condition are analogous to those of the maneuver load conditions. Moreover, to obtain the taxi loads, first the total wing weight due to the maneuver load conditions is calculated from the current bending material weight estimation method and FLOPS wing weight equations, and then it is added to the fuel weight. Finally, all masses are multiplied by the taxi load factor. The wing weight estimation procedure used in FLOPS is given in Appendix A.

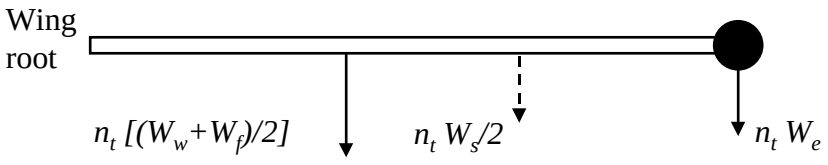

Figure 3.6 Taxi loads.

Furthermore, to prevent wingtip or engine ground strikes during taxiing, an optimization procedure to limit wing vertical deflections is used to obtain an optimum

wing material thickness distribution. Hence, a displacement limit based on the landing gear length and the fuselage diameter is imposed to avoid such problems. This matter will be discussed in the next section in more detail. The maximum vertical displacement during taxiing is calculated for tip-mounted and under-wing engines from the following equations. Obviously, for the tip mounted-engine configuration, the wingtip should be checked for ground strikes while for the under-wing engine configuration, most likely the engine mounting location would be the case to be checked. Thus, for tip-mounted engines:

$$\delta_{tip} = \delta_{wingtip} + \frac{d_{nacelle}}{2}, \tag{3.26}$$

and for under-wing engines:

$$\delta_{engine-\max} = \delta_{wing-engine} + h_{pylon} + d_{nacelle}, \tag{3.27}$$

where $\delta_{wingtip}$ denotes the wingtip deflection, $d_{nacelle}$ denotes the nacelle diameter, $\delta_{wing-engine}$ denotes the wing deflection at the engine location, and h_{pylon} denotes the pylon height.

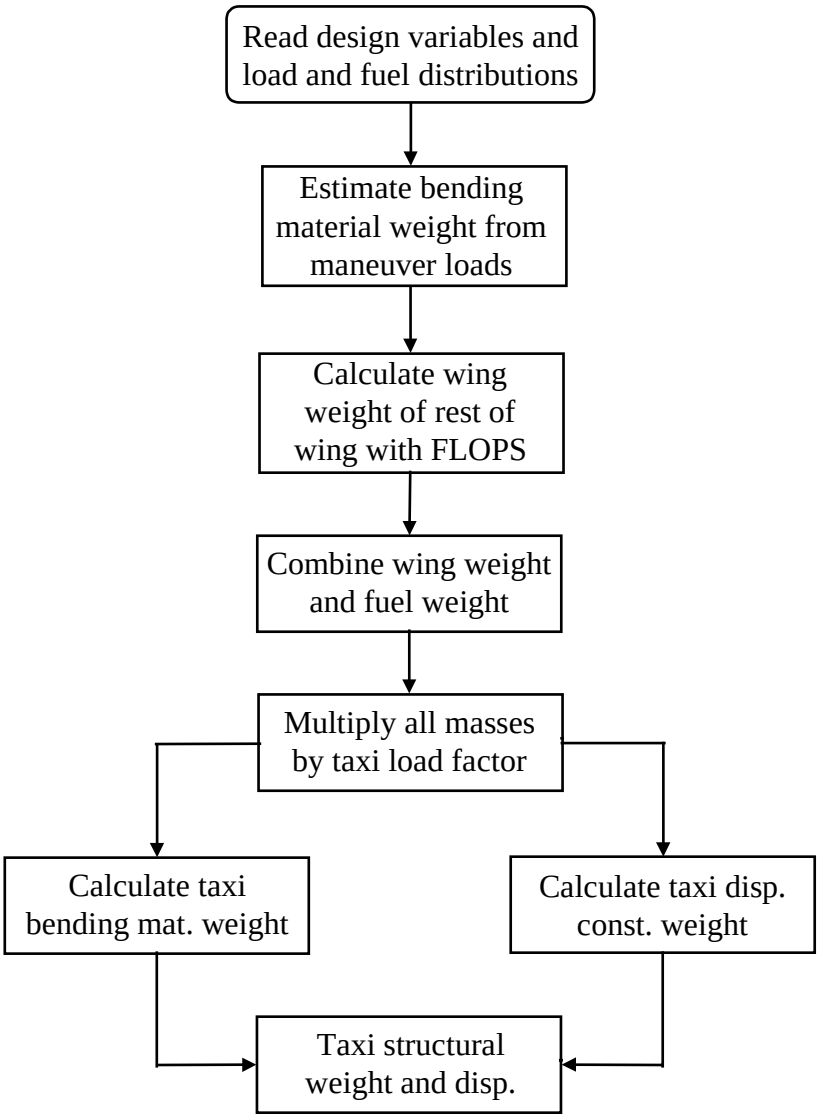

Figure 3.7 Taxi weight analysis.

3.2.1 Optimum Thickness Distribution for Wing Ground Strike Displacement Constraint

Since the wing is treated as a cantilever beam with a given strut load, the required thickness at a point *y* for any load case can be directly calculated from the maximum bending moment $M_{max}(y)$ of any load case at that point. The imposition of a displacement limit on the wing tip does not change that thickness requirement. Moreover, it becomes a lower limit for the thickness at that point, which will be denoted as $t_m(y)$. The displacement limit at the tip δ_{tip} may require additional thickness

at some points. Now the question is how to distribute the thickness optimally? Denoting the chord of the structural box as $c_b(y)$ and the thickness of the box as $d(y)$, the objective of the optimization is the material volume V which can be expressed as:

$$V = 2\int_0^{b/2} t(y)c_b(y)dy, \tag{3.28}$$

where $b/2$ denotes the wing box half-span.

The displacement at the tip can be calculated in terms of the bending moment in taxi bump bending moment distribution $M_b(y)$ as:

$$\delta_{tip} = \int_0^{b/2} \frac{M_b(y)y}{EI(y)}dy, \tag{3.29}$$

where E is Young's modulus, and $I(y)$ is the moment of inertia of the wing box given in Equation (3.19).

The optimization problem can then be formulated:

$$\begin{aligned} &\text{Minimize} \quad \int_0^{b/2} t(y)c_b(y)dy, \\ &\text{such that} \quad \int_0^{b/2} \frac{2M_b(y)y}{Ec_b(y)t(y)d^2(y)}dy = \delta_{tip}, \\ &\text{and} \quad t(y) \geq t_m(y). \end{aligned} \tag{3.30}$$

Now, the above problem can be combined into a single objective functional I by introducing a scalar Lagrange multiplier λ_1 and a Lagrange multiplier function $\lambda_2(x)$

$$\begin{aligned} I = &\int_0^{b/2} t(y)c(y)dy + \lambda_1\left(\int_0^{b/2} \frac{2M_b(y)y}{Ec_b(y)t(y)d^2(y)}dy - \delta_{tip}\right) + \\ &\int_0^{b/2} \lambda_2(x)\left[t(y) - t_m(y)\right]dy. \end{aligned} \tag{3.31}$$

Taking the first variation of I

$$\delta I = \int_0^{b/2} \left[c_b(y) - \frac{2M_b(y) y \lambda_1}{E c_b(y) t^2(y) d^2(y)} + \lambda_2(y) \right] \delta t(y) dy = 0 . \qquad (3.32)$$

Since $\lambda_2(y) = 0$ when the minimum thickness constraint is not active, then:

$$t^2(y) = \frac{2M_b(y) y \lambda_1}{E c_b^2(y) d^2(y)} , \qquad (3.33)$$

whenever it gives a value larger than t_m (Haftka and Gurdal, 1992) .

To find λ_1, the material thickness at the root, i.e. $t(b/2)$, can be assumed as a design variable in global optimization. Then, λ_1 can be extracted from Equation (3.33) for $y = b/2$:

$$\lambda_1 = \frac{E t^2(b/2) c_b^2(b/2) d^2(b/2)}{2M_b(b/2) b/2} . \qquad (3.34)$$

A value for $t(b/2)$ is picked by the global optimizer. If the optimizer selects λ_1 too large, the weight will increase, and if it selects λ_1 too small, the displacement constraint will be violated.

In general, for the regions where the stress constraints are active, the thickness is dictated by the stress constraints denoted by $t_m(y)$, and for the regions where the displacement constraints are active the thickness to dictated by the displacement constraints.

3.3 *Landing Analysis*

Landing loads could be critical because of the downward inertia loads as well as the large concentrated loads applied to the wing due to the landing gear impact if the landing gears are located on the wing. For the case of the strut-braced wing, the landing gear is not located on the wing thus the landing gear loads do not directly apply to the wing. This matter can be considered as a plus. Fuselage-mounted landing gears are utilized for truss-braced wing configurations.

Inertia loads during landing can be found by multiplying the aircraft inertia factor by the weights. The landing gear impact load factor can be obtained from the following energy based equation (Niu, 1988):

$$n_{LG} = \frac{\frac{V_S^2}{2g} - \frac{\eta_t K_t X_t^2}{2W} + \left(1 - \frac{L}{W}\right)\left(X_t + X_S\right)}{\eta_s X_S}, \tag{3.35}$$

where W denotes the takeoff gross weight, V_S denotes the sinking speed, K_t denotes the tire spring constant, η_t denotes a factor to account for the fact that the tire deflection is non-linear, X_t denotes the tire deflection, L denotes the wing lift, X_S denotes the strut stroke, and η_s denotes the strut efficiency (0.8 to 0.85). The sinking speed for large transports is usually assumed 10 *ft/sec* and $L = W$.

The inertia factor on the aircraft is defined as:

$$n_L = n_{LG} + \left(\frac{L}{W}\right), \tag{3.36}$$

where *L/W* is the aircraft load factor during landing.

Figure 3.8 shows the landing loads on the strut-braced wing aircraft for a two point level landing condition. Depending on the aircraft and landing gear characteristics, the landing gear load factor is estimated $1.2 < n_{LG} < 1.7$. Hence, assuming that $L=W$ during landing the aircraft inertia factor is obtained $2.2 < n_L < 2.7$. For the analysis herein, a landing load factor of 2.5 will be considered.

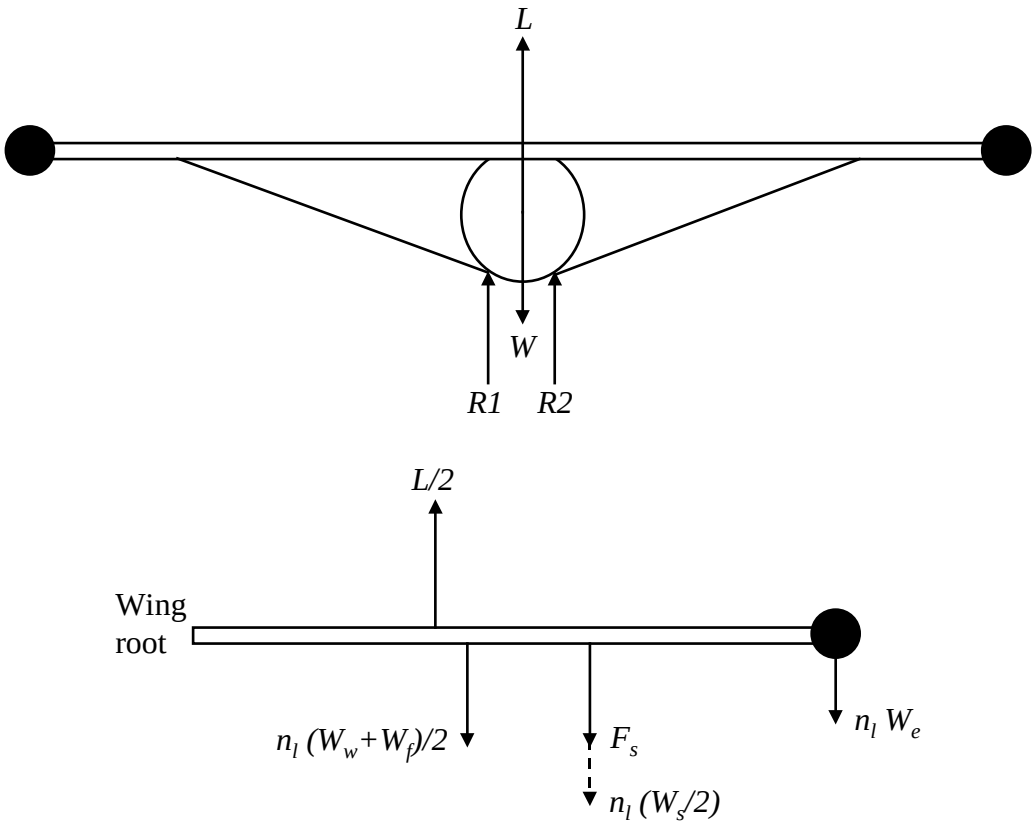

Figure 3.8 Landing loads.

For the above sketches W_e is the engine weight, W_s is the strut weight, F_{sv} is the vertical strut force, W_L is the aircraft landing weight, and W_w is the wing weight.

3.4 *Bending Material Weight Optimization*

3.4.1 Wing Bending Material Weight Calculation

Optimum weight is the key issue in designing an aircraft. A wing with a high aspect ratio and small thickness to chord ratios has aerodynamic advantages compared to a conventional cantilever wing aircraft. However, wings of that kind may encounter a large weight penalty due to the increased material thickness to meet the yield criterion. Thus, to reduce weight, using a strut or a truss to support the wing can be a suitable solution since a strut or a truss can relieve the wing bending moment. As long as the strut bears part of the loading, some of the wing bending moment distribution diminishes and hence the required material weight decreases. Knowing the bending moment distribution, the corresponding bending stress in the wing is calculated from the following equation:

$$\sigma_{\max} = \frac{M(y)d(y)}{2I(y)}, \tag{3.38}$$

where $\sigma_{\max}$ denotes the maximum stress and $M(y)$ denotes the bending moment of the wing.

If the wing is designed according to the fully-stressed criterion, one can substitute the allowable stress into equation (3.38) for $\sigma_{\max}$. Furthermore, substituting equation (3.19) into equation (3.38) for $I(y)$, the wing skin thickness can be specified as:

$$t(y) = \frac{|M(y)|}{c_b(y)d(y)\sigma_{all}}, \tag{3.39}$$

where σ_{all} indicates the allowable stress.

The bending material weight of the half-wing is expressed as:

$$W_b = 2\int_0^{b_s/2} t(y)c_b(y)\rho dy\,, \tag{3.40}$$

where b_s is the structural span. The structural span is obtained as:

$$b_s = \frac{b}{\cos\Lambda}, \tag{3.41}$$

where Λ is the three quarter chord wing sweep angle (McCullers).

Then, assuming *d(y)* to be constant and substituting for *t(y)* into equation (3.40), the bending material weight is formulated:

$$W_{wb} = k\int_0^{b_s/2} \left|M(y)\right| dy\,, \tag{3.42}$$

where $k = 2\rho/d\sigma_{all}$.

The non-dimensional form can be written:

$$\overline{W}_{wb} = \frac{W_{wb}}{kq_0\left(\frac{b_s}{2}\right)^3}, \tag{3.43}$$

where $\overline{W}_{wb}$ denotes the non-dimensional bending material weight. This equation reveals the importance of the span in wing bending material weight.

Eventually, the non-dimensional bending material weight is obtained as:

$$\overline{W}_{wb} = \int_0^1 \left|\overline{M}(\overline{y})\right| d\overline{y}\,. \tag{3.44}$$

Equation (3.44) shows that the bending material weight is dependent directly on the area under the bending moment diagram. Thus, to minimize the bending material weight, the area under the bending moment diagram should be minimized.

If *d* varies along the wing in terms of *y*, the bending material weight will have the form:

$$\overline{W}_{wb} = \int_0^1 \frac{\left|\overline{M}(\bar{y})\right|}{\overline{d}(\bar{y})} d\bar{y}\,, \tag{3.45}$$

where *d(y)* is obtained from equations (3.22) and (3.23), $k = 2\rho/\sigma_{all}$, and $\overline{W}_{wb} = W_{wb} / kq_0(b_s/2)^2$. Therefore, to have the bending material weight minimized, the area under the integrand function in equation (3.45) should be minimized. This functional as well as the strut weight is utilized as the objective function to minimize the bending material weight of the wing.

3.4.2 Strut Weight Calculation

For all calculations the strut is considered as a truss member which is modeled as a spring in the *z*-direction for simplicity. As shown before, the spring stiffness is obtained from the stiffness matrix of a truss member. The effect of strut bending will be considered in wing weight estimation by a simple assumption and will be discussed later. The actual strut force can be calculated from its vertical component as:

$$F_s = \frac{F_{sv}}{h}\sqrt{h^2 + \left(\frac{s}{\cos\Lambda_s}\right)^2}\,, \tag{3.46}$$

where F_s is the actual strut force and Λ_s is the strut sweep angle. The required cross-sectional area of the strut, i.e. A_s, is given as $A_s = F_s/\sigma_{all}$. So that, the weight of the strut capable of carrying tension loads is:

$$W_{st} = A_s \rho_s \sqrt{h^2 + \left(\frac{s}{\cos \Lambda_s}\right)^2}, \tag{3.47}$$

where ρ_s is the material density of the strut.

Substituting for A_s and F_s, we have:

$$W_{st} = \frac{\rho_s}{\sigma_{all} h}\left[h^2 + \left(\frac{s}{\cos \Lambda_s}\right)^2\right] F_{sv}. \tag{3.48}$$

Since a real strut also carries bending loads, a factor of 1.5 was found reasonable to be multiplied to the strut tension weight to account for the additional strut bending weight. Consequently, the strut bending and tension weight will be:

$$W_s = 1.5 W_{st}. \tag{3.49}$$

Also, to take into account the extra compression weight due to the horizontal strut force component in inboard wing, another additional weight equal to the strut tension weight W_{st} is added to the total bending material weight. Thus, a factor of 2.5 is multiplied by the strut tension weight to account for both strut bending weight and inboard compression weight. The total wing structure bending material weight is expressed as:

$$W_b = 2(W_{wb} + 2.5 W_{st}). \tag{3.50}$$

3.4.3 Wing Weight Estimation Scheme

The wing weight estimation scheme is shown in Figure 3.9. The design variables and aerodynamic load and fuel distributions are imported from other parts the MDO code. Then, the wing bending material weight, strut weight, and offset weight are calculated from two maneuver load conditions 2.5g and -1.0g × factor of safety of 1.5 and a 2.0g taxi bump load condition. Moreover, the total wing structure bending material weight is exported to FLOPS and the resulting total wing weight obtained from FLOPS is exported to the MDO code.

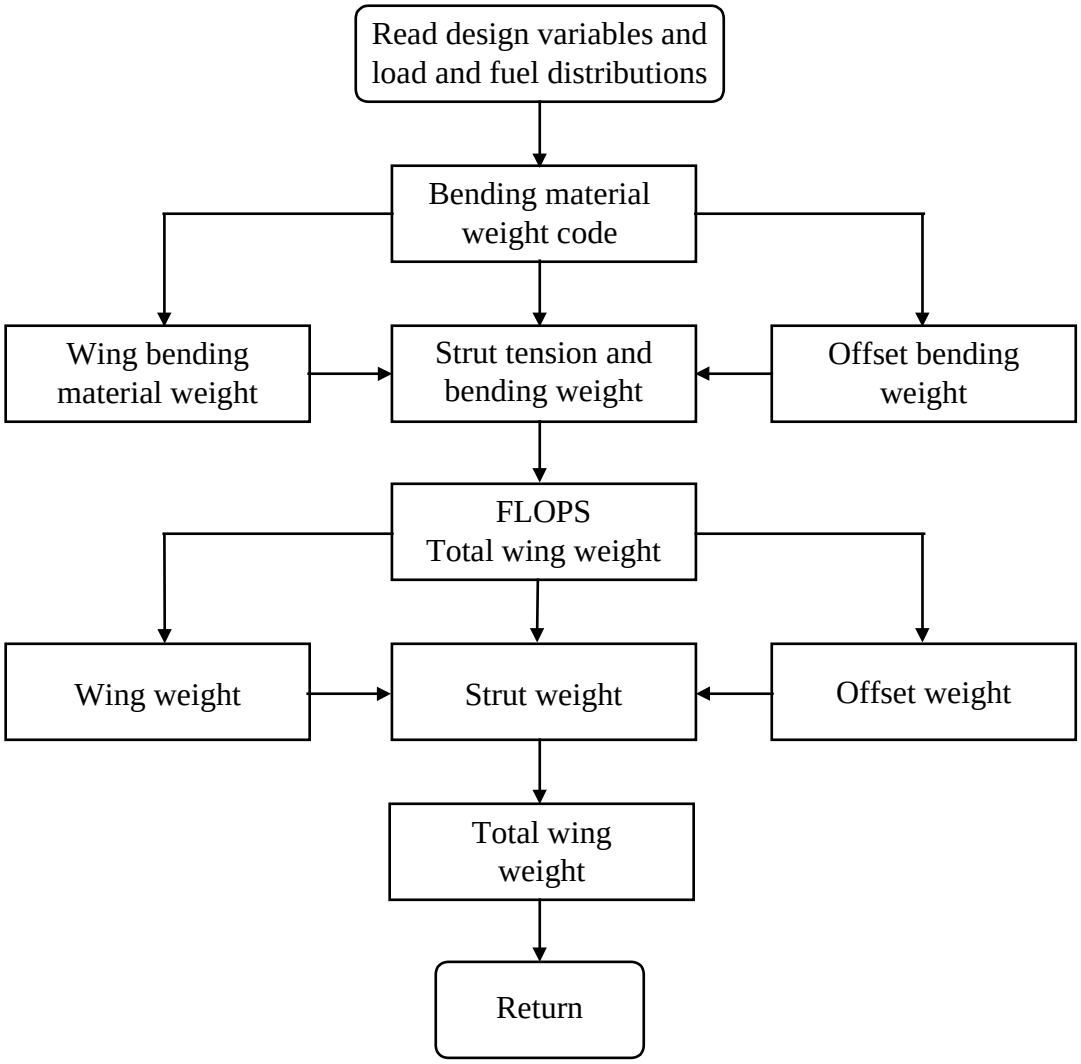

Figure 3.9 Wing weight estimation scheme.

The above procedure has been coded and implemented in the MDO code for bending material weight estimation.

3.5 *Validation*

The structural analysis code has been validated to ensure the integrity of the results. The bending material weight computed from the piecewise linear load model is compared with the bending material weights given by Torenbeek (1992) and FLOPS (McCullers) for the Boeing 747-100. Figure 3.10 presents the comparison. It shows good agreement. The values found using the procedure described here is given in the column labeled *wing.f*, which is the name of the subroutine. The bending material weight calculated by *wing.f* (see Appendix B) shows a 0.6% deviation from the actual 747 bending material weight.

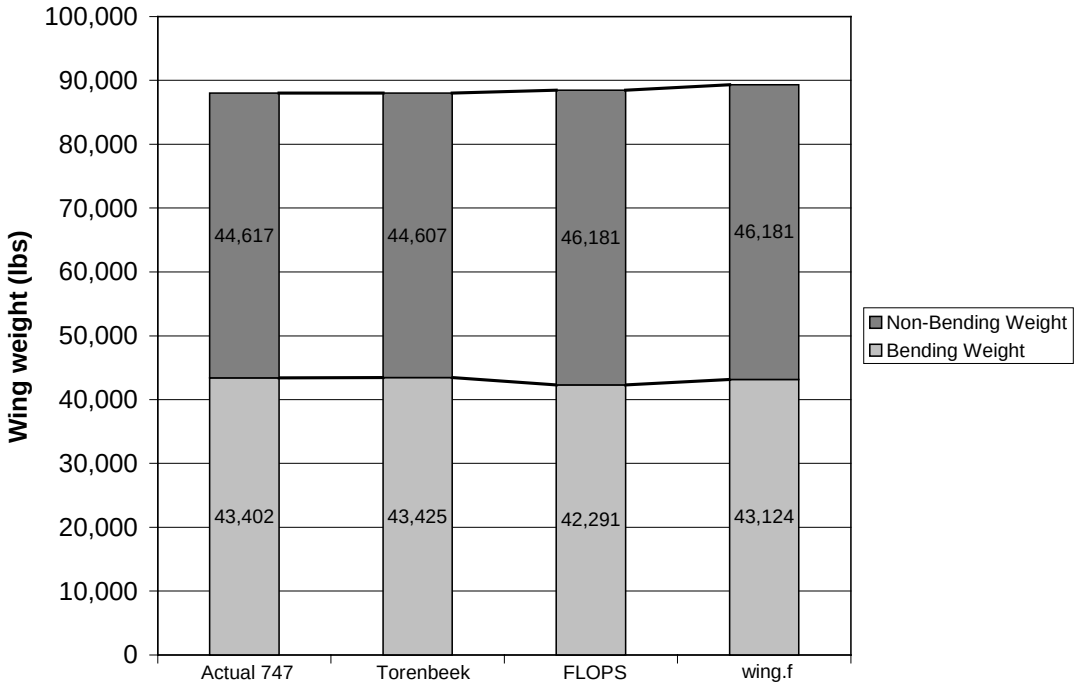

Figure 3.10 Wing weight validation.

Chapter 4 Optimization Problem

Multidisciplinary Design Optimization has been employed to optimize truss-braced wing configurations to minimize the takeoff gross weight subject to realistic constraints. The method of feasible directions in the Design Optimization Tools (DOT) software package from Vanderplaats (1995) is used to perform optimizations. A brief description of the optimization problem is presented herein. For more details refer to Grasmeyer et al. (1998).

4.1 *Design Variables and Constraints*

In general, a single-strut-braced wing is parameterized by a total of 22 design variables summarized in Table 4.1. Fourteen design variables describe the wing layout and 8 design variables describe the other distinctive features. The vertical separation of the wing and strut at the root is designated to be equal to the fuselage diameter. The fuselage geometry of the baseline cantilever design is used in the strut-braced wing configurations and remains fixed. Moreover, tail sizing is also performed. Table 4.2 shows thirteen inequality constraints to obtain realistic configurations. Additionally, side constraints are also used to bound each design variable. Table 4.3 lists the two major side constraints, i.e. the upper limit of the semispan which ensures that the wing span is within the FAA 80 meter gate box limit and the lower limits of the wing and strut *t/c*'s which guarantee values more than 5% and 8%, respectively. The 5% limit was chosen empirically and the 8% limit was suggested by LMAS to reduce strut sagging due to its weight during taxiing.

Table 4.1 Strut-braced wing configuration variables

Number	Description
1	Semispan
2	Wing-strut spanwise location
3	Wing sweep
4	Strut sweep
5	Wing root chord
6	Wing chord at wing-strut intersection
7	Wing tip chord
8	Wing root *t/c*
9	Wing-strut intersection *t/c*
10	Wing tip *t/c*
11	Strut root chord
12	Strut tip chord
13	Strut *t/c*
14	Strut offset distance
15	Strut force
16	Vertical tail lift coefficient increment due to circulation control
17	Zero-fuel weight
18	Fuel weight
19	Spanwise location of engine
20	Average cruise altitude
21	Maximum sea level static thrust
22	Vertical tail sizing factor

Some of the constraint limits are based on FAA regulations and some are adopted from in-service aircraft like the Boeing 777. The maximum wing ground strike constraint of 20 *ft* was taken based on the fuselage diameter and landing gear length. Also, a slack load factor between 0 and 0.8 ensures that the strut will be neither pre-loaded when the slack load factor is less than zero nor subject to fatigue loads due to engagement and disengagement of the strut at cruise when the slack load factor is about 1.

Table 4.2 Optimization constraints

Number	Description
1	Zero-fuel weight convergence
2	Range $\geq$ 7,500 *nmi* with 500 *nmi* reserve
3	Balanced field length $\leq$ 11,000 *ft*
4	2^{nd} segment climb gradient $\geq$ 2.4%
5	Approach speed $\leq$ 140 *kts*
6	Missed approach climb gradient $\geq$ 2.1%
7	Fuel volume ratio $\geq$ 1.0 (fuel in wing only)
8	Rate of Climb at initial cruise altitude $\geq$ 500 *ft/min*
9	Engine-out (C_n constraint)
10	Wing ground strike at the taxi bump load condition $\leq$ 20 *ft*
11	Max. allowable section lift coefficient at the beginning of cruise $\leq$ 0.7
12	Landing distance $\leq$ 11,000 *ft*
13	0 $\leq$ Slack load factor $\leq$ 0.8

Table 4.3 Side constraints

Number	Description
1	80 meter gate box on the wing span
2	Minimum allowable *t/c* of 5% on the wing and 8% on the strut

The weight equations from NASA Langley's Flight Optimization System (FLOPS) (McCullers) are used to calculate most of the structural weight (except the wing bending material weight) and all the non-structural weight of the aircraft. However, FLOPS would be expected to yield inaccurate results for the wing bending material weight since truss-braced wing configurations are unconventional. Consequently, a code has been developed to estimate the wing bending material weight. The method to estimate the wing bending material weight uses a piecewise linear load model and is based on the fully stressed criterion. The wing geometry parameters and load distributions are passed from the MDO code at the critical load conditions to the wing bending weight code for structural optimization and wing bending material weight estimation. Then, the bending material weight value is replaced for the value in FLOPS to estimate the wing weight more accurately. In the future, for more complex truss configurations, response surface equations will be used. These response surfaces will be developed using a finite element method based structural optimization for the

wing bending material weight. This was previously done by Balabanov et al. (1996) and Kaufman et al. (1996) for the High Speed Civil Transport (HSCT) wing.

4.2 *MDO Code Connectivity*

Figure 4.1 shows the connectivity of aerodynamics, structures, propulsion, and controls in the MDO approach for the truss-braced wing problem. The structural optimization has been highlighted in the flowchart.

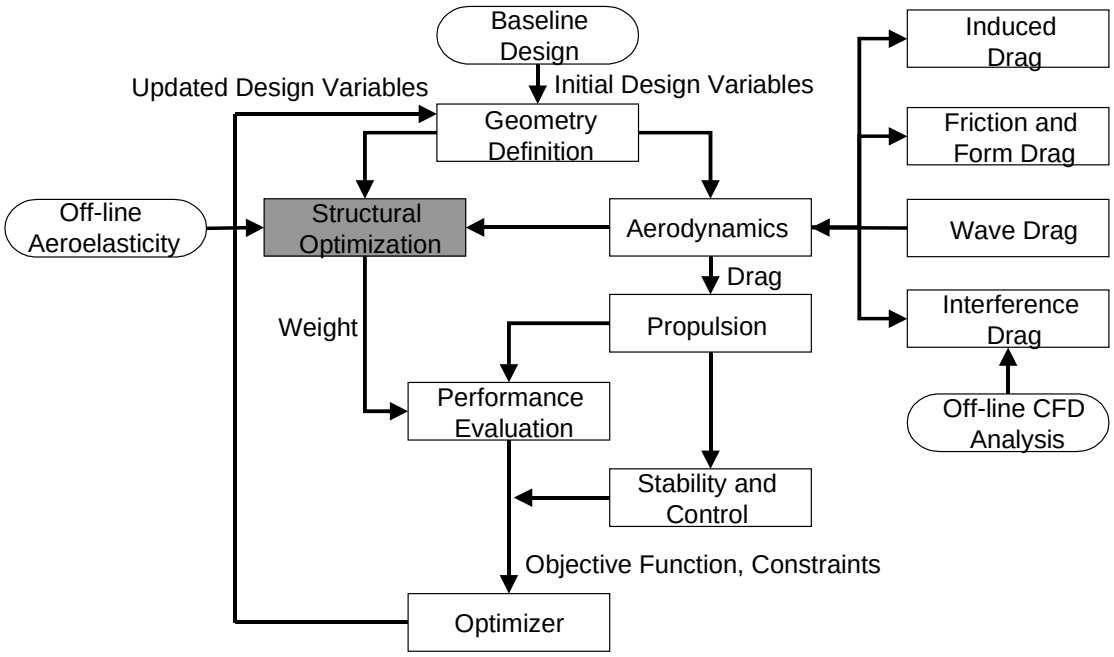

Figure 4.1 MDO code connectivity.

First a reasonable baseline design with initial design variables is created to define the aircraft. Then, the design variables are passed to the aerodynamics and structural optimization modules for aerodynamic loads and wing weight estimation, respectively. Meanwhile, the aerodynamics module provides the lift loads at the critical maneuvers for the structural optimization module for wing weight calculation. The aerodynamic module consists of several sub-modules. The sub-modules estimate the total lift loads and drag. The total drag contains the induced drag, friction and form drag, wave drag, and interference drag. The wing-strut interference drag is

evaluated using an offline CFD solver. Moreover, the propulsion module reads the drag from the aerodynamics module and calculates the required thrust and engine size by rubber engine sizing. Tail sizing and circulation control for the engine-out condition are performed in the stability and control module. Finally, the total drag and wing weight are input to the performance evaluation module to calculate the aircraft takeoff weight, the objective function for the optimizer. The constraints are also evaluated in the same module. This procedure is iterated by the optimizer until an optimum configuration is obtained.

A Lockheed Martin Aeronautical Systems' (LMAS) mission profile is used to generate the results. The takeoff gross weight was chosen as the objective function for optimization. Nineteen out of 22 design variables for the tip-mounted engine design and 20 out of 22 design variables for the under-wing engine design as well as 13 constraints are used to characterize the strut-braced wing configurations and bending material weight estimation. For the current optimization cases, the strut *t/c* is fixed at 8% and the strut tip chord is set to be equal to the strut root chord based on the LMAS suggestion.

Chapter 5 Results

All structural results obtained from the piecewise linear load method for different strut-braced wing design configurations are tabulated and presented in this chapter. Two sets of single-strut configurations are explored. The first set represents the optimization results based on the tip-mounted engine configuration and the second set indicates the optimization results based on the under-wing engine configuration. The wing structure is partially assumed to be made of a composite material.

Also, the final design configurations are compared with the counterpart cantilever wing configuration obtained from the same MDO methodology and technology to evaluate the potential of the strut-braced wing. Some of the technology concepts that are introduced are natural laminar flow, drag reduction techniques, and relaxed static stability (Grasmeyer et al., 1998). Rubber engine sizing to match the engine size and weight to the required thrust is also considered.

The advantage of using composite materials for bending load carrying panels is evaluated by comparing the wing weights of metallic strut-braced wing configurations to those of composite strut-braced wing configurations.

Finally, the variations of the wing weight and takeoff gross weight of the strut-braced wing to changes in the strut force, strut offset length, and wing-strut intersection are shown.

5.1 *Material propeties*

Two different materials are used in the wing weight estimation code to produce the results. A high strength aluminum alloy and a graphite-epoxy composite laminate with a [45/-45/0/90/0/-45/45] stacking sequence are considered. Material information and properties were obtained from Torenbeek (1992) and Fielding et al., (1987) for

the aluminum alloy and Vitali et al., (1998) for the graphite-epoxy and are given in Table 5.1 and Table 5.2, respectively. Since at this stage a detailed structural analysis is not being performed, average values for the graphite-epoxy composite laminate, i.e. Young's modulus and the yield stress, are used for weight estimation. These values are substituted for the aluminum properties in the wing weight code.

Table 5.1 Material Properties of an aluminum alloy

Aluminum	Wing	Strut
Density (lb/in^3)	0.103177	0.103177
Young's Modulus (lb/in^2)	1.0442361×10^7	1.0442361×10^7
Allowable Stress (lb/in^2)	55632.0	55632.0

Table 5.2 Material properties of graphite-epoxy [45/-45/0/90/0/-45/45]

Graphite epoxy	Wing	Strut
Density (lb/in^3)	0.058	0.058
Young's Modulus (lb/in^2)	9.25×10^6	9.25×10^6
Yield Stress (lb/in^2)	50000.0	50000.0

Also, a composite material factor f_{comp} has been implemented into FLOPS wing weight equations to account for composite wings (see Appendix A). This factor can also be employed to predict the influence of a composite material in wing weight estimation. This factor can vary between 0 for no composite and 1 for 40% composite. For the future aircraft technology (2010 technology), a factor of $f_{comp} = 0.5$ was found suitable for the current analysis according to the LMAS suggestion. This factor will have a 20% reduction in the bending material weight, an 8% reduction in shear and flaps weight, and a 15% reduction in non-structural weight.

5.2 *Critical Load Conditions*

Three critical load conditions are considered to accomplish the results according to load factors per FAR 25.337 (b) and (c) for commercial transport aircraft (Lomax, 1996):

1. Maximum lift of $2.5\,MTOW\,FS/2$ *lbs* distributed over the wing half-span. It corresponds to a 2.5g upward maneuver.
2. Reversed lift of $-\,MTOW\,FS/2$ *lbs* distributed over the wing half span. It corresponds to a 1.0g downward maneuver.
3. 2.0g taxi bump.

The bending material weight calculations are based on the above load conditions.

5.2.1 Landing Calculations

An inertia load factor of 2.5 is assumed for landing calculations. The following landing loads are calculated from the output data which will be presented later in this chapter for the tip-mounted engine configuration. Based on the material discussed in chapter 3, section 3.3 one obtains:

$$L/2 = W_L/2 = 244{,}913.0\,(lbs),$$
$$n_L W_e + n_L(W_s + W_w + W_f)/2 = 300{,}775.0\,(lbs),$$

where W_e is the engine weight, W_s is the strut weight, W_f is the fuel weight, W_L is the aircraft landing weight, and W_w is the wing weight.

Comparing the downward loads with the upward lift shows that the resultant of the downward loads is a little greater than the lift during landing. Because the wing is designed for 2.5 and –1.0 maneuver load factors and 2.0 taxi bump load factor, the bending moment distribution due the landing loads is not expected to be more critical than those of the critical load conditions according to the above results. Consequently, it can be concluded that landing would be less critical and was not considered as a critical load case in this study. Similar conclusion can be carried out for the under-wing engine configuration.

5.3 *Strut-Braced Wing Optimum Configurations*

The advanced technology optimum cantilever wing configuration and the advanced technology optimum strut-braced wing configuration results are summarized in Table 5.3. These design configurations were created using the strut-braced wing MDO tool. The strut-braced wing with tip-mounted engines exhibits a 9.2% reduction in the takeoff gross weight, a 38.1% reduction in the wing weight, and an 8.2% reduction in the fuel weight while the strut-braced wing with under-wing mounted engines shows a 9.4% reduction in the takeoff gross weight, an 18.2% reduction in the wing weight, and a 15.2% reduction in the fuel weight compared to the cantilever configuration. Although both strut-braced wing configurations have practically equal takeoff gross weights, the under-wing configuration shows more reduction in the fuel weight which makes it a more economical aircraft. This corresponds to a higher *L/D* for the under-wing engine configuration. Moreover, notice that the wing weight of the under-wing engine configuration is higher than the wing weight of the tip-mounted engine configuration with practically equal takeoff gross weights, indicates that the tip-mounted engine configuration is a structurally dominated design and the under-wing engine configuration is an aerodynamically dominated design. The span and *t/c*'s of the tip-mounted engine configuration are decreased and increased respectively to decrease the wing weight while the span and *t/c*'s of the under-wing engine configuration are increased and decreased respectively to increase the aircraft *L/D* by taking advantage of induced and wave drag reductions.

Table 5.3 Cantilever and strut-braced wing optimum configurations

	Advanced cantilever wing	Strut-braced wing tip-mounted engines	Strut-braced wing under-wing engines
Wing half span (*ft*)	109.21	93.30	114.34
Wing-strut intersection (*ft*)	N/A	83.97 (90%)	79.12 (69%)
Wing break location (*ft*)	40.41	83.97 (90%)	79.12 (69%)
Wing 1/4 chord sweep (*deg*)	28.29	31.96	30.39
Strut 1/4 chord sweep (*deg*)	N/A	21.10	20.86
Strut offset length (*ft*)	N/A	3.34	2.51
Wing root chord (*ft*)	36.77	29.41	27.58
Wing break chord (*ft*)	25.83	12.46	13.71
Wing tip chord (*ft*)	7.35	10.58	7.52
Strut root chord (*ft*)	N/A	6.616	6.616
Strut tip chord (*ft*)	N/A	6.616	6.616
Wing root *t/c*	0.1110	0.1507	0.1308
Wing break *t/c*	0.1000	0.0654	0.0648
Wing tip *t/c*	0.0800	0.0510	0.0500
Strut *t/c*	N/A	0.0800	0.0800
Aspect ratio	9.9	9.3	13.0
Wing area (ft^2)	4,809	3,731	4,013
Strut force (*lbs*)	N/A	58,319	227,152
Slack load factor	N/A	0.8	0.8
Cruise *L/D*	23.41	23.04	25.66
Engine weight (*lbs*)	13,913	12,769	11,160
Spanwise engine location (*ft*)	40.41 (37%)	93.30 (100%)	43.83 (38%)
Zero fuel weight (*lbs*)	354,356	319,640	331,847
Fuel weight (*lbs*)	186,332	171,049	157,977
Wing weight (*lbs*)	73,767	45,631	60,323
Takeoff gross weight (*lbs*)	540,689	490,687	489,826

The tip-mounted engine design shows a longer strut offset length than that of the under-wing engine design. This behavior originates from the wing-strut interference drag reduction. Since the wing-strut intersection distance is greater for the tip-mounted engine design, the optimizer tries to increase the strut offset distance to decrease the interference drag. Therefore, the wing-strut intersection is driven outboard to increase the strut force moment arm to reduce the strut optimum force. The reduction in the strut optimum force will result in a lighter strut offset. However, since the under-wing engine design has a longer wing span, the wing-strut intersection

lies at about 2/3 of the half span of the wing to prevent high strut and strut offset weight due to the induced moment by the horizontal strut force component. Thus, the strut offset length can be shorter without too much interference drag penalty.

The slack load factor for both cases is calculated to be 0.8 which is the specified upper bound in the slack load factor constraint. This means that the strut engages at 0.8g. Hence, at the cruise condition the strut is active.

Also, several local optima, deviating between 0.6-3.5% from the obtained optima, were found by changing the design variables initial guesses. Thus, the current configurations are not guaranteed to be the global optimum designs. However, the author did his best to discover the best design configurations based on minimum takeoff gross weight. This was achieved by assigning the design variables initial values close to the optimum values obtained from the previous run and then re-optimizing.

5.4 *Aerodynamic and Taxi bump Loads*

Aerodynamic loads are imported into the structural optimization subroutine from the aerodynamics subroutine (Grasmeyer et al. 1997). Figure 5.1 shows the lift distributions at the 2.5g and 1.0g load conditions. A linear interpolation procedure is used to interpolate the load distributions from the locations where the aerodynamic loads are assumed onto the structural nodes. The structural nodes are assumed to be independent of the aerodynamic nodes. A convergence study was performed to determine a reasonable value for the number of structural nodes. The number of 82 nodes was found suitable. Also, the 2.0g taxi bump loads are obtained from the procedure described in Section 3.2 and are shown in Figure 5.2. For these plots, the *x*-axis represents the aerodynamic half-span in *ft* and the *y*-axis represents the amount of load in *lbs/ft*.

(a)

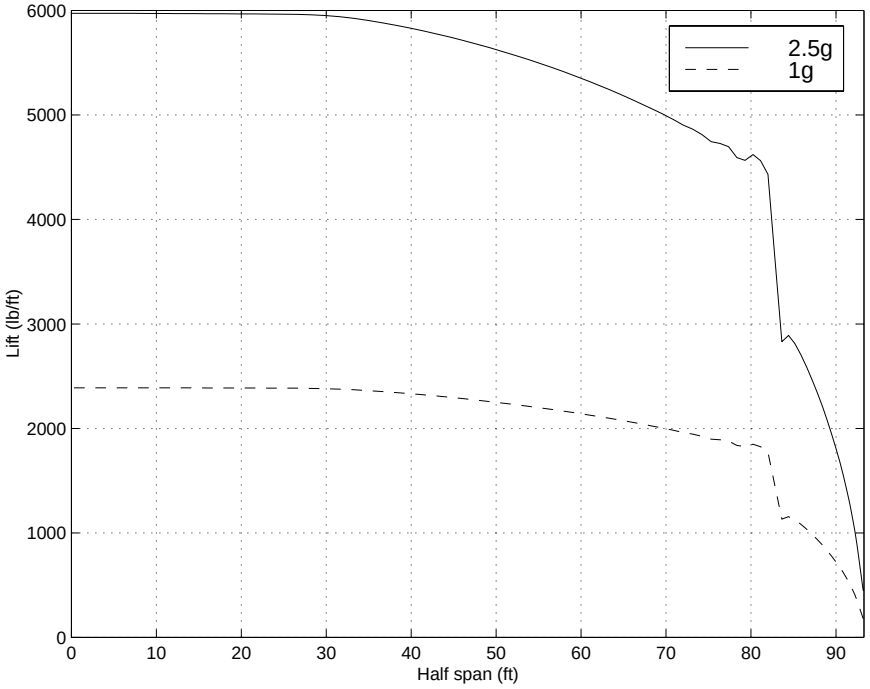

(b)

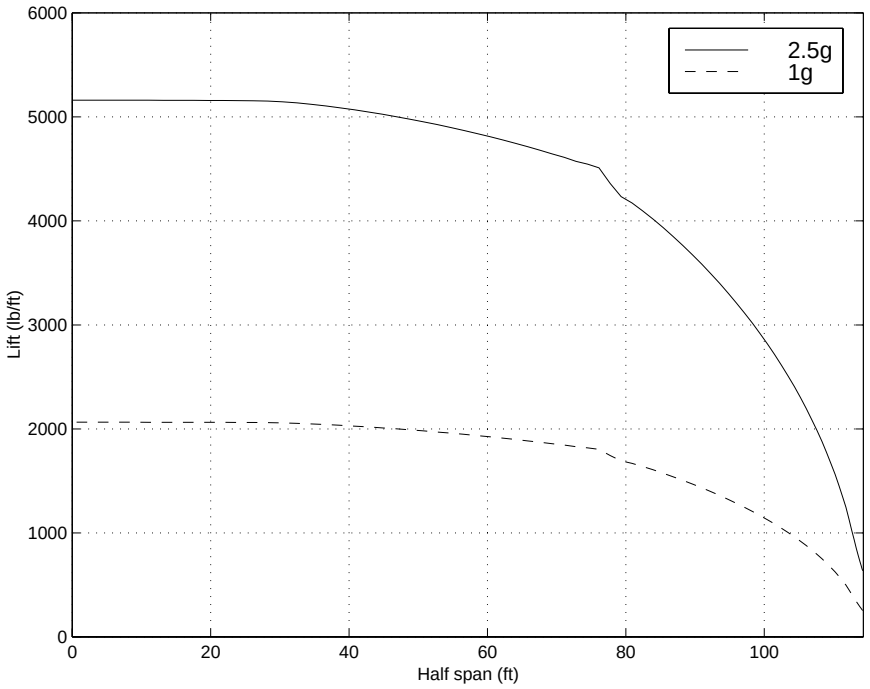

Figure 5.1 Aerodynamic load distributions at the 2.5g and 1.0g load conditions (a) tip-mounted engines (b) under-wing engines.

(a)

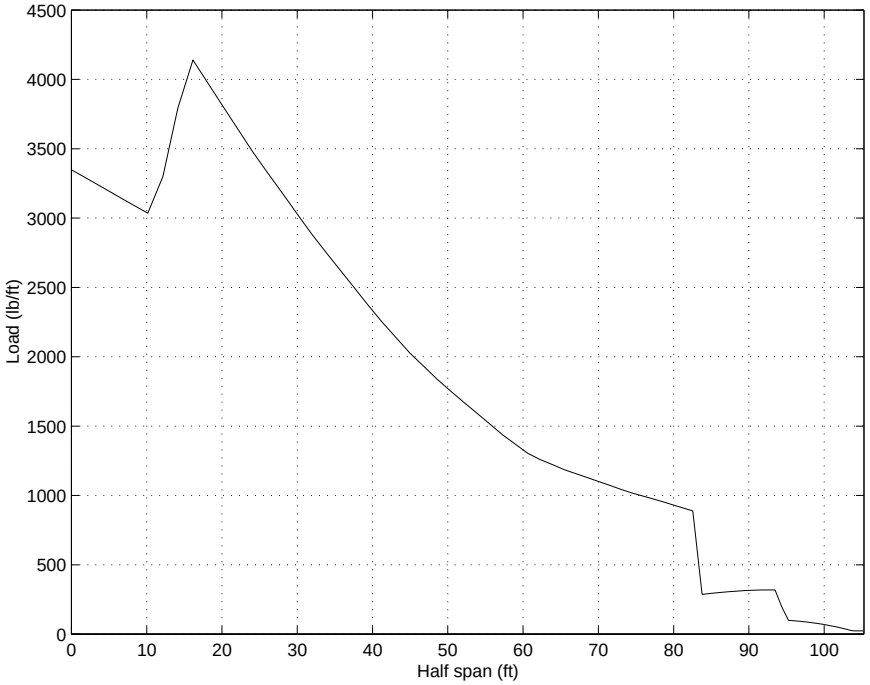

(b)

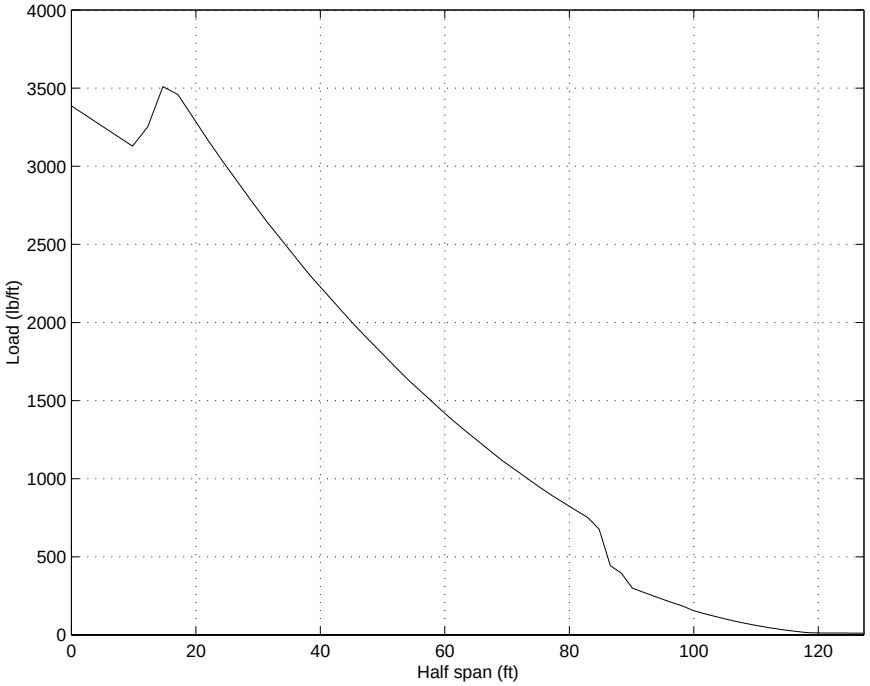

Figure 5.2 2.0g taxi bump loads (a) tip-mounted engines (b) under-wing engines.

5.5 *Shear Force and Bending Moment Diagrams*

Figure 5.3 and Figure 5.4 show the shear force and bending moment distributions at the critical load conditions corresponding to both configurations, respectively. The distributions are obtained at the 2.5g and –1.0g maneuver conditions and the 2.0g taxi bump load condition. For both maneuver conditions, a factor of safety of 1.5 is considered. Thus, the results essentially are obtained based on 3.75g and –1.5g load factors. At each structural segment the shear force and bending moment are calculated from mechanics of materials equations and then the thickness distribution for each load condition is calculated according to the derived equations in the previous chapter. For these plots the *x*-axis represents the structural half-span of the wing in *ft* and the *y*-axis represents the shear force in *lbs* and bending moment in *lb-ft*.

The shear force diagram corresponding to the tip-mounted engines shows a discontinuity on the 2.5g maneuver shear force distribution. This is due to the vertical strut force component. Moreover, because the engines are located on the wing tips, the shear forces at the wingtip do not go to zero and are equal to the engine weight multiplied by the load factor. Also, for the under-wing engines, the discontinuity on the 2.5g shear force distribution around 50 *ft* from the root corresponds to the engine weight and the one around 85 *ft* from the root corresponds to the vertical strut force component. At this load condition, the discontinuity is more pronounced since the vertical strut force component is greater. The other discontinuities on the -1.0g and 2.0g shear force distributions are due to the engine weight. As it is seen, all the shear force distributions for this case go to zero at the wingtip.

Furthermore, the discontinuities on the bending moment distributions are due to the horizontal strut force distribution applied to the strut offset. This force creates a moment in the opposite direction of the bending moment due to the positive lift. Thus, some relief can be achieved.

(a)

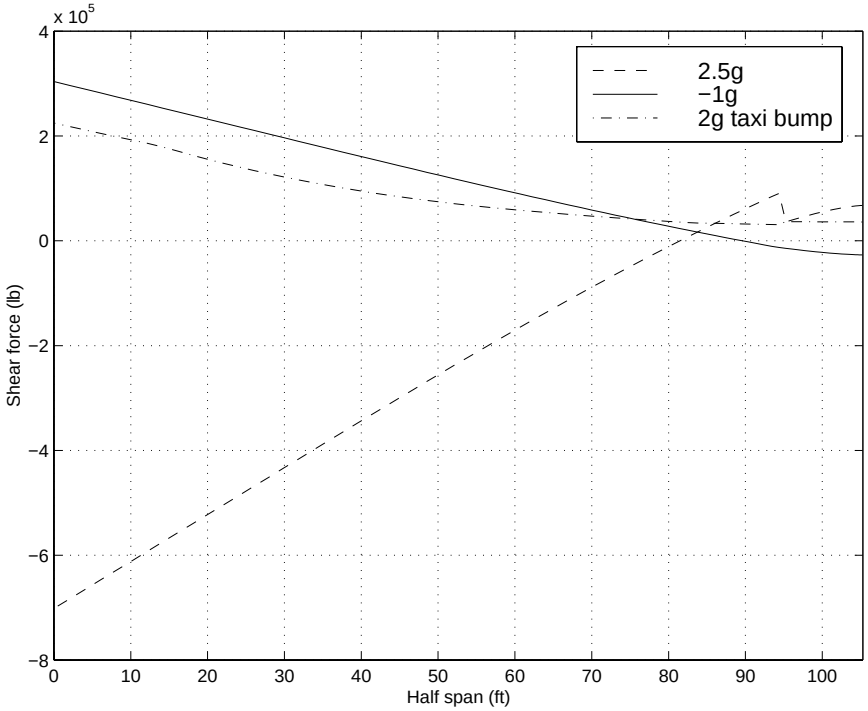

(b)

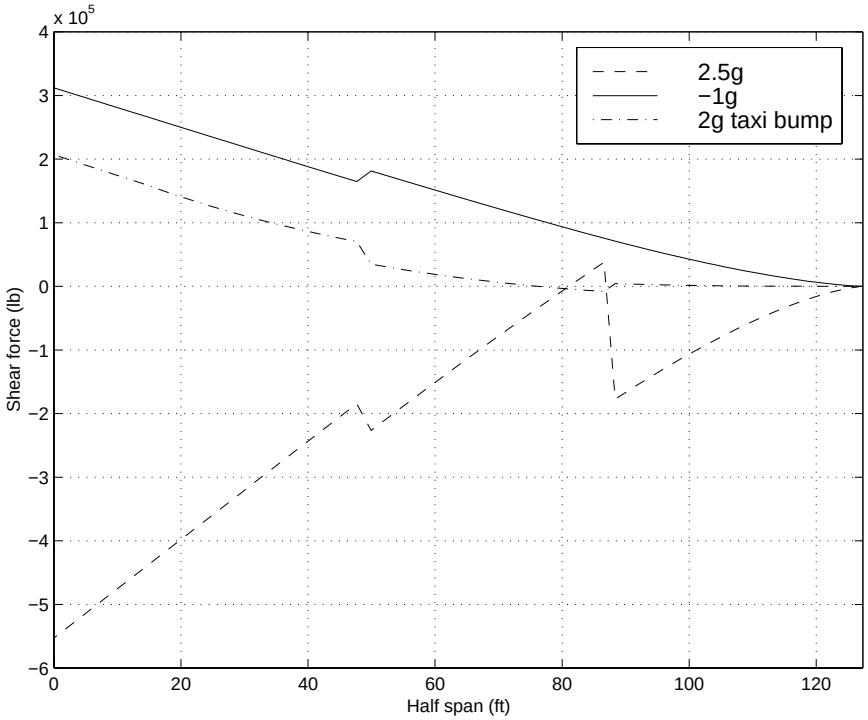

Figure 5.3 Shear force distributions at the 2.5g and -1.0g maneuver and 2.0g taxi bump load conditions (a) tip-mounted engines (b) under-wing engines.

(a)

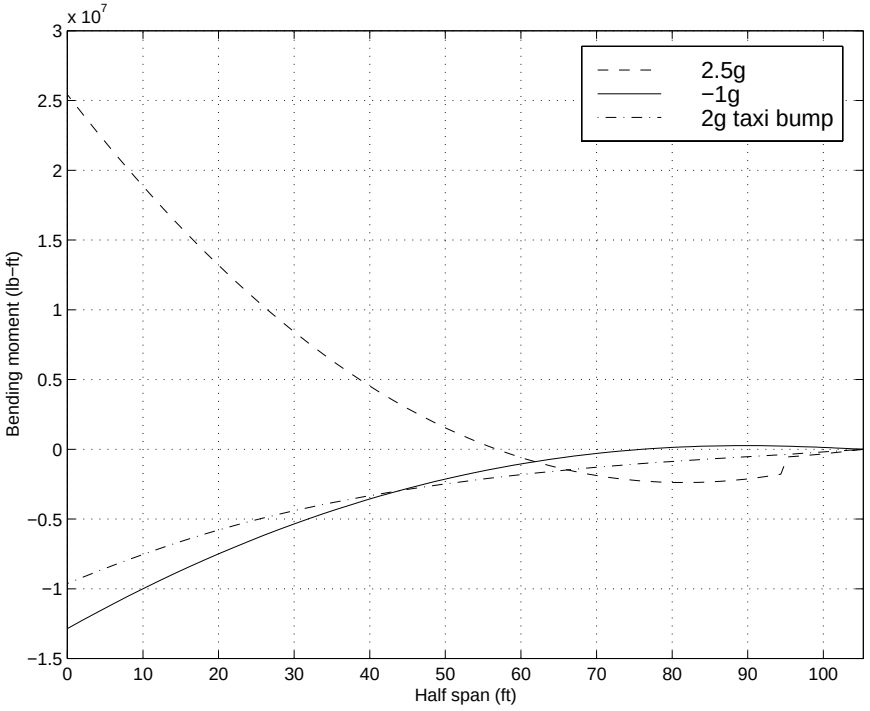

(b)

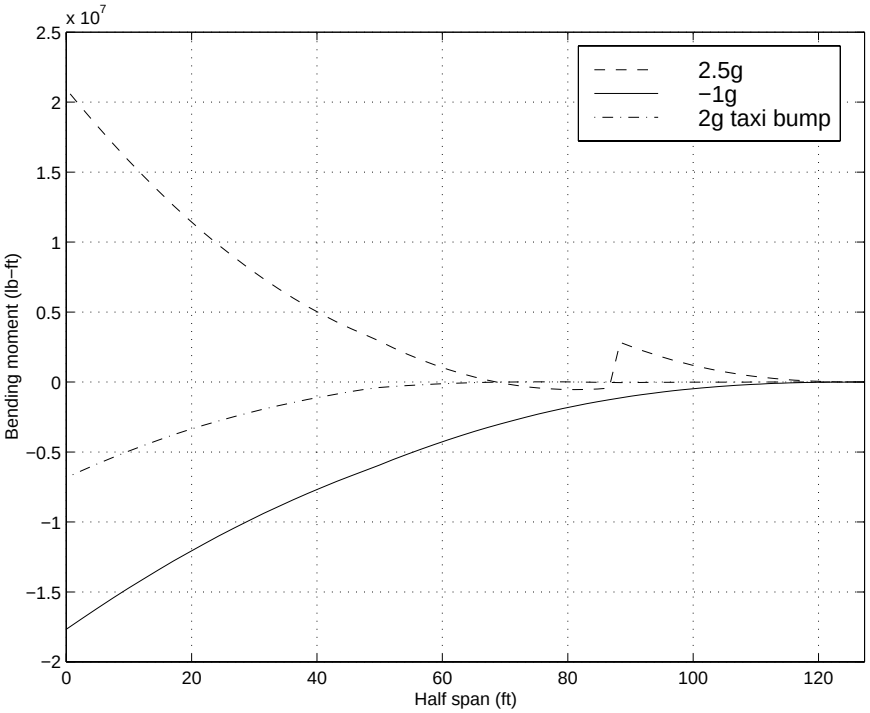

Figure 5.4 Bending moment distributions at the 2.5g and -1.0g maneuver and 2.0g taxi bump load conditions (a) tip-mounted engines (b) under-wing engines.

5.6 *Vertical Deflection Distributions*

The vertical deflection distributions at the critical load conditions are shown in Figure 5.5. Without constraining the deflections, the high aspect ratio wing with small thickness to chord ratios, will likely lead to wingtip or engine ground strikes, since the wing is only designed to satisfy the material yield condition. Hence, an optimization procedure described in section 3.2.1 is imposed to distribute an optimum thickness distribution for the taxi bump load condition to prevent possible wingtip or engine ground strikes. Therefore, a displacement constraint is implemented in the global optimization. A minimum allowable wingtip or engine deflection of 20 *ft* is enforced at the taxi bump load condition to account for the weight or the engine ground strike. The 20 *ft* displacement limit was determined based on the fuselage diameter of 20.33 *ft* and the landing gear length of 7 *ft*. Equations (3.26) and (3.27) show how the maximum deflection for each configuration is calculated. For the current study, the pylon height and the nacelle diameter are fixed to 4.1 and 12.54 *ft* for both configurations, respectively. Based on the values obtained from the taxi bump deflection distributions equations (3.26) and (3.27), the tip-mounted engine design shows a maximum deflection of 20 *ft* at the wingtip and the under-wing engine design shows a maximum deflection of 19.1 *ft* at the engine location. The distributions shown in Figure 5.5 only represent the wing deflection. The vertical distance corresponding to pylon height and nacelle diameter is not included. Both configurations satisfy the wing strike displacement constraint.

Furthermore, the engine location of the under-wing engine configuration is driven considerably inboard from where it might otherwise have been anticipated. The engines can provide inertia relief and hence a further outboard location will result in a lower wing weight. However, due to the maximum deflection constraint in the taxi bump analysis, the optimizer locates the engines more inboard and determines the optimization trade between the spanwise engine location and the wing material thickness distribution.

(a)

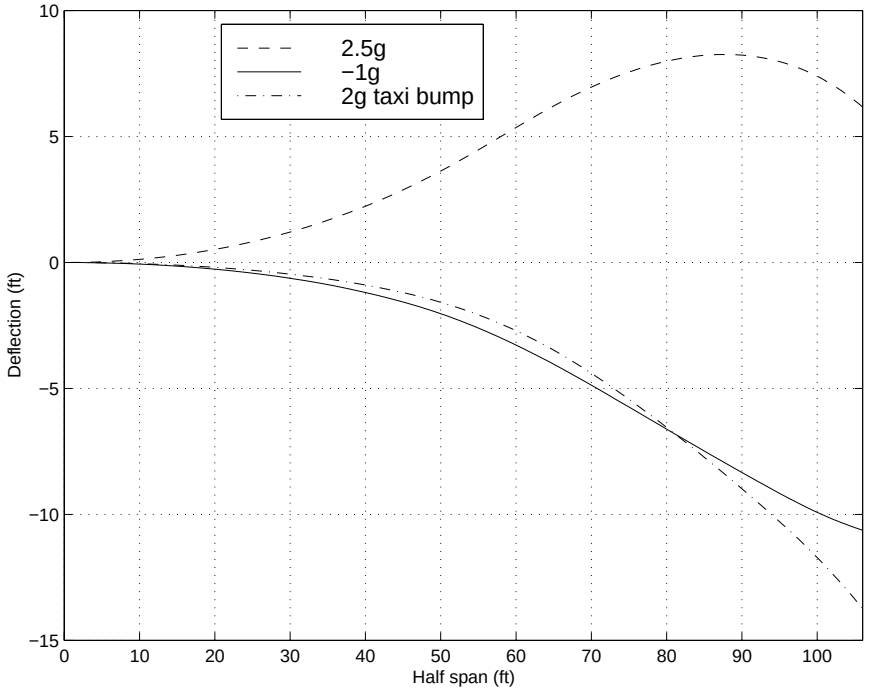

(b)

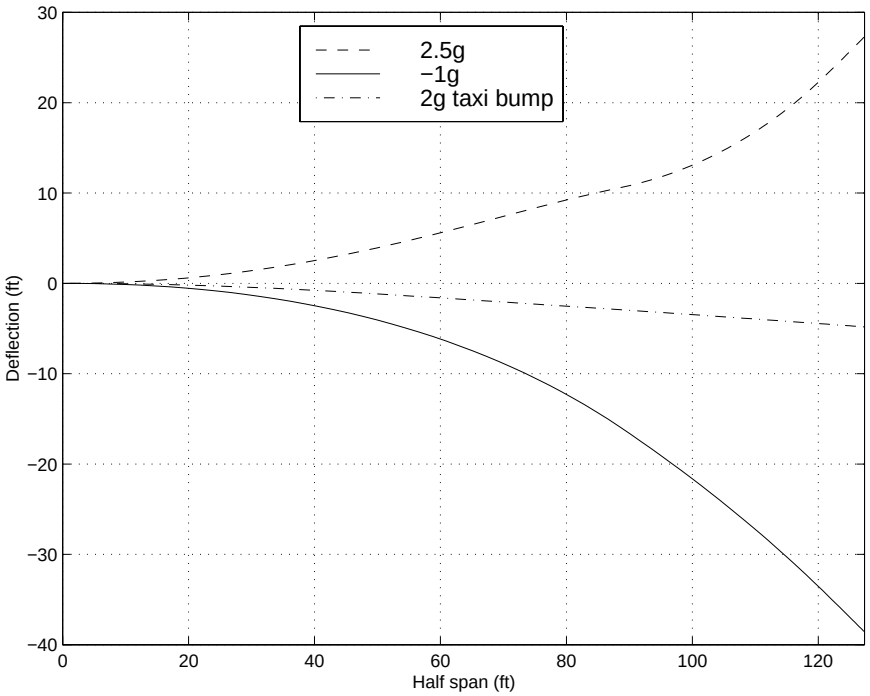

Figure 5.5 Vertical deflection distributions at the 2.5g and -1.0g maneuver and 2.0g taxi bump load conditions (a) tip-mounted engines (b) under-wing engines.

5.7 *Material Thickness Distributions*

Figure 5.6 depicts the required wing box material thickness distributions due to bending only at the 2.5g and -1.0g maneuver and 2.0g taxi bump load conditions. These plots reveal that for some regions along the wing half span the -1.0g load condition is the dominant load condition and for other regions the 2.5g load condition is the dominant one. Thus, at each segment, the maximum thickness distribution on the figure defines the required thickness. Two separate skin thickness distributions are obtained for the taxi bump load condition. The dash-dotted line is the distribution due to the material allowable stress and was obtained based on the fully stressed criterion while the dotted line is the distribution due to the maximum displacement constraint which was discussed in the previous chapter. Moreover, the taxi bump thickness distributions show that the required skin thickness distribution due to this load condition may violate the required skin thickness distribution due to the maneuver conditions. This is avoided by adding the required extra thickness due to the taxi bump load condition at the aforementioned wing locations to the required thickness due to the maneuver conditions. A minimum gauge of 0.055 *in* is used as a lower bound for the skin thickness distributions. For the current configurations, at the taxi bump load condition, the material thickness distributions due to bending are only exceeding the minimum gauge thickness and the one corresponding to the tip-mounted engine configuration only violates the maneuver envelope. The material thickness distribution due to the displacement constraint is not active for either configuration. The outer thickness envelope in both figures show the design material thickness. The two sharp changes on the thickness distributions at the 2.5g load condition are due to the moments applied by the strut horizontal force component acting on the strut offset as can be seen on the bending moment diagrams (Figure 5.4). This is most likely the reason which prevents the material thickness distribution due to the ground strike displacement constraint becoming critical.

(a)

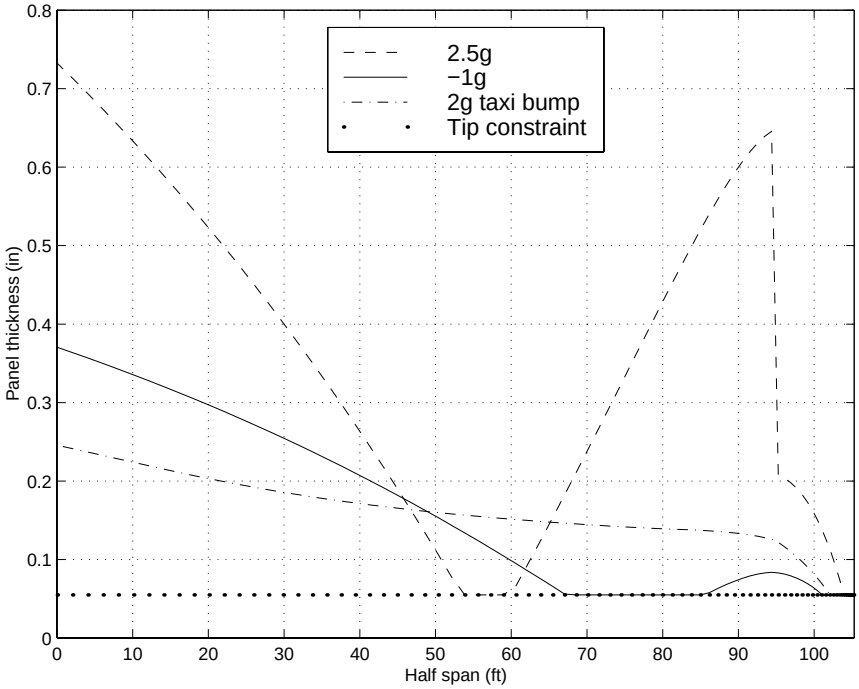

(b)

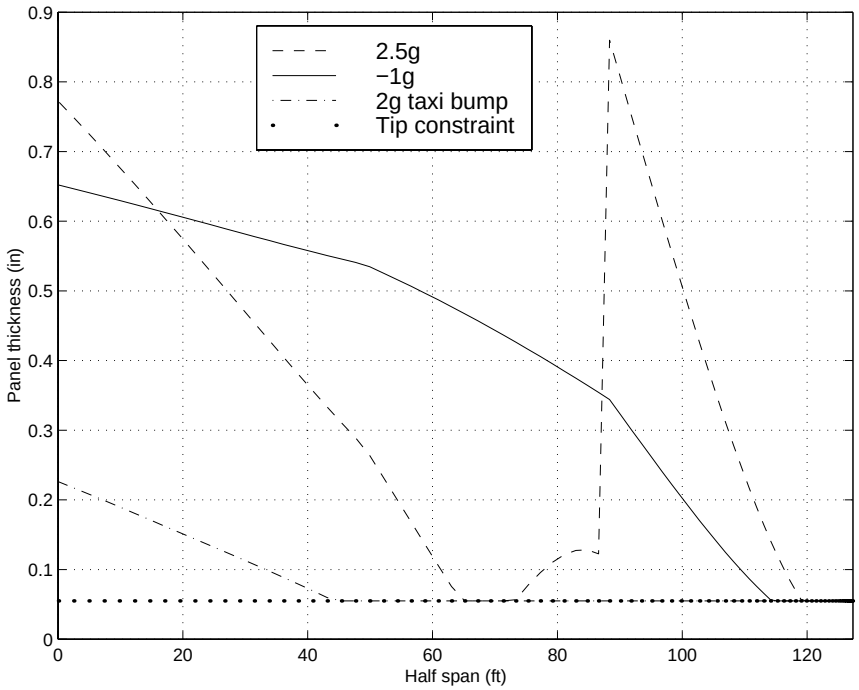

Figure 5.6 Material thickness distributions at the 2.5g and -1.0g maneuver and 2.0g taxi bump load conditions (a) tip-mounted engines (b) under-wing engines.

5.8 *Load Alleviation*

To further reduce the wing weight and thus to increase the overall aircraft performance, modern electronic control systems in concert with the fly-by-wire technology offer a considerable potential for active load alleviation.

The use of active load control has been investigated to understand the effects of load alleviation on potential bending weight reduction. The aileron is used to shift approximately 10% of the lift inboard at the maneuver load conditions. By deflecting the aileron, the wing intends to wash out at the tip, thereby shifting the lift inboard (Kulfan et al., 1978). Hence, this phenomenon produces a bending weight reduction at the root since the lift distribution centroid is also moved inboard. Moreover, Young et al. (1998) explains how trailing edge flaps are used for load alleviation on the F/A-18E/F aircraft. As the aircraft pulls load factor, the trailing edge flap is scheduled down by the flight control system as a function of load factor. The result is a modification of the lift distribution with less lift on outboard and more on inboard. This reduces wing bending moment, which results in a reduction in wing weight.

Table 5.4 summarizes the optimum configurations. The under-wing engine configuration shows more improvements in both aerodynamics and structures than those of the under-wing engine configuration without active load alleviation. Active load alleviation is a practical means to reduce the structural weight. Because the under-wing engine configuration is an aerodynamic driven design, active load alleviation not only reduced the wing weight but also helped with aerodynamic improvements (a higher *L/D*) due to its design behavior. Also, the tip-mounted engine configuration shows a reduction in wing weight compared to that of the same configuration without active load alleviation. However, aerodynamic improvements are not observed for the tip-mounted engine configuration employing active load alleviation compared to the case of the same configuration without active load alleviation since it is a structurally driven design. In general, the results show that this mechanism could assist in achieving a significant reduction in the bending weight. Further discussion will follow in the next few sections.

Table 5.4 Optimum strut-braced wing configurations with active load alleviation

	Strut-braced wing tip-mounted Engines w/active load alleviation	Strut-braced wing under-wing engines w/active load alleviation
Wing half span (*ft*)	91.27	117.16
Wing-strut intersection (*ft*)	82.14 (90%)	76.27 (65%)
Wing break location (*ft*)	82.14 (90%)	76.27 (65%)
Wing 1/4 chord sweep (*deg*)	32.02	27.80
Strut 1/4 chord sweep (*deg*)	22.27	19.00
Strut offset length (*ft*)	3.93	2.30
Wing root chord (*ft*)	30.03	25.19
Wing break chord (*ft*)	12.59	13.66
Wing tip chord (*ft*)	10.64	7.48
Strut root chord (*ft*)	6.616	6.616
Strut tip chord (*ft*)	6.616	6.616
Wing root *t/c*	0.1539	0.1291
Wing break *t/c*	0.0642	0.0639
Wing tip *t/c*	0.0500	0.0500
Strut *t/c*	0.0800	0.0800
Aspect ratio	8.97	14.34
Wing area (ft^2)	3,713	3,827
Strut force (*lbs*)	24,281	185,353
Slack load factor	0.8	0.8
Cruise *L/D*	22.64	25.98
Engine weight (*lbs*)	12,992	10,889
Spanwise engine location (*ft*)	91.27 (100%)	45.69 (39%)
Zero fuel weight (*lbs*)	315,930	320,394
Fuel weight (*lbs*)	172,367	150,554
Wing weight (*lbs*)	41,416	50,938
Takeoff gross weight (*lbs*)	488,297	470,955

The current analysis method assumes a rigid wing when calculating the aerodynamic loads. In future research, the capability to model aeroelastic deflections will be added. A flexible wing may be designed to shift the load distribution inboard, especially the swept wingtips which tend to wash out. For the strut-braced wing, another mechanism is possible to produce a wash out; the use of unequal forces on the front and rear spars to produce required wing twist. Since the current design code does not model the effects of passive load alleviation, our current wing estimates are somewhat

conservative. In the next section the weight results obtained by implimenting the active load alleviation are presented.

5.9 *Wing Weight Results and Comparison*

The wing weight breakdowns of the aluminum and composite strut-braced and cantilever wing configurations are tabulated in Table 5.5. The effect of active load alleviation on the wing weight and takeoff gross weight is also reflected in the tabulated data. Figure 5.7 and Figure 5.8 show the wing weight and takeoff gross weight comparisons. The wing weight varies between 73,767 *lbs* for the cantilever wing to 45,631 *lbs* for the strut-braced composite wing with tip-mounted engines. Comparing the strut-braced wing weights with the cantilever wing shows that the strut-bracing can reduce the wing weight and takeoff gross weight considerably. The consequence is a 38% weight savings for the composite strut-braced wing with tip-mounted engines and an 18% weight savings for the composite strut-braced wing with under-wing engines compared to the composite cantilever wing. Also, the use of a composite material has reduced the wing weight of the tip-mounted engine design by 18% and the under-wing engine design by 8%. As mentioned earlier, the tip-mounted engine design is a structurally dominated design and thus a lighter wing with greater drag is achieved. On the other hand, the under-wing engine design is an aerodynamically dominated design and thus less drag and a heavier wing is obtained.

Moreover, active load alleviation via aileron deflection is considered. This is done by transferring 10% of the lift inboard at the maneuver load conditions. Therefore, a wing weight reduction and a total takeoff gross weight reduction are expected. According to Table 5.5, the weight reduction corresponding to the under-wing engine configuration is more pronounced than that corresponding to the tip-mounted engine configuration. Since the strut-braced wing with under-wing engines is aerodynamically more efficient, and according to Figure 5.6-(b) both maneuver cases contribute to the weight more or less equally, the use of active load alleviation increases the structural efficiency significantly without losing its aerodynamic

advantages (there may even be some aerodynamic gain according to the results). So that, active load alleviation can luxuriate in both structural and aerodynamic benefits. However, the strut-braced wing with tip-mounted engines does not exhibit a notable weight decrease since it is a structurally dominated design. Also, as shown in Figure 5.6-(a), the material thickness distribution at the -1.0g load condition is barely active in determining the wing weight and hence load alleviation at this load condition is not very effective. No aerodynamic efficiency is seen to be gained (there may be even some loss) at the expense of a further decrease in the aspect ratio due to a further wing weight decrease. Therefore, the takeoff gross weight does not decrease as it was expected. The under-wing engine configuration shows a 16% savings in wing weight and 3.8% savings in takeoff gross weight while the tip-mounted engine configuration shows a 9.2% savings in wing weight and 0.5% savings in takeoff gross weight relative to their counterparts without active load alleviation.

Table 5.5 Takeoff gross weight and wing weight breakdowns (*lbs*)

	TME[*] Met.	UWE[#] Met.	TME[%] Comp.	UWE[&] Comp.	TME/C[$] w/ALA	UWE/C[+] w/ALA	Cant.[¶] Comp.
Strut offset bending	614	1,030	576	1,263	326	836	N/A
Strut tension/bending	2,779	6,889	2,543	7,777	1,152	5,627	N/A
Wing bending	27,938	38,824	22,115	38,382	17,550	28,780	60,932
Wing shear and flaps	21,021	21600	18,217	18,654	18,133	17,928	21,049
Wing nonstructural	8,700	9,647	6,781	7,564	6,731	7,045	9,921
Total strut offset	1,393	2,001	1,089	1,819	707	1,357	N/A
Total strut	6,309	13,386	4,808	11,199	2,492	9,134	N/A
Total wing	47,452	50,208	39,556	47,062	38,072	40,291	73,557
Inertia relief factor	0.054	0.075	0.046	0.079	0.036	0.061	0.091
Total wing structure	55,378	65,776	45,631	60,323	41,416	50,938	73,767
Takeoff gross weight	519,816	523,297	490,687	489,826	488,297	470,955	540,689

[*] Tip-mounted engines, metallic
[#] Under-wing engines, metallic
[%] Tip-mounted engines, composite
[&] Under-wing engines, composite
[$] Tip-mounted engines, composite with active load alleviation
[+] Under-wing engines, composite with active load alleviation
[¶] Cantilever, composite

For the obtained configurations, the takeoff gross weight varies between 470,955 *lbs* for the composite strut-braced wing aircraft with under-wing engines employing active load alleviation to 540,689 *lbs* for the composite cantilever wing aircraft. The

composite strut-braced wing with tip-mounted engines shows a 9.2% savings and the composite strut-braced wing with under-wing engines shows a 9.4% decrease in takeoff gross weight compared to their composite cantilever wing counterpart. Using a composite material in the wing structures has saved 5.6% weight for the tip-mounted engine aircraft and 6.4% weight for the under-wing engine aircraft. Furthermore, applying active load alleviation has reduced the takeoff gross weight by 3.8% compared to the strut-braced wing aircraft with under-wing engines. However, this mechanism has not been as effective for the strut-braced wing aircraft with tip mounted engines. A maximum total weight savings of 13% has been achieved relative to the composite cantilever wing. In general, implications of composite materials and active load alleviation challenge the tradeoffs between the aerodynamics and structures and result in both aerodynamic improvements and weight savings. Figure 5.8 depicts the takeoff gross weight comparison.

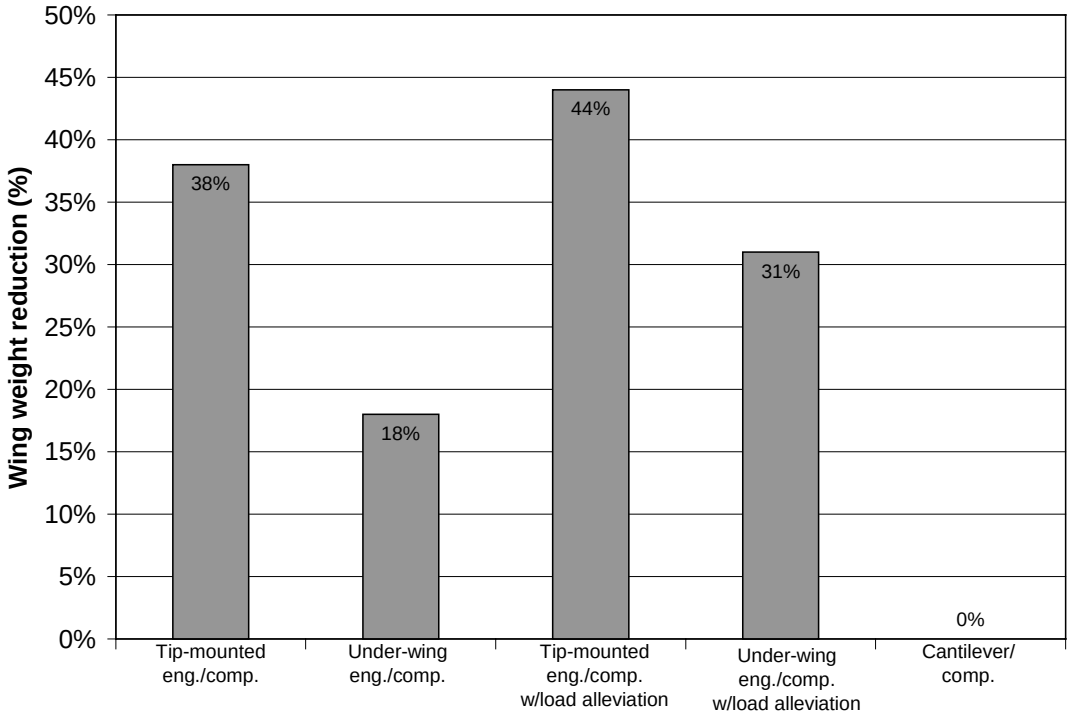

Figure 5.7 Wing weight comparison.

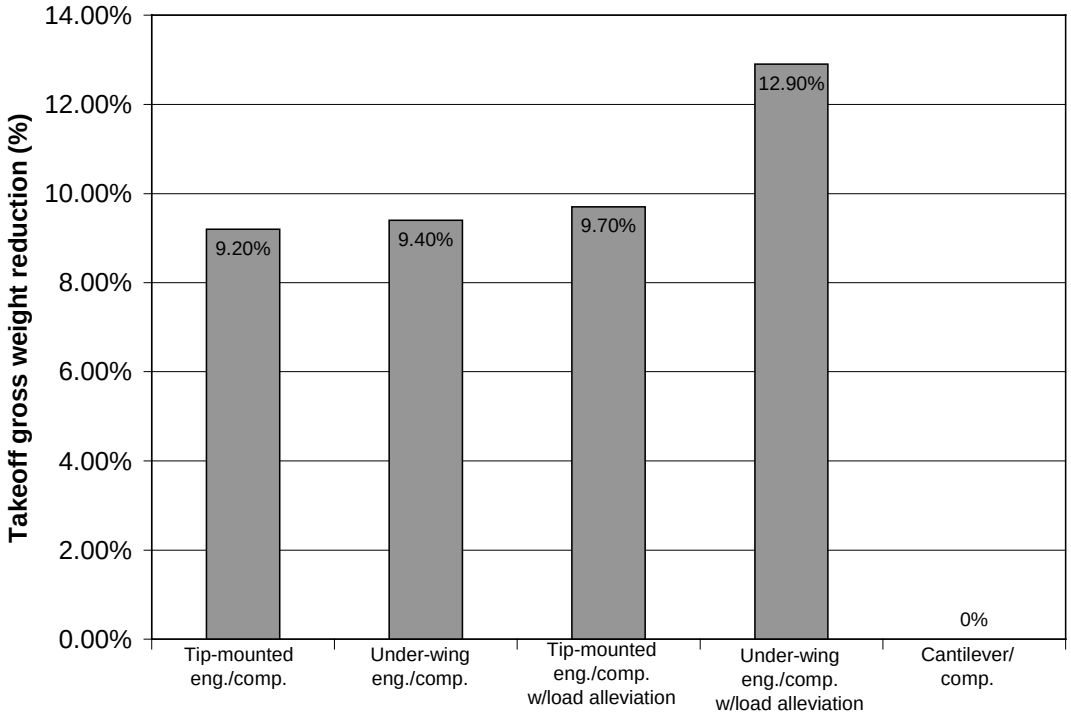

Figure 5.8 Takeoff gross weight comparison.

5.10 *Wing weight and Takeoff Gross Weight Tradeoff Studies*

The following sections discuss the variations of the wing weight and takeoff gross weight versus the strut force, strut offset length, and wing-strut intersection. These factors are particularly important in the determination of wing weight from the structural point of view. At each point the whole configuration is optimized for minimum takeoff gross weight.

5.10.1 Variations of the Wing Weight and Takeoff Gross Weight Versus the Strut Force

In the original strut-braced wing configuration, the strut force is a design variable in the global optimization and is determined by the optimizer for minimum wing weight. A tradeoff study was performed to evaluate the effect of different strut forces on the wing weight and takeoff gross weight associated with the tip-mounted engine and

under-wing engine configurations as shown in Figure 5.9 and Figure 5.10. The strut force is varied between zero to 300,000 (*lbs*) for the tip-mounted engines and zero to 400,000 for the under-wing engines.

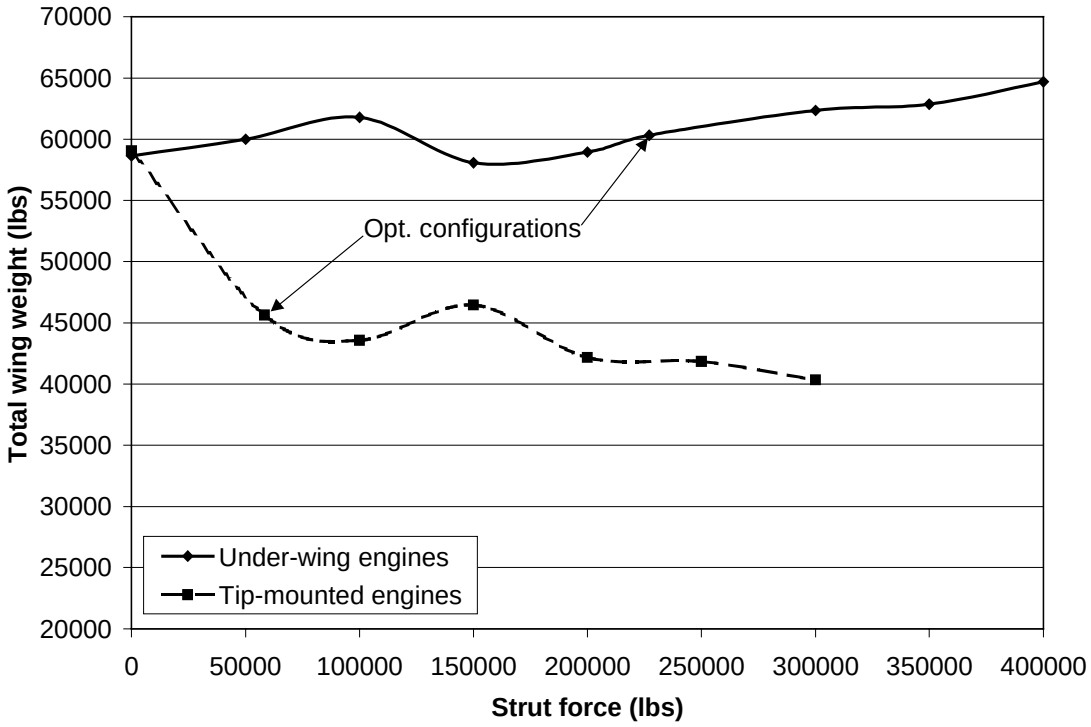

Figure 5.9 Total wing weight versus the strut force.

The tip-mounted engine and under-wing engine configurations show maximum changes of 3.2% and 9.3% in wing weight, respectively. The two designs exhibit two different behaviors. The wing weight associated with the tip-mounted engine design tends to decrease by increasing the strut force while the wing weight associated with the under-wing engine design tends to increase by increasing the strut force. These behaviors can be better understood by looking at the takeoff gross weight curves. Both designs have the highest takeoff gross weight values at zero strut force. When the strut force is zero, the wing weight of the tip-mounted engine design shows a significant growth by increasing the panel material thickness to be able to withstand the required lift without losing that much of its aerodynamic advantages. This, is because it is a design dominated by structures considerations as discussed before.

Thus, due to the ripple-through effect, the takeoff gross weight also increases and reaches its maximum value. However, the wing weight of the under-wing engine design does not show too much change from its optimum configuration (even it is a bit lighter). This is due to the fact that this design configuration is aerodynamically dominated therefore the *t/c*'s increase to be able to withstand the required lift without too much change in the wing weight. Hence, on account of drag rise, the takeoff gross weight also increases and reaches its maximum value. The tip-mounted engine and under-wing engine configurations show maximum changes of 16% and 25% in takeoff gross weight, respectively.

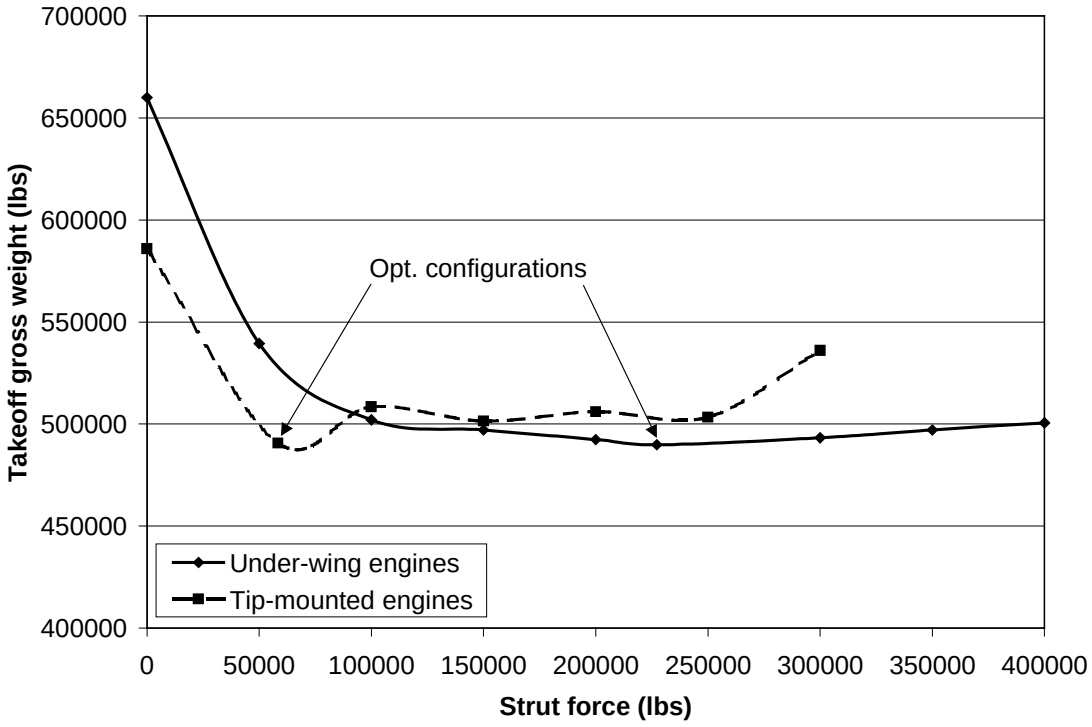

Figure 5.10 Takeoff gross weight versus the strut force.

5.10.2 Variations of the Wing Weight and Takeoff Gross Weight Versus the Strut Offset Length

Another sensitive factor in wing weight and takeoff gross weight is the strut offset length. This offset distance is determined by the global optimizer by balancing the

two conflicting requirements of decreasing the interference drag by increasing the strut offset and decreasing the offset weight by decreasing its length. To understand the effect of the strut offset length on the wing weight and takeoff gross weight, it is varied from 1 to 5 *ft*. The variations are shown in Figure 5.11 and Figure 5.12 for both configurations. Maximum changes 5.4% and 5.2% in wing weight are obtained corresponding to the tip-mounted engine and under-wing engine designs, respectively.

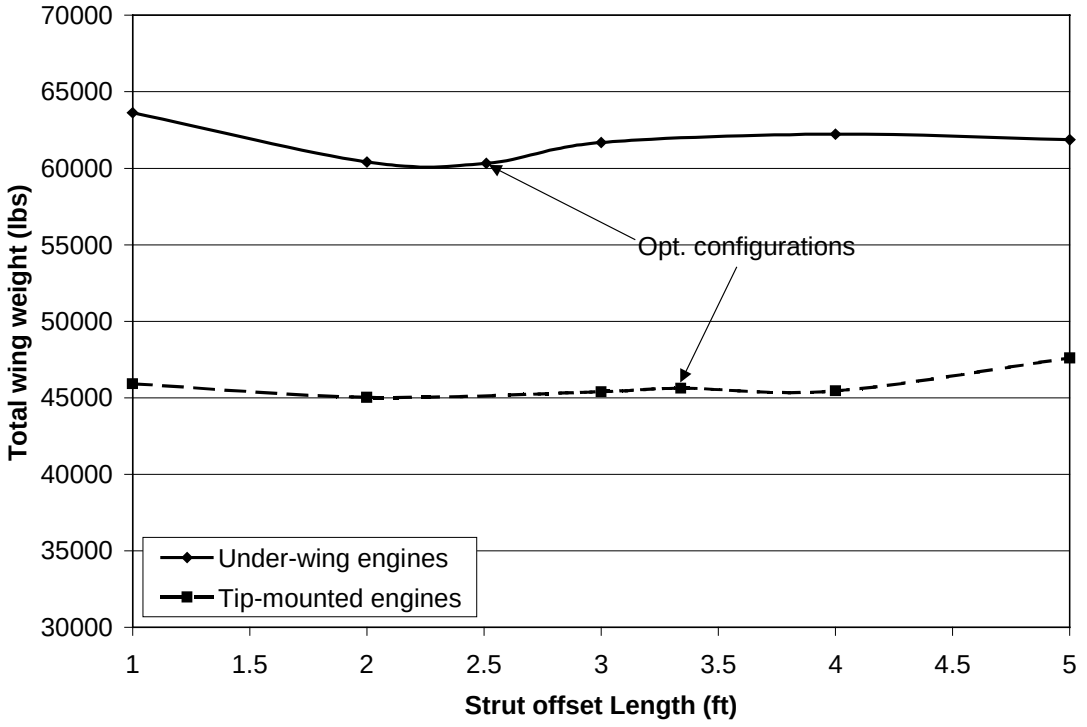

Figure 5.11 Total wing weight versus the strut offset length.

In addition to the strut optimum force for bending material weight relief, the strut offset also induces a moment opposite to the bending moment due to the lift which results in additional bending material weight relief. Hence, this fact will add to the flexibility of the optimization procedure in determining the optimum strut force as well as the strut offset length.

According to Figure 5.12, the takeoff gross weight is greatest when the offset length is 1.0 *ft* (it's lower limit in the optimization, takeoff gross weight increases tremendously

as the offset length is further reduced). The shorter the offset length is, the more interference drag is produced. Within the range of 2.5 to 4.0 *ft*, the takeoff gross weight remains practically unchanged. Consequently, it can be concluded that the interference drag and the offset weight compensate for one another. When the offset length is less than 2.5 *ft*, due to the increase in the interference drag, the takeoff gross weight also increases. And, when the offset length is more than 4.0 *ft* due to the increase in the offset weight and also other factors, the takeoff weight grows. The maximum changes in takeoff gross weight associated with the tip-mounted engine and under-wing engine designs are obtained 4.7% and 1.9%, respectively.

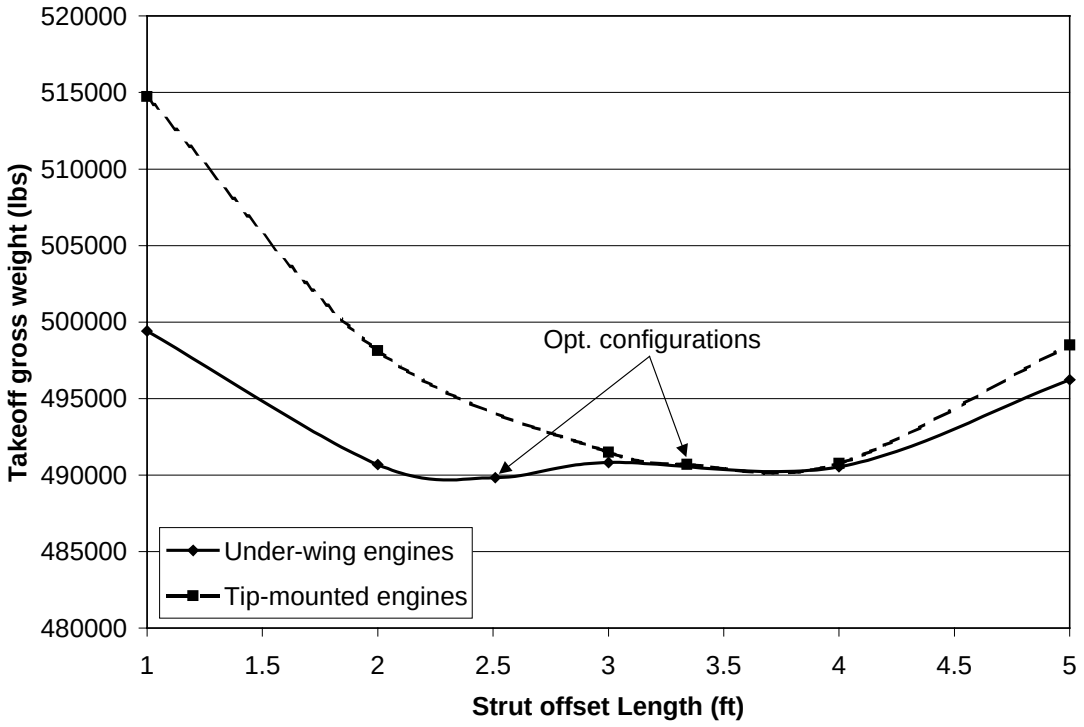

Figure 5.12 Takeoff gross weight versus the strut offset length.

5.10.3 Variations of the Wing Weight and Takeoff Gross Weight Versus Wing-Strut Intersection Location

To evaluate the influence of the wing-strut intersection location on the wing weight and takeoff gross weight, a tradeoff study is performed. The wing-strut intersection

location is varied from 40% to 90% of the half span. Figure 5.13 and Figure 5.14 depict the variations of the wing weight and takeoff gross weight versus the wing-strut intersection, respectively. This design variable plays an important role in determining the strut offset length and the optimum strut force. A longer strut offset may cause greater offset weight due to the induced bending moment by the horizontal strut force component. This results in a smaller strut force. The smaller strut force can regain its effect on reducing the bending material weight by an increase in the moment arm (distance from the root to the wing-strut intersection). This is the situation which most likely took place in the optimization trend associated with the tip-mounted engine configuration. On the other hand, for the under-wing configuration the wing-strut intersection was forced more inboard. This issue changes the optimization trend associated with this design configuration. Hence, the strut offset can further reduce to save its weight and then a greater strut force could be applied.

Significant variations in the wing weight are seen for neither configuration. This is mostly because of the tradeoff between this design variable, the strut offset length, and the strut force. The tip-mounted engine design shows a maximum change of 5.3% while the under-wing engine design shows that of 9.6% in wing weight.

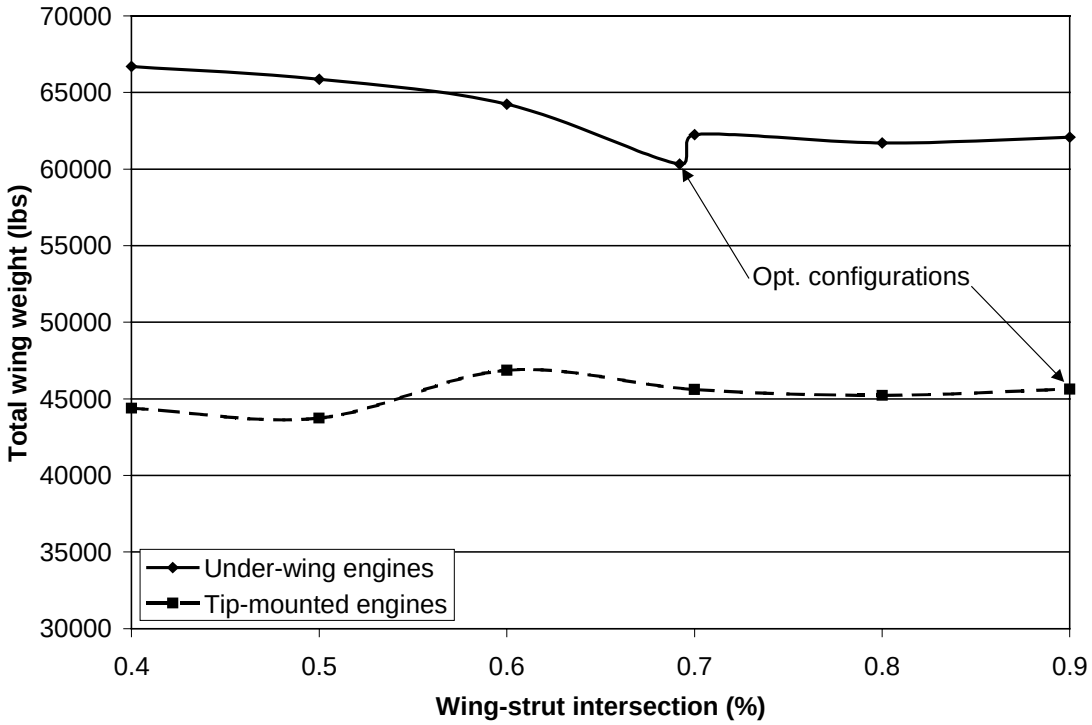

Figure 5.13 Total wing weight versus the wing-strut intersection.

According to Figure 5.14, the two configurations exhibit different behaviors in the takeoff gross weight. The takeoff weight of the tip-mounted engine design increases as the wing-strut intersection location moves outwards, up to a point that is a bit more than the mid wing. Then, the trend reverses. The takeoff weight of the under-wing engine design, on the other hand, decreases up to about 0.7 of the half span (optimum configuration) and then begins to increase. The maximum changes in takeoff gross weight associated with the tip-mounted engine and under-wing engine designs are 5% and 3.9%, respectively.

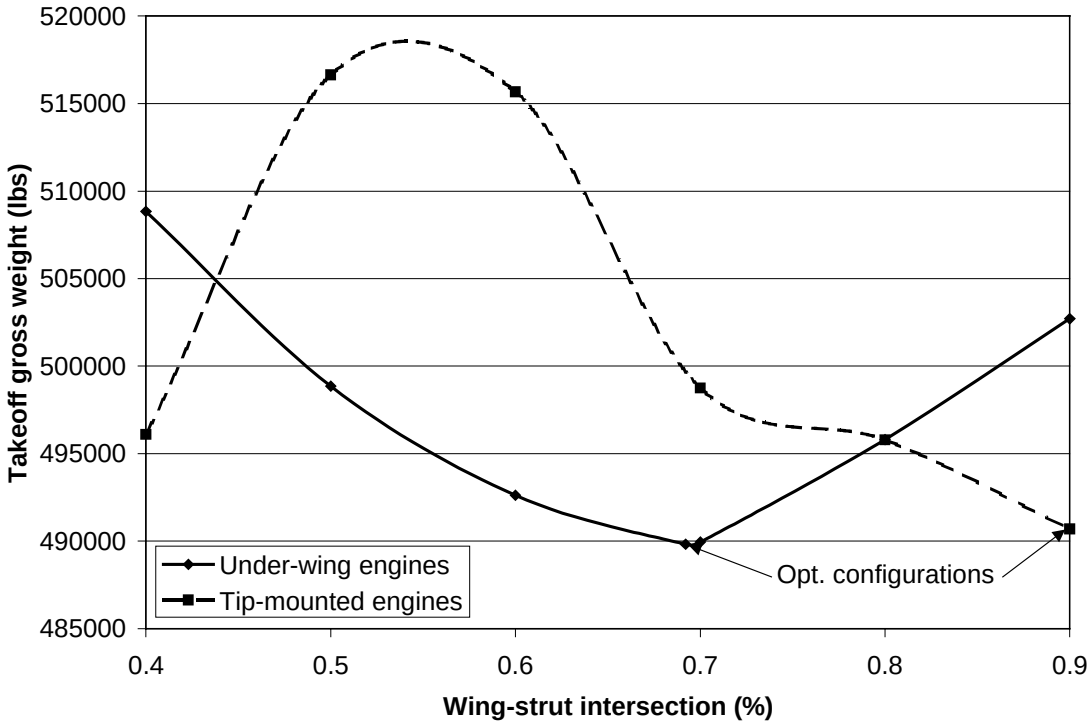

Figure 5.14 Takeoff weight versus the wing-strut intersection.

Chapter 6 A Preliminary Static Aeroelastic Analysis of the Strut-Braced Wing Using the Finite Element Method

To reduce weight, aircraft structural parts are commonly built with thin-walled flexible structures. Thin-walled flexible structures such as wings, when encountering significant aerodynamic loads, show large elastic deformations and may be prone to flutter. The elastic deformations induce additional aerodynamic loads which can strongly affect the aircraft stability and aerodynamic load distributions and thus the overall performance while flutter results in catastrophic structural failure. Other aeroelastic phenomena such as divergence and control effectiveness can also be important. Hence, in aircraft conceptual and preliminary design phases special attention should be paid to aeroelastic effects on structural design which yields to the utilization of multidisciplinary design concepts and optimization strategies (Niu, 1988, Bisplinghoff et al., 1983, and Honlinger et al., 1998).

The truss-braced wing has a high aspect ratio made of thin airfoil sections. Preliminary studies showed that the wing may undergo large deformations at critical maneuver load conditions. Thus, static aeroelastic effects should be considered to account for more realistic aerodynamic load distributions since significant differences may occur in wing weight estimation compared to rigid wing weight estimation. The introductory work for bending material weight estimation uses load distributions obtained from the optimum spanload for minimum induced drag method (Grasmeyer, 1997) which does not account for static aeroelastic effects. Studying the aeroelastic influences requires knowledge of the torsional stiffness distribution along the wing semispan. Such a capability does not exist in the double-plate model. Therefore, the MSC/NASTRAN aeroelastic module (Rodden and Johnson, 1994) is used to create a NASTRAN finite element model for the strut braced wing. The MSC/NASTRAN optimization module (Moore, 1994) will be integrated (future work) with the static aeroelastic analysis to perform structural optimizations to produce bending material

weight response surfaces to be used in the truss-braced wing MDO code for different truss-braced wing configurations. The work of Rais-Rohani (1991), Huang (1994), and Balabanov (1997) can be mentioned in this category. The use of response surfaces, as mentioned in previous sections, reduces high computational costs associated with detailed CFD and FEM models. Response surfaces to represent structural and aerodynamic responses have been used at Virginia Tech for designing the High Speed Civil Transport (HSCT) with a considerable success for several years. The reader can refer to Giunta et al., 1996, Giunta et al., 1997, Hutchison et al., 1994, and Knill et al., 1998 for further information.

6.1 *MSC/NASTRAN*

MSC/NASTRAN is one of the most common multipurpose commercial finite-element software packages that is used in the aircraft industry. NASTRAN was developed at NASA during the late 1960's period and was released for public use in 1970. Since then, it has evolved and several different modules have been integrated to it. MSC/NASTRAN has capabilities of performing linear static analysis, dynamic analysis, non-linear analysis, aeroelastic analysis, design sensitivity and optimization, numerical methods, and thermal analysis. For this study, aeroelastic and design sensitivity and optimization analysis modules are used. The following is a brief description of each.

6.1.1 MSC/NASTRAN Aeroelastic Analysis Module

The aeroelastic analysis module is capable of performing aeroelastic analyses in both subsonic and supersonic regimes. The model can be simulated structurally and aerodynamically with separate grid points. One subsonic and three supersonic lifting surface aerodynamic theories as well as strip theory are available in this module. The Doublet-Lattice theory which can account for interference among multiple lifting surfaces and bodies is used for subsonic aerodynamics while supersonic theories are the Mach Box method, Piston Theory, and the ZONA51 method for multiple interfering lifting surfaces. Moreover, splining techniques for both lines and surfaces

are provided to interpolate the load distribution from the aerodynamic grid points to structural degrees of freedom. Furthermore, the equations for static equilibrium are solved to determine the structural load distribution on an elastic vehicle in trimmed flight. The solution process leads to aerodynamic stability derivatives, lift and moment curve slopes and lift and moment coefficients due to control surface rotation, and trim variables, i.e. angle of attack and control surface setting, as well as aerodynamic and structural loads, structural deflections, and element stresses (Rodden and Johnson, 1995).

6.1.2 MSC/NASTRAN Design Sensitivity and Optimization Module

The design sensitivity and optimization module has several built-in numerical optimization techniques. The optimization algorithms in MSC/NASTRAN belong to the gradient-based optimization methods. For a general optimization problem, the method of feasible directions is used. Moreover, finite difference approximations are employed to evaluate the derivatives. Approximate design models are also included. Output in design sensitivity and optimization may be generated from (1) MSC/NASTRAN analysis, (2) design sensitivity analysis, (3) design optimization (including optimization output), and (4) convergence tests and design model updates (Moore, 1995).

6.2 *MSC/NASTRAN Element Discriptions Used for Wing Modeling*

In this section, the MSC/NASTRAN finite element model details are explained. The developed model uses the CQUAD4 and CTRIA3 membrane and shell elements and the CROD truss element.

6.2.1 CQUAD4 Shell Element

The CQUAD4 element is a typical isoparametric quadrilateral plate and shell element. Although there are variety of elements available in the MSC/NASTRAN library, the CQUAD4 element is the most commonly used two-dimensional element. This

element can be used to model membranes, plates, and thick and thin shells. The geometry and coordinate systems of a CQUAD4 element is shown in Figure 6.1. An element coordinate system and a material coordinate system are used in a CQUAD4 element. Using a material coordinate system different from the element coordinate system is useful when the material properties are orthotropic or anisotropic. The CQUAD4 is a 4-noded, 24 degree of freedom element with 6 degrees of freedom per node $(u, v, w, \theta_x, \theta_y, \theta_z)$ (Lee, 1997).

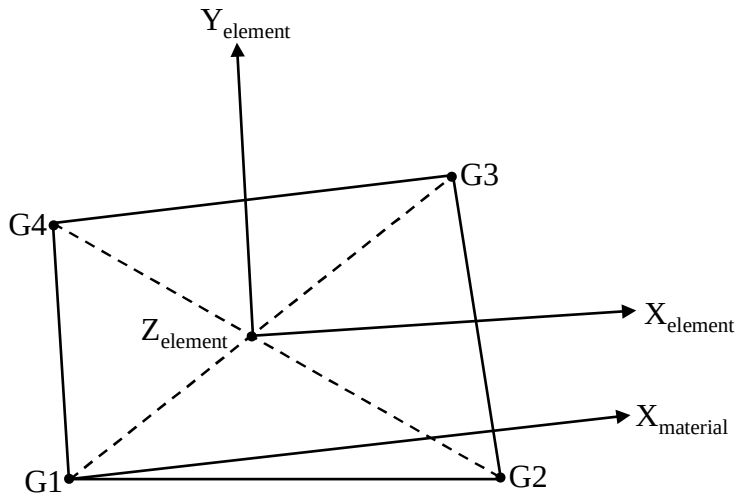

Figure 6.1 CQUAD4 element with coordinate systems.

6.2.2 CTRIA3 Shell Element

The CTRIA3 element is a typical isoparametric triangular plate and shell element. This element can be used to model membranes, plates, and thick and thin shells. The geometry and coordinate systems of a CTRIA3 element is shown in Figure 6.2. An element coordinate system and a material coordinate system are used in a CTRIA3 element. The CTRIA3 is a 3-noded, 18 degree of freedom element with 6 degrees of freedom per node $(u, v, w, \theta_x, \theta_y, \theta_z)$ (Lee, 1997).

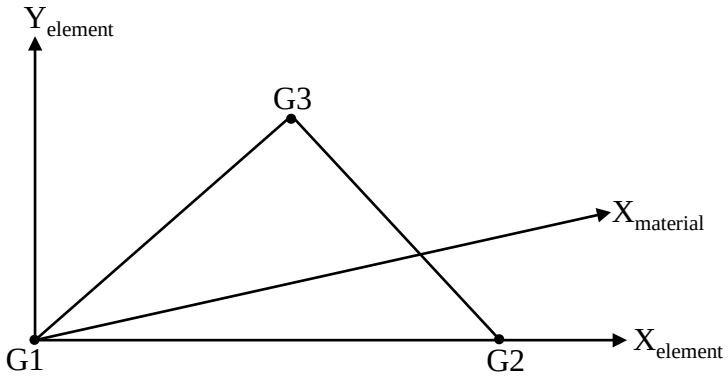

Figure 6.2 CTRIA3 element with coordinate systems.

6.2.3 CROD Truss Element

The CROD element is a one-dimensional axial force and axial torsion (truss) element. Figure 6.3 shows the geometry and coordinate system of a CROD element. The CROD is a 2-noded, 6 degree of freedom element with 3 degrees of freedom per node (u, v, θ_x).

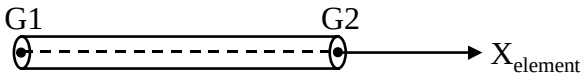

Figure 6.3 CROD element.

6.3 *Strut-Braced Wing Finite Element Arrangement*

Truss-braced wing configurations are highly unconventional. Thus, available weight estimation software packages are not capable of performing weight analyses on such wings. Also, analytical-based methods cannot be employed for structural analyses of such structures as was used for the single-strut-braced wing. Consequently, numerical techniques such as the finite element method should be used to perform structural analyses and optimization of complex truss-braced wing configurations. For the time being, only the strut-braced wing configuration with tip-mounted engines is considered to develop the finite element model. This can be assumed as the first step

towards modeling more complex trusses. MSC/NASTRAN finite-element-based structural optimization commercial software package was selected to perform structural optimizations to provide the bending material weight for different truss-braced wing configurations. The results from the structural optimizations will then be used in the truss-braced wing MDO code via the response surface methodology. Performing structural optimizations and customizing response surfaces should be studied in the future.

A relatively simple finite element model with a fixed arrangement of spars, ribs, and skin panels is employed. To prevent degree of freedom singularities, the wing skin panels are modeled by CQUAD4 shell elements. Moreover, spar and rib caps are modeled by CROD truss elements. Because spar and rib shear webs contribute to the stiffness of the structure hence they should not be considered as pure shear elements. Therefore, CQUAD4 membrane elements are used to model spar and rib shear webs. Figure 6.4 shows a typical wing box cell that is used herein.

The wing box from top and side views is depicted in Figure 6.5 and Figure 6.6. The front spar is located at 15% chord and the rear spar is located at 60% chord. Also, a 20-30 *in* spacing is considered for the ribs. Moreover, the wing ribs are assumed perpendicular to the rear spar. This arrangement has structural advantages over the case that the ribs are parallel to the flight path. The latter has too many structural disadvantages (Niu, 1988) such as (1) the rib webs are subjected to chordwise bending (2) additional twist is produced due to wing bending.

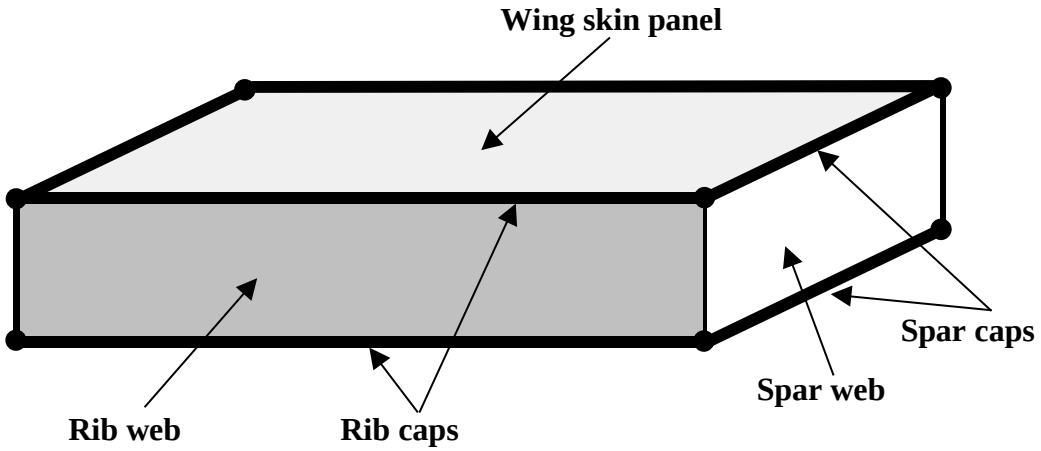

Figure 6.4 Typical wing box cell used in strut-braced wing finite element modeling.

Because of symmetry, only a finite element model of half-wing is generated. For this study, the aluminum alloy with the same properties as before is used.

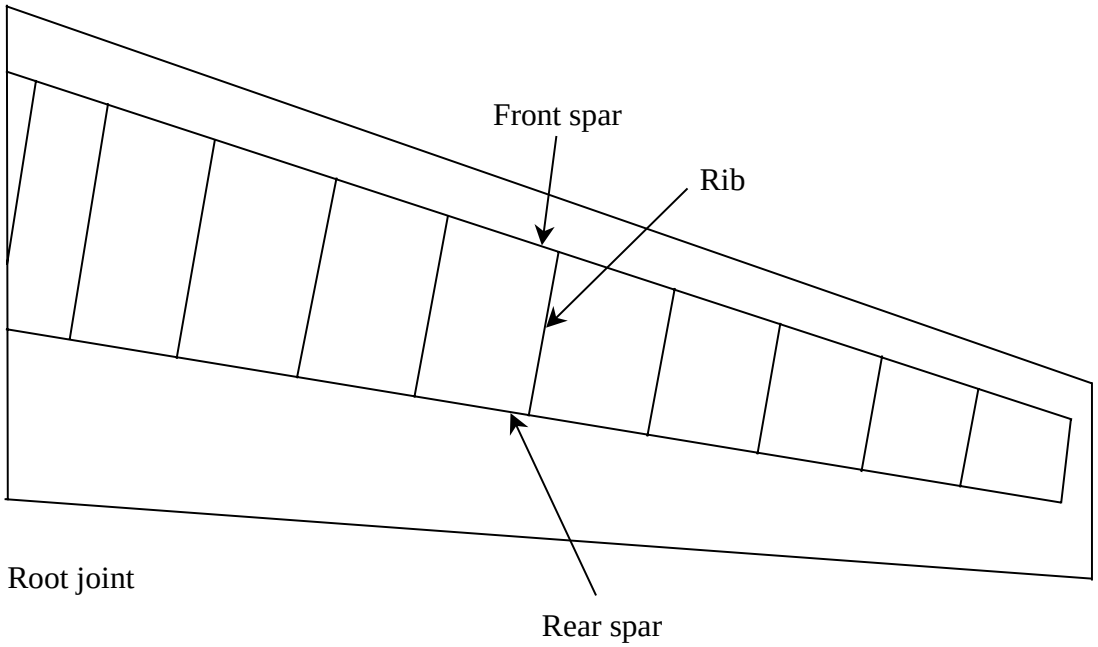

Figure 6.5 Wing spar and rib arrangement.

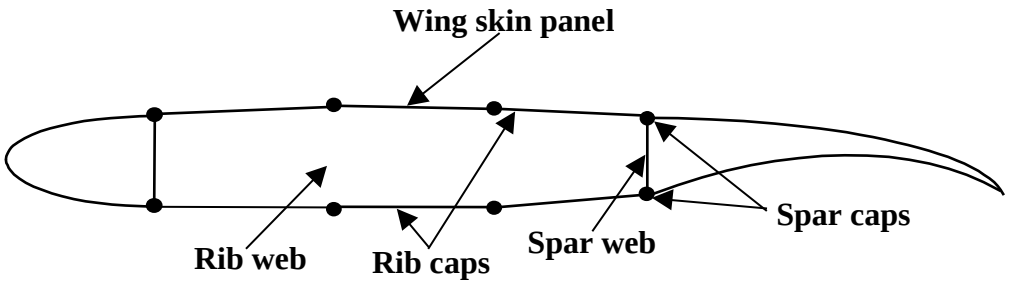

Figure 6.6 Finite element wing box.

6.4 *Strut-Braced Wing Geometry Definitions*

Table 6.1 shows the wing characteristics for the current finite element model. This design configuration belongs to the previous optimized tip-mounted engine design.

Table 6.1 Characteristics of the wing used for FE modeling

	Strut-braced wing Tip-mounted engines
Wing half span (*ft*)	99.7
Wing-strut intersection (*ft*)	87.32
Wing break location (*ft*)	87.32
Wing 1/4 chord sweep (*deg*)	23.89
Strut 1/4 chord sweep (*deg*)	17.71
Wing root chord (*ft*)	27.11
Wing break chord (*ft*)	13.71
Wing tip chord (*ft*)	8.73
Strut root chord (*ft*)	4.51
Strut tip chord (*ft*)	5.75
Wing root *t/c*	0.0919
Wing break *t/c*	0.0502
Wing tip *t/c*	0.0502
Strut *t/c*	0.0500
Strut force (*lbs*)	175,108
Engine pod weight (*lbs*)	20,125
Spanwise engine location (*ft*)	99.7
Zero fuel weight (*lbs*)	324,459
Fuel weight (*lbs*)	165,367
Wing weight (*lbs*)	57,766
Takeoff gross weight (*lbs*)	489,826

6.5 *Strut-Braced Wing Finite Element Model*

A special FORTRAN mesh generator has been developed to automate the mesh generation procedure. The wing geometry parameters are input to the code and the mesh and necessary NASTRAN input cards to perform static aeroelastic analysis are generated. For the future, one needs to modify the code to add the structural optimization input cards to carry out structural optimization.

Currently, the panel thickness distributions from the double plate model are used to create the finite element wing box according to the Lockheed Martin data (confidential). The initial structural sizing is done by distributing the bending material thickness distribution obtained from the piecewise linear load analysis by a FORTRAN program developed by Erwin Sulaeman. To obtain the spanwise distribution of the moments of inertia, the overall cross sectional area of spar caps and skin panels are matched with the respective cross sections of the double plate model. In the future, the structural optimization will be performed to obtain panel thicknesses and spar and rib cap areas by applying Von Mises stress and local buckling constraints.

The current strut-braced wing finite element model contains 432 grid points, 580 CQUAD4 elements, 2 CTRIA3 elements, and 528 CROD elements for the wing and 2 CROD elements for the strut. Also, 2 rigid elements are used to model the engine mount. Moreover, the wing is assumed to be clamped at the fuselage. Thus, a total number of 1114 elements with 2532 degrees of freedom is used in the model. All these numbers may change as the configuration changes. Figure 6.7 shows the finite element model created by the automatic mesh generator. MSC/PATRAN is used for post-processing.

The strut is modeled by assuming two struts connected to the front and rear spars. By this way, the strut force can be transmitted to the spars (Figure 6.7). The existence of the struts decreases the large deformations which would be produced if the struts did

not exist. Therefore the struts can be effective to reduce the static aeroelastic effect on the lift distributions.

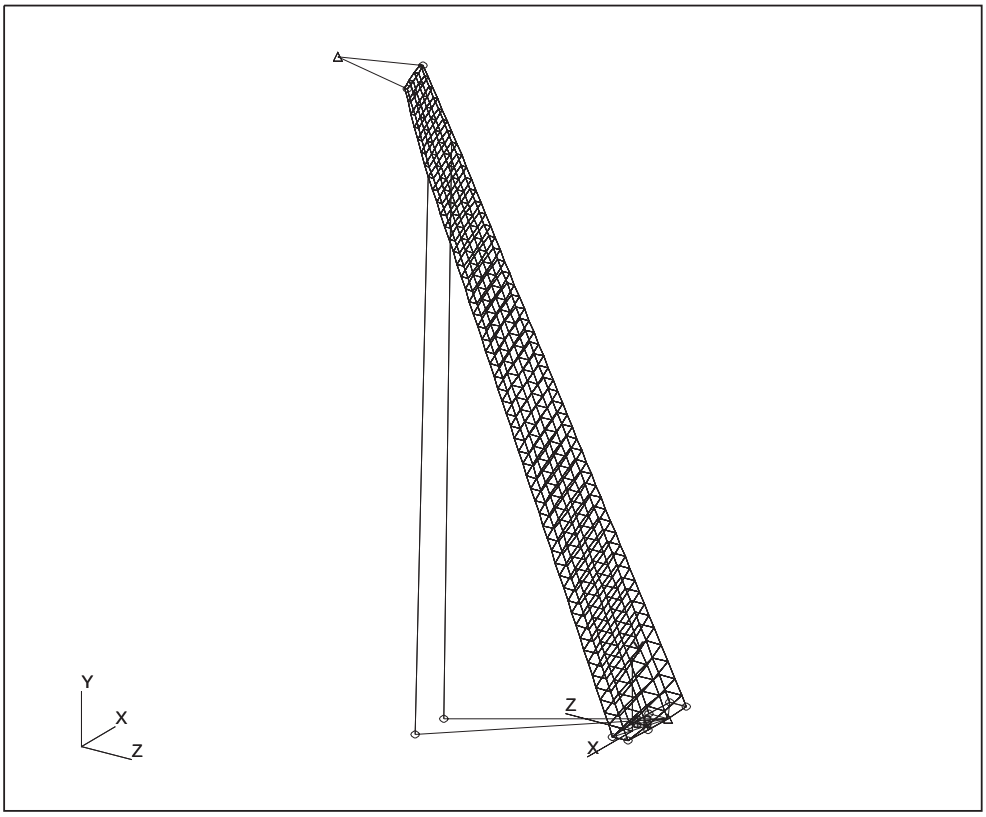

Figure 6.7 MSC/NASTRAN strut-braced wing finite element model.

6.6 *Finite Element Model Validation*

In order to validate the finite element model, the tip deflection of the wing box is obtained for a 10,000 *lb* concentrated load at the wingtip by NASTRAN static analysis and then compared with the same analysis performed by the piecewise linear load method. For the finite element analysis, the concentrated load was equally distributed at the 4 wingtip nodes. The results show good agreement in the *z*-direction at the wingtip midchord as shown in Figure 6.8. The tip deflection obtained from the piecewise linear load model has a deflection of 4.25 *ft*. The wingtip displacement of the finite element model is obtained 3.93 *ft* at the wingtip midchord, which shows a 7% deviation.

Due to the non-symmetry of the wing cross-section, a wing twist is imposed by the concentrated load in addition to the vertical displacement. This twist cannot be captured by the double plate model. Hence, no assessment of the twist result is possible.

(a)

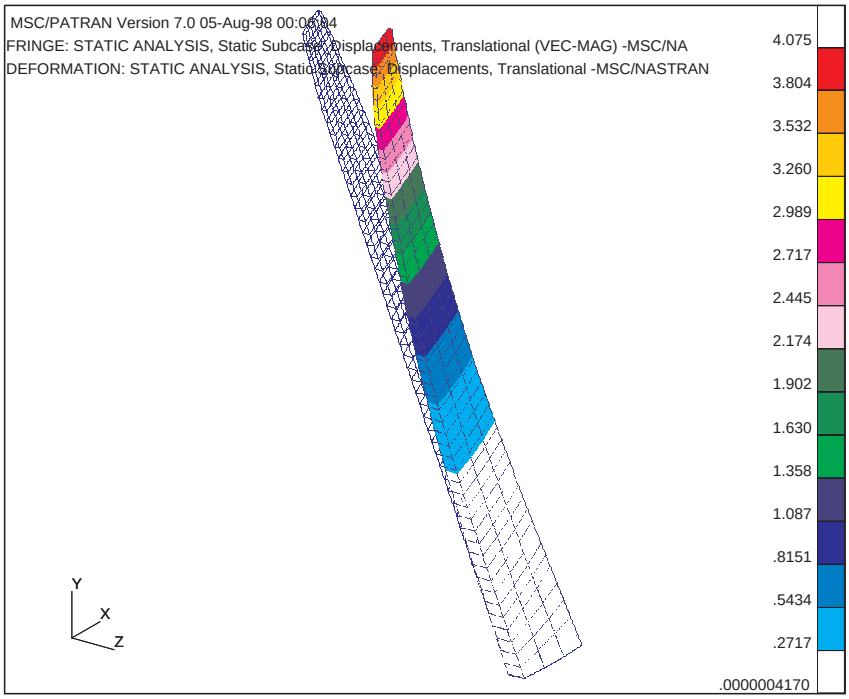

(b)

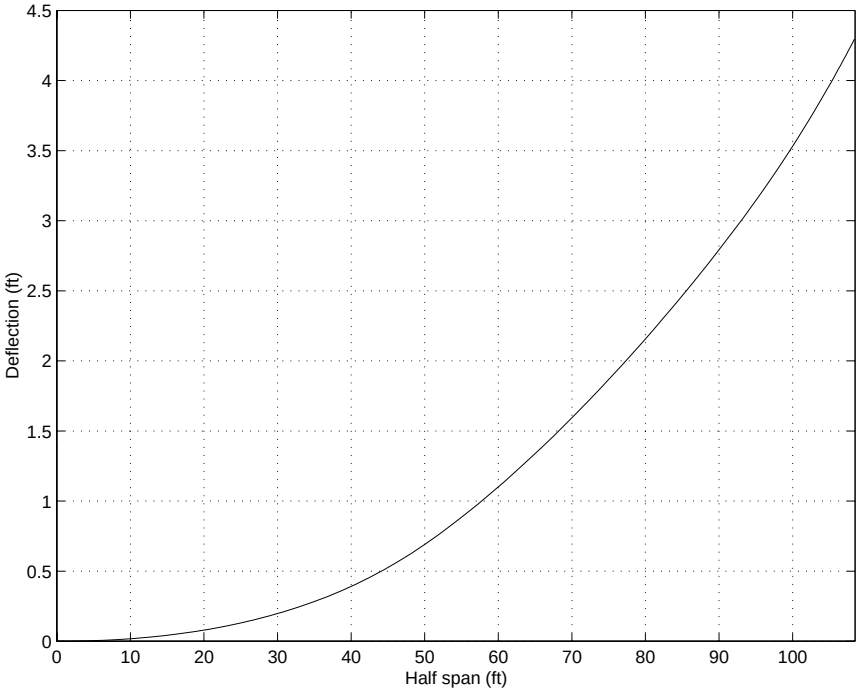

Figure 6.8 Finite element model validation (a) NASTRAN finite element result (b) Piecewise load method result.

6.7 *Static Aeroelasticity Results*

Static aeroelastic analysis is performed for the 1g load condition. The subsonic Doublet Lattice method is used to generate the aerodynamic lift loads on the wing since the available version of MSC/NASTRAN is not capable of performing transonic flow analyses. The rigid lift distribution is obtained by creating a wing structure of very high rigidity. This is determined by having a high material elastic modulus. The rigid and flexible aerodynamic load distributions are shown in Figure 6.9. The rigid aerodynamic load distribution was expected to be close to an elliptical load distribution but it is not. This can be cured by considering the wing jig-shape correction or the wing twist in the finite element model (future work). The rigid wing analysis will provide sufficient information to calculate the jig-shape twist.

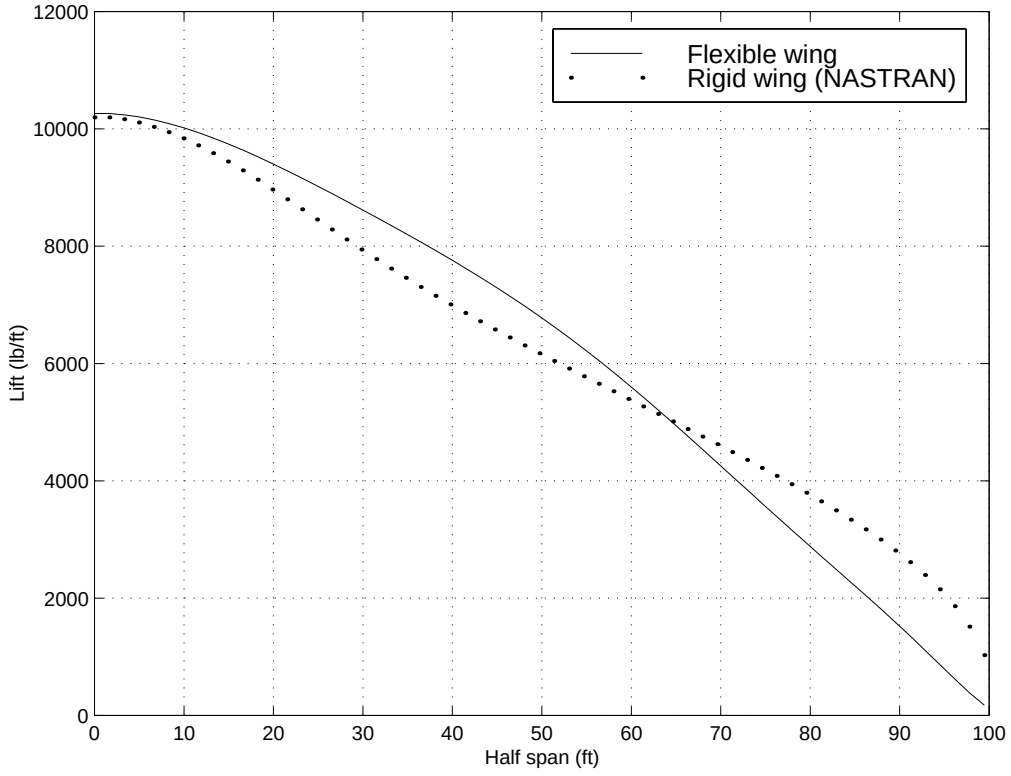

Figure 6.9 Rigid and flexible aerodynamic load distributions.

Figure 6.10 shows the strut-braced wing displacements due to the flexible aerodynamic load distribution at the 1.0g load condition. The wing is subjected to a

considerable wing twist distribution due to non-symmetrical cross-sectional area and chordwise lift pressure distribution. By adjusting the stiffnesses of the struts (aeroelastic tailoring), it will be possible to produce a desirable twist distribution for a drag reduction.

This chapter presented a brief introduction to the static aeroelastic analysis of a strut-braced wing using the finite element method. In the future, an optimization capability will be added for structural optimization. This will be done by using the built-in MSC/NASTRAN Design Sensitivity and Optimization module (Moore, 1995).

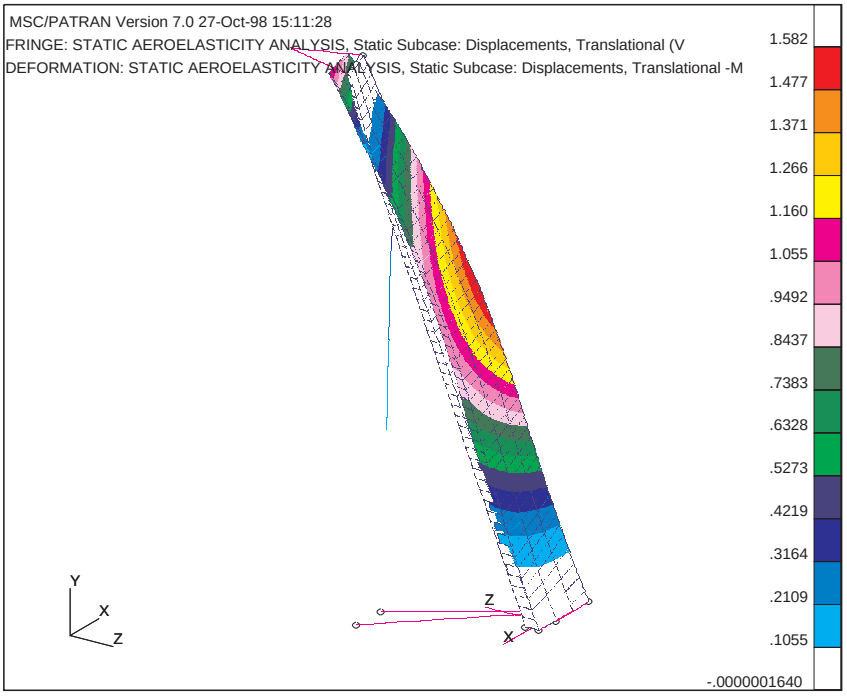

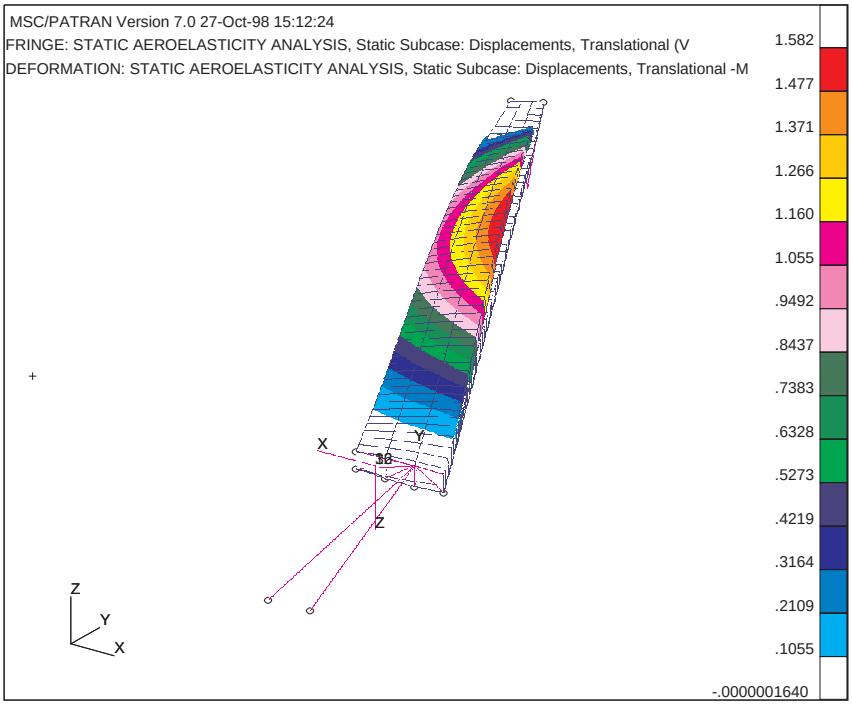

Figure 6.10 Strut-braced wing displacements due to flexible aerodynamic load distribution.

Chapter 7 Concluding Remarks and Future Work

The advantages of a strut-braced wing over its cantilever wing counterpart were explored. Multidisciplinary design optimization (MDO) was employed to integrate different disciplines to construct a tool for conceptual aircraft design. A considerable reduction in takeoff gross weight was obtained by applying the truss-braced wing concepts in combination with advanced technologies and novel design innovations. In this work, a preliminary structural analysis and optimization of a strut-braced wing was investigated.

Two maneuver load conditions (2.5g and -1.0g $\times$ a factor of safety of 1.5), and a 2.0g taxi bump load condition were used to determine the wing bending material weight. An innovative design was considered to eliminate the significant weight penalty due to strut buckling under the -1.0g pushover. Weight savings was accomplished by considering a clamped wing for both positive and negative maneuvers while the strut provides support at positive maneuvers and is inactive at negative maneuvers. This was done by utilizing a telescoping sleeve mechanism. Moreover, the strut force was optimized to provide the minimum wing bending material weight at the 2.5g maneuver. Also, a strut offset member was designed and optimized to reduce significant wing-strut interference drag. The results showed a significant weight reduction.

Two sets of results corresponding to two different design configurations were provided. The first design configuration assumes tip-mounted engines while the second design configuration employs under-wing engines. Shear force, bending moment, vertical deflection, and material thickness distributions were obtained for both design configurations. Also, a composite material based on the future technology was used by applying a technology factor to a state-of-the-art aluminum alloy. The total wing weight results showed 18% and 8% savings associated with tip-mounted engine and under-wing engine configurations, respectively compared to a thoroughly

metallic wing. Furthermore, the use of active load alleviation control was explored to cut down the wing bending material weight. It showed good potential for future investigation.

Overall, this preliminary study of a strut-braced wing showed a considerable weight savings in takeoff gross weight compared to the cantilever wing counterpart without sacrificing performance. The best strut-braced wing configuration exhibited a 18% reduction in wing weight and an 9.4% reduction in takeoff gross weight.

It is recommended that the future work of this study showed focus on:

1. Implementation of two additional constraints, i.e. the inboard wing buckling constraint and the engine location constraint, in the MDO code.
2. Implementation of a hexagonal wing box model in place of the double-plate model. The model was suggested and provided by Lockheed Martin Aeronautical Systems (LMAS). The new model provides higher geometrical accuracy.
3. Structural analysis and optimization of an arch-braced wing using geometrically non-linear finite elements (Kapania and Li, 1998).
4. Structural analysis and optimization of more complex truss-braced wing configurations using the finite element method. Also, other truss configurations rather than the single-strut using the finite element method should be examined.
5. Complete static and dynamic aeroelastic optimization and analysis. One of the main goals of strut braced wing designs is to decrease airfoil thickness and, as a result, to reduce wave drag and increase laminar flow. This thickness reduction results in a reduction of the wing-box torsional stiffness, rendering the aircraft prone to aeroelastic instabilities. Therefore, aeroelastic and structural dynamic analyses must be performed along with the MDO optimization.

References

1. Aerosoft, GASP The General Aerodynamic Simulation Program User's Manual, Version 3, Aerosoft, Inc., Blacksburg, Virginia, 1996.

2. Balabanov, V., "Development of Approximations for HSCT Wing Bending Material Weight Using Response Surface Methodology, Ph.D. Dissertation, Virginia Polytechnic Institute and State University, Blacksburg, VA 24061, September 1997.

3. Balabanov, V., Kaufman, M., Knill, D.L., Giunta, A.A., Haftka, R.T., Grossman, B., Mason, W.H., and Watson, L.T., "Dependence of Optimum Structural Weight on Aerodynamic Shape for a High Speed Civil Transport," AIAA 96-4046, Proceedings of the 6th AIAA/NASA/ISSMO Symposium on Multidisciplinary Analysis and Optimization, pp. 599-612, Sept. 1996.

4. Bennett, J., Fenyes P., Haering W., and Neal M., "Issues in Industrial Multidisciplinary Optimization," AIAA-98-4727, 1998.

5. Bisplinghoff, R.L., Ashley, H., and Halfman, R.L., *Aeroelasticity*, Dover Publications, Inc., 31 East 2nd Street, Mineola, N.Y. 11501, 1983.

6. Coster, J.E., and Haftka, R.T., "Preliminary Topology Optimization of a Truss-Braced Wing," University of Florida, December 1996.

7. Dudley, J., Huang, X., MacMillin, P.E., Grossman, B., Haftka, R.T., and Mason, W.H., "Multidisciplinary Optimization of the High-Speed Civil Transport," AIAA-95-0124, January 1995.

8. Fielding, J. and Wild, F., "Aluminum Alloys in Aircraft--Present Status and Future Potential," *Aluminum Industry*, Vol. 6, No. 4, pp 5-11, May 1987.

9. Gallman, J.W. and Kroo, I.M., "Structural Optimization for Joined-Wing Syntheses," AIAA-92-4761-CP, 1992.

10. Gallman, J.W., Smith, S.C., and Kroo, I.M., "Optimization of Joined-Wing Aircraft," *Journal of Aircraft*, Vol. 30, No. 6, Nov.-Dec., 1993.

11. Giunta, A.A., Balabanov, V., Haim, D., Grossman, B., Mason, W.H., Watson, L.T., and Haftka, R.T., "Wing Design for a High-Speed Civil Transport Using a Design of Experiments Methodology," AIAA, Virginia Polytechnic Institute and State University, Blacksburg, VA 24061, 1996.

12. Giunta, A.A., Balabanov, V., Haim, D., Grossman, B., Mason, W.H., Watson, L.T., and Haftka, R.T., "Multidisciplinary Optimization of a Supersonic Transport Using Design of Experiments Theory and Response Surface Modeling," *The Aeronautical Journal*, pp. 347-356, October 1997.

13. Grasmeyer, J.M., "A Discrete Vortex Method for Calculating the Minimum Induced Drag and Optimum Load Distribution for Aircraft Configurations with Non-coplanar Surfaces," VPI-AOE-242, Multidisciplinary Analysis and Design Center for Advanced Vehicles, Department of Aerospace and Ocean Engineering, Virginia Polytechnic Institute and State University, Blacksburg, VA 24061, January 1997.

14. Grasmeyer, J.M., "Stability and Control Derivative Estimation and Engine-Out Analysis," VPI-AOE-254, Multidisciplinary Analysis and Design Center for Advanced Vehicles, Department of Aerospace and Ocean Engineering, Virginia Polytechnic Institute and State University, Blacksburg, VA 24061, January 1998.

15. Grasmeyer, J.M., "Truss-Braced Wing Description and User's Manual," VPI-AOE-255, Multidisciplinary Analysis and Design Center for Advanced Vehicles, Department of Aerospace and Ocean Engineering, Virginia Polytechnic Institute and State University, Blacksburg, VA 24061, 1998.

16. Grasmeyer, J.M., Naghshineh-Pour, A.H., Tetrault, P.A., Grossman, B., Haftka, R.T., Kapania, R.K., Mason, and W.H., Schetz, "Multidisciplinary Design Optimization of a Strut-Braced Wing Aircraft with Tip-Mounted Engines," MAD 98-01-01, Multidisciplinary Analysis and Design Center for Advanced Vehicles, Virginia Polytechnic Institute and State University, Blacksburg, Virginia 24061, January 1998.

17. Grossman, B., Strauch, G.J., Eppard, W.M., Gurdal, Z., and Haftka, R.T., "Integrated Aerodynamic/Structural Design of a Sailplane Wing," AIAA-86-2623, Dayton, Ohio, October 20-22, 1986.

18. Haftka, R.T. and Gurdal Z., *Elements of Structural Optimization*, Kluwer Academic Publishers, P.O. Box 17, 3300 AA Dordrecht, The Netherlands, 1992.

19. Hajela, P. and Chen J.L., "Optimum Structural Sizing of Conventional Cantilever and Joined-Wing Configurations Using Equivalent Beam Models," AIAA-86-2653, Dayton, Ohio, October 20-22, 1986.

20. Hoerner, S.F., "Fluid-Dynamic Drag: Practical Information on Aerodynamic Drag and Hydrodynamic Resistance," Midland Park, NJ, pp. 8-1-8-20, 1965.

21. Hönlinger, H.G., Krammer, J., and Stettner, M., "MDO Technology Needs in Aeroelastic Structural Design," AIAA-98-4731, 1998.

22. Huang, X., *Structural Optimization and Its Integration with Aerodynamic Optimization for a High Speed Civil Transport*, Ph.D. Dissertation, Virginia Polytechnic Institute and State University, Blacksburg, VA 24061, September 1994.

23. Hutchison, M.G., Unger, E.R., Mason, W.H., Grossman, B., Haftka, R.T., "Variable Complexity Aerodynamic Optimization of a High Speed Civil Transport Wing," *Journal of aircraft*, Vol. 31, No. 1, pp. 110-116, 1994.

24. Joslin, R.D., "Aircraft Laminar Flow Control," *Annual Review of Fluid Mechanics*, Annual Reviews Inc., Vol. 30, pp. 1-29, Palo Alto, CA, 1998.

25. Kapania, R.K. and Li, J., "A Four-Noded 3-D Geometrically Nonlinear Curved Beam Element with Large Displacements/Rotations, in Modeling and Simulation Engineering," Atluri, S.N., O'Dononghue (ed.), Technology Science Press, 679-784, 1998.

26. Kaufman, M., Balabanov, V., Burgee, S.L., Giunta, A.A., Grossman, B., Haftka, R.T., Mason, W.H., and Watson, L.T., "Variable-Complexity Response Surface Approximations for Wing Structural Weight in HSCT Design," *Computational Mechanics*, Vol. 18, No. 2, pp. 112-126, June 1996.

27. Knill, D.L., Giunta, A.A., Baker, C.A., Grossman, B., Mason, W.H., Watson, L.T., and Haftka, R.T., "HSCT Configuration Design Using Response Surface Approximations of Supersonic Euler Aerodynamics," AIAA-98-0905, 1998.

28. Korte, J.J., Weston, R.P., and Zang, T.A., "Multidisciplinary Optimization Methods for Preliminary Design," Multidisciplinary Optimization Branch, MS 159, NASA Langley Research Center, 1998.

29. Kroo, I., "MDO Applications in Preliminary Design: Status and Directions," 38th AIAA/ASME/ASCE/ASC Structures, Structural Dynamics, and Materials Conference, Kissimme, Florida, April 7-10, 1997.

30. Kroo, I., Altus, S., Braun, R., Gage, P., and Sobieski, I., "Multidisciplinary Optimization Methods for Aircraft Preliminary Design," AIAA-94-4325, 1994.

31. Kroo, I.M. and Gallman J.W., "Aerodynamic Structural Studies of Joined-Wing Aircraft," *Journal of aircraft*, Vol. 28, No. 1, pp. 74-81, May 7, 1990.

32. Kulfan, R.M., and Vachal, J.D., "Wing Planform Geometry Effects on Large Subsonic Military Transport Airplanes," Boeing Commercial Airplane Company, AFFDL-TR-78-16, February 1978.

33. Lee, J.M., MSC/NASTRAN Linear Static Analysis User's Guide Version 69, MacNeal-Schwendler Corporation, 1997.

34. Lomax, T.L., Structural Loads Analysis for Commercial Transport Aircraft: Theory and Practice, AIAA, Reston, Virginia, 1996.

35. McCullers, L.A., *FLOPS User's Guide, Release 5.81,* NASA Langley Research Center.

36. Moore, G.J., MSC/NASTRAN Design Sensitivity and Optimization User's Guide Version 68, MacNeal-Schwendler Corporation, 1995.

37. Niu, M.C.Y., *Airframe Structural Design*, Lockheed Aeronautical Systems Company, Burbank, California, 1988.

38. Parikh, P. and Pirzadeh, S., "A Fast Upwind Solver for the Euler Equations on Three-Dimensional Unstructured Meshes," AIAA-91-0102, Reno, Nevada, January 7-10, 1991.

39. Park, H. P., "The Effect on Block Fuel Consumption of a Strutted vs. Cantilever Wing for a Short Haul Transport Including Strut Aeroelastic Considerations," AIAA-78-1454-CP, Los Angeles, California, Aug. 21-23, 1978.

40. Patel, H.D., "Multidisciplinary Design Optimization with Superelements in MSC/NASTRAN," AIAA-92-4732-CP, 1992.

41. Rais-Rohani, M., *Integrated Aerodynamics-Structural-Control Wing Design*, Ph.D. Dissertation, Virginia Polytechnic Institute and State University, Blacksburg, VA 24061, September 1991.

42. Raymer, D.P., *Aircraft Design: A Conceptual Approach*, AIAA, Washington D.C., 1992.

43. Rodden, W.P. and Johnson, E.H., *MSC/NASTRAN Aeroelastic Analysis User's Guide Version 68*, MacNeal-Schwendler Corporation, 1995.

44. Selberg, B.P. and Cronin, D.L., "Aerodynamic-Structural Optimization of Positive/Negative Stagger Joined-Wing Configurations," AIAA-86-2626, Dayton, Ohio, October 20-22, 1986.

45. Thomas, H.L., Shyy, Y-K., Vanderplaats, G.N., and Miura, H., "GENESIS - A Modern Shape and Sizing Structural Design Tool," AIAA-92-2559-CP, 1991.

46. Torenbeek, E., "Development and Application of a Comprehensive, Design Sensitive Weight Prediction Method for Wing Structures of Transport Category Aircraft," Delft University of Technology, Report LR-693, Sept. 1992.

47. Turriziani, R.V., Lovell, W.A., Martin, G.L., Price, J.E., Swanson, E.E., and Washburn, G.F., "Preliminary Design Characteristics of a Subsonic Business Jet Concept Employing an Aspect Ratio 25 Strut Braced Wing," NASA CR-159361, October 1980.

48. Vanderplaats Research & Development, Inc., *DOT User's Manual, Version 4.20*, Colorado Springs, CO, 1995.

49. Vanderplaats, G.N., "Automated Optimization Techniques for Aircraft Synthesis," AIAA-76-909-CP, Dallas, Texas, September 27-29, 1976.

50. Venkayya, V.B., Tischler, V.A., and Bharatram, G., "Multidisciplinary Issues in Aircraft Design," AIAA-96-1386-CP, 1996.

51. Vitali, R., Park, O., Haftka, R.T., Sankar, B.V., and Rose. C., "Structural Optimization of a Hat Stiffened Panel," Department of Aerospace Engineering, Mechanics and Engineering Science, Gainesville, FL 32611-6250, 1998.

52. Wolkovitch, J., "The Joined Wing: An Overview," AIAA-85-0274-CP, Reno, NV, January 14-17, 1985.

53. Young, J.A., Anderson, R.D., and Yurkovich, R.N., "A Description of the F/A-18E/F Design and Design Process," AIAA-98-4701-CP, St. Louis, Missouri, September 2-4, 1998.

Appendix A FLOPS Wing We i ght Equations

The general wing weight equation in FLOPS is based on an analytical expression to relate the wing bending material weight to the wing geometry, material properties, and loading. Other weight terms are added to account for shear material, control surfaces, and nonstructural weight. Additionally, technology factors are included to correlate with a wide range of existing transports and to reflect features such as composite materials, aeroelastic effects, and external strut bracing. The wing weight W_{wing} used within FLOPS is given as

$$W_{wing} = \frac{W_{gross} K_e W_{wing1} + W_{wing2} + W_{wing3}}{1 + W_{wing1}}, \tag{A.1}$$

where

$$W_{wing1} = K f_{ult} b (1 - 0.4 f_{comp})(1 - 0.1 f_{aert}),$$

$$W_{wing2} = 0.68(1 - 0.17 f_{comp}) S_{flap}^{0.34} W_{gross}^{0.6},$$

$$W_{wing3} = 0.035(1 - 0.3 f_{comp}) S_w^{1.5},$$

$$K = (8.8 \times 10^{-6})\left(1 + \sqrt{6.25 / b}\right) B_t,$$

$$K_e = 1 - \left(\frac{B_{te}}{B_t}\right)\left(\frac{W_{pot}}{W_{gross}}\right),$$

and W_{gross} denotes the gross takeoff weight (*lbs*), W_{wing1} denotes the wing bending material weight (*lbs*), W_{wing2} denotes the wing shear material and flaps weight (*lbs*), W_{wing3} denotes the wing control surfaces and non-structural weight (*lbs*), W_{pod} denotes the engine pod weight (*lbs*), b denotes the wing span (*ft*), B_t denotes the bending material factor, B_{te} denotes the engine relief factor, f_{ult} denotes the ultimate load factor, f_{comp} denotes the composite material factor, f_{aert} denotes the aeroelastic

tailoring factor, S_w denotes the wing reference area (ft^2), and S_{flap} denotes the flaps area (ft^2).

The system is closed except for the bending material factor B_t and the engine relief factor B_{te}. The parameter B_t accounts for the load distribution on the wing and is calculated by approximating determining the required material volume of the upper and lower wing skin panels in a simple wing box description of the wing. The parameter B_{te} accounts for the reduced amount of structural weight necessary due to the presence of the engines on the wing. The weighted average of the load sweep angle at 75% chordwise

$$\Lambda_L = \int_0^1 (1+2y)\Lambda(y)dy.$$

Now it is necessary to determine the bending moment assuming a simple elliptic pressure distribution.

$$M(y) = \int_0^y p(\xi)\xi d\xi.$$

The necessary flange areas are calculated

$$A(y) = \frac{M(y)}{t(y)c(y)Cos\Lambda(y)},$$

and the required volume as

$$V = \int_0^1 A(y)dy.$$

The total load is

$$L = \int_0^1 p(y)dy,$$

and the bending material factor is finally given as

$$B_t = \frac{2V}{Ld},$$

where

$$d = AR^{0.25}\left[1 + (0.5 f_{aert} - 0.16)Sin^2\Lambda_L + 0.3K_a(1 - 0.5 f_{aert})Sin\Lambda_L\right],$$

AR is the aspect ratio and K_a is given by

$$\begin{cases} AR - 5, & \text{if } AR > 5, \\ 0, & \text{otherwise} \end{cases}$$

B_{te} accounts for the reduced amount of structural weight necessary due to the presence of the engines on the wing.

$$B_{te} = 16\int_{y_{root}}^{y_{tip}} NE\left(\frac{y_{tip} - y}{Cos^2\Lambda(y)}\right)\left(\frac{y_{tip} - y_{root}}{c(y)Max(t/c)}\right)dy,$$

where *NE* is given by

$$NE = \begin{cases} 2, & y < y_{nacelle1}, \\ 1, & y_{nacelle1} < y < y_{nacelle2}, \\ 0, & y > y_{nacelle2}. \end{cases}$$

Appendix B *Wing.f* Code Description

A FORTRAN code labeled *wing.f* has been provided to estimate the single-strut-braced wing bending material weight. This appendix describes the code. For the full description of the strut-braced wing MDO code, the reader may refer to Grasmeyer (1998). All the necessary information, i.e. aerodynamic lift loads, fuel distribution, and wing geometry parameters, is passed from the MDO code as shown in Figure 4.1. The code is capable of estimating the bending material weight for both cantilever and strut-braced wings at three different load conditions. Also, the code can be run separately without running the MDO code at the same time by defining a parameter set along with fuel and load information as separate input files. **.in* provides the input parameters, **.fuel* provides the spanwise fuel distribution, and **.loads* provides the spanwise load distributions. The above input files are read by the *wingin.f* code and passed to *wing.f*.

B.1 *Wing.f Structure*

The code consists of a main body and several subroutines. Figure B.1 shows the *wing.f* flowchart. First, the wing parameters and the lift and fuel distributions are read and then interpolated onto the structural nodes. The shear force and bending moment distributions are calculated to estimate the bending material weight. The bending material weight is substituted for the value in FLOPS to calculate the wing weight due to the maneuver load conditions using FLOPS wing weight equations. The wing weight along with the fuel weight distribution are combined to create the taxi loads. The taxi analysis is performed to calculate the bending material weight due to the taxi bump load condition. Finally, the bending material weight due to the maneuvers and bending material weight due to the taxi bump condition are compared to calculate the total bending material weight and to obtain the design material distribution.

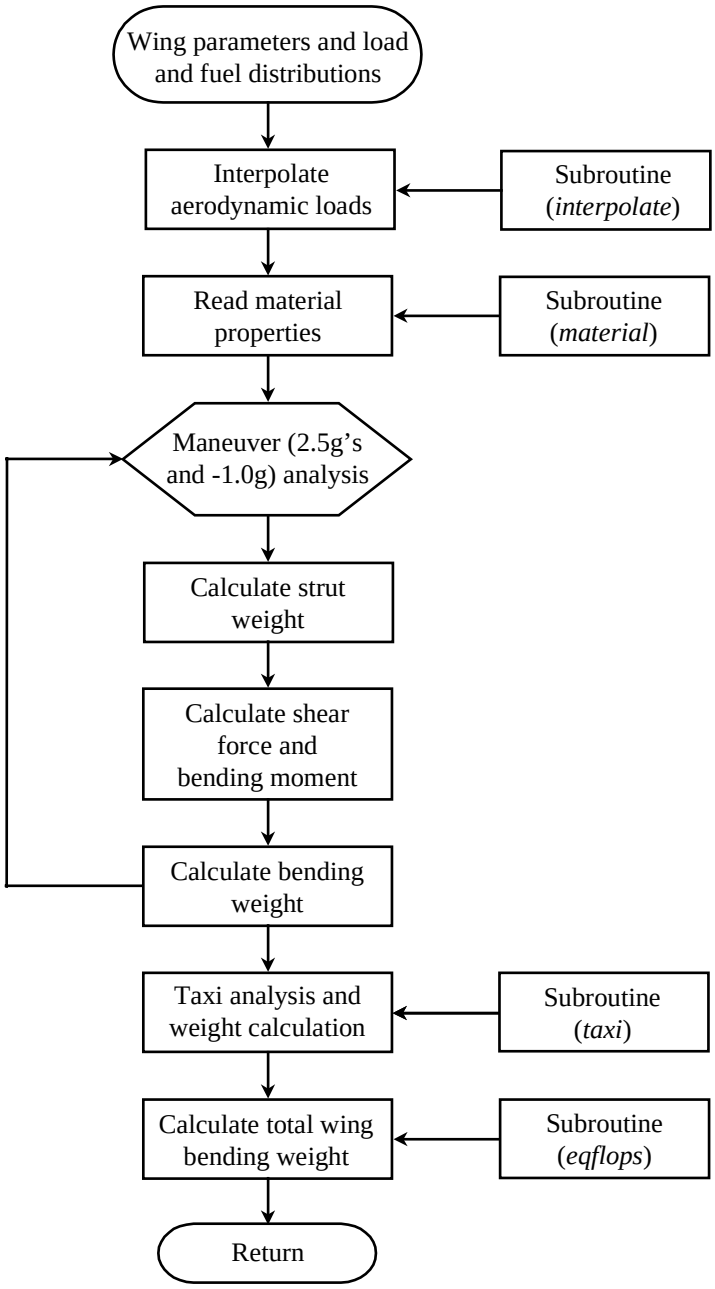

Figure B.1 *Wing.f* structure flowchart.

B.2 *Parameter set*

Table B.1 shows the common parameters between the MDO code and *wing.f* for bending material weight estimation. These parameters can also be set up as an input file (*.*in*) to run the *wing.f* code separately.

Table B.1 *Wing.f* parameter set

Variable Name	Description
outfile	Output file description
title	Title
write_flag	See MDO code user's manual
config_class	Configuration class (0 = cantilever, 1 = single-strut)
fuse_flag	Fuselage flag (0 = wing engines, 1 = fuselage engines)
h	Vertical separation between wing and strut at centerline (*ft*)
bl_int	Spanwise position of wing-strut intersection (*ft*)
bl_break	Spanwise position of chord breakpoint (*ft*)
hspan_wing	Wing semispan (*ft*)
sweep_wing_in	Inboard average wing quarter-chord sweep (*deg*)
sweep_wing_out	Outboard average wing quarter-chord sweep (*deg*)
sweep_strut	Strut sweep (*deg*)
offset	Chordwise wing-strut offset at wing-strut intersection (*ft*)
c_wing_root	Wing centerline chord (*ft*)
c_wing_mid	Wing chord at chord break (*ft*)
c_wing_tip	Wing tip chord (*ft*)
c_strut_root	Strut centerline chord (*ft*)
c_strut_tip	Strut tip chord (*ft*)
tc_wing_in	Wing centerline *t/c*
tc_wing_break	Wing break *t/c*
tc_wing_out	Wing tip *t/c*
tc_strut	Strut *t/c*
npanels	See MDO code user's manual
nvortices	See MDO code user's manual
xv, yv, zv	See MDO code user's manual
loads	Aerodynamic lift loads (*lbs/ft*)
t_root	Wing-box panel thickness at the root (*ft*)
f_spring_1	Vertical strut force (*lbs*)
dia_nacelle	Nacelle diameter (*ft*)
height_pylon	Pylon height (*ft*)
dia_fuse	Fuselage diameter (*ft*)
fcomp	Composite technology factor
faert	Aeroelastic technology factor
sflap	Control surfaces area (ft^2)
sw	Wing surface area (ft^2)
eta_engine_1	Percent spanwise location of engine 1
eta_engine_2	Percent spanwise location of engine 2
w_pod	Engine pod weight (*lbs*)
w_zf	Zero fuel weight (*lbs*)
w_to	Maximum takeoff weight (*lbs*)
cl_to	Takeoff lift coefficient

Table B.1 *Wing.f* parameter set (continued)

Variable Name	Description
pct_c_tank	Percent chord (*x/c*) of fuel tank
nstrips_tank	Number of integration strips per fuel tank
bl_fuel_dist	Spanwise position of fuel distribution (*ft*)
fuel_dist	Fuel distribution (*lbs/ft*)
fuel_strut	Strut fuel weight (*lbs*)
w_bm	Bending material weight (*lbs*)
max_def_taxi	Maximum wing deflection in taxi bump (*ft*)
loadf_slack	Slack load factor
w_strut_offset	Strut offset weight (*lbs*)
w_strut_only	Strut weight without offset weight (*lbs*)
strut_offset	Strut offset length (*ft*)

B.3 *Other Important Parameters*

Some of important parameters which are used in *wing.f* are summarized in Table B.2. Other parameters are commented in the code.

Table B.2 Important *wing.f* internal parameters

Variable Name	Description
comp_flag	Composite flag (0 = metallic, 1 = composite)
load_flag	Load flag (0 = regular, 1 = load alleviation)
ratio_box	Wing box chord to wing chord
safe_factor	Factor of safety
load_factor_375	2.5 Load factor × factor of safety
load_factor_15	1.5 Load factor × factor of safety
lfactor_taxi	Taxi load factor
stress_all_wing	Wing material allowable stress
stress_all_strut	Strut material allowable stress
den_wing	Wing material density
den_strut	Strut material density
modul_wing	Wing material Young's module
modul_strut	Strut material Young's module
pthick_gauge	Minimum panel thickness gauge
w_wing_1	Wing bending material weight
w_wing_2	Wing shear and flaps weight
w_wing_3	Wing non-structural weight
w_wing_to	Wing total weight

B.4 **.in Input Files*

To be able to run *wing.f* separately from the MDO code, a parameter set should be defined. **.in* input files are used to define different parameter sets for different configurations. A sample of such a file is shown as follows:

input file for wing
ss6

1	***write_flag***
1	***config_class***
1	***fuse_flag***
20.3	***h***
106.32	***eta_int***
106.32	***eta_break***
128.97	***hspan_wing***
20.12	***sweep_wing_in_3_4***
23.20	***sweep_wing_out_3_4***
16.30	***sweep_strut_3_4***
1.	***offset***
29.38	***c_wing_root***
10.35	***c _wing_mid***
9.11	***c_wing_tip***
4.00	***c_strut_root***
5.57	***c_strut_tip***
0.0851	***tc_wing_in***
0.0676	***tc_wing_break***
0.0500	***tc_wing_out***
0.0500	***tc_strut***
0.0200	***t_skin_root***
207256.	***strut_force***
13.1	***dia_nacelle***
4.1	***height_pylon***
20.3	***dia_fuse***
0.0	***fcomp***
0.0	***faert***
977.8	***sflap***
3259.3	***sw***
0.766	***eta_engine_1***
0.	***eta_engine_2***
19212.	***w_pod***
332185.	***w_zf***
481027.	***w_to***
0.812	***cl_ci***
4	***npanels***
50	***nvortices***
0	***spacing_flag***
25	***nvortices***
1	***spacing_flag***
25	***nvortices***
0	***spacing_flag***
10	***nvortices***
1	***spacing_flag***

B.5 **.fuel Input Files*

**.fuel* input files are used for the fuel distributions for different configurations when *wing.f* is run separately from the MDO code. A sample of **.fuel* input files is as follows:

```
fuel input file for wing
0.5                pct_c_tank
2704.              fuel_strut
10
0.507500           985.505
1.52250            979.992
2.53750            974.479
3.55250            968.965
4.56750            963.452
5.58250            957.939
6.59750            952.425
7.61250            946.912
8.62750            941.399
9.64250            935.885
14.9585            1461.57
24.5754            1205.51
34.1923            981.214
43.8092            786.576
53.4262            619.497
63.0431            477.880
72.6600            359.625
82.2770            262.632
91.8939            184.802
101.511            124.036
107.452            57.1994
109.717            55.8308
111.981            54.4787
114.246            53.1433
116.511            51.8244
118.776            50.5221
121.041            49.2364
123.306            47.9672
125.571            46.7146
127.836            45.4786
5.31596            8.99235
15.9479            9.69839
26.5798            10.4311
37.2118            11.1905
47.8437            11.9766
58.4756            12.7894
69.1075            13.6288
79.7395            14.4949
90.3714            15.3877
101.03             16.3072
```

The fist column represents the fuel spanwise location in (*ft*) and second column represents the fuel distribution in (*lbs/ft*). For more details, the reader may refer to the MDO User's Manual (Grasmeyer, 1998).

B.6 **.loads Input Files*

**.loads* input files are used for the load distributions for different configurations when *wing.f* is run separately from the MDO code. The two maneuver load conditions are read from a **.loads* input file. A sample is not given.

B.7 **.wing and *.dat Output Files*

**.wing* output files represent the calculated quantities by *wing.f*. The necessary data for post-processing are produced in **.dat* output files.

B.8 *Post-Processing*

A MATLAB code labeled *wing.m* has been provided for post-processing. This code reads the output files produced by *wing.f* and generates the required plots. Samples of the post-processing results are shown in Figures 5-1 to 5-6.

Vita

Amir H. Naghshineh-Pour was born on March 3, 1969 in Tehran, Iran. After graduation from high school in Tehran in 1986, he entered Azad University in Tehran and graduated with the Bachelor of Science in Mechanical Engineering. After two years of working as an engineer in a consulting engineering company, he began his post graduate studies in 1994 at North Carolina Agricultural and Technical State University and completed his Master of Science degree in Mechanical Engineering in 1996. Due to his interest in aircraft and aerospace engineering he also decided to pursue his education in the aerospace field. He joined the Aerospace and Ocean Engineering Department at Virginia Polytechnic Institute and State University in August 1996 and graduated with the Master of Science degree in Aerospace Engineering in December 1998. He will join BFGoodrich, Aerospace, Aerostructures Group located in San Diego, California.